University of Cologne

Faculty of Mathematics and Natural Sciences

Department of Biology

Structure-Function Analysis of STICHEL in the Context of Trichome Branching of *Arabidopsis thaliana*

Inaugural-Dissertation
zur
Erlangung des Doktorgrades
der Mathematisch-Naturwissenschaftlichen Fakultät
der Universität zu Köln
vorgelegt von
Helen Yvonne Bärbel Janßen

Köln, 2026

Abstract

Trichome branching in *Arabidopsis thaliana* is a well-established model for studying spatially controlled cell morphogenesis. The *STICHEL* (*STI*) gene is required for proper branch initiation during trichome development, but its molecular function has remained unresolved. Early sequence analyses suggested similarity to ATPase-associated proteins, although experimental evidence supporting ATPase activity has been lacking.

In this study, *STI* was investigated using bioinformatic, biochemical, and cell biological approaches. Structural predictions and sequence analyses identified a conserved central region containing motifs associated with ATPase-related proteins. Comparative analyses supported the presence of an ATPase-like core architecture. However, ATPase assays using recombinant STI fragments did not detect measurable ATP hydrolysis under the tested conditions, suggesting that STI may not function as a classical enzymatically active ATPase.

To analyse STI function *in planta*, fluorescent reporter constructs were generated and expressed in *A. thaliana*. Confocal microscopy revealed enrichment of STI at prospective branch initiation sites in developing trichomes, supporting a role during early branch establishment. Complementation experiments further demonstrated that STI-tdTomato constructs restore branching in the *sti* mutant background, confirming functionality of the examined fusion protein.

Because trichome branch initiation depends on highly coordinated cortical organization involving actin-associated processes, potential interactions between STI and members of the NET1 protein family were investigated. Yeast two-hybrid analyses revealed specific interactions between STI and a C-terminal region of several NET1 paralogs. In contrast, no interaction was detected with the conserved N-terminal actin-binding NAB domain of NET1 proteins.

Together, the results of this work support a model in which STI functions as part of a regulatory protein network involved in localized cortical organization during branch initiation. Rather than acting as a conventional ATPase, STI may fulfil scaffold-like or regulatory functions associated with cytoskeleton-dependent processes required for polarized trichome morphogenesis.

Table of Contents

List of Figures

List of Tables

List of Abbreviations

°C	degree Celsius
µl	microliter
µm	micrometer
µmol	micromole
AAA+	ATPases associated with diverse cellular activities
amp	ampicillin
AOA	aminooxyacetic acid
AVG	2-aminoethoxyvinyl glycine
bp	base pairs
carb	carbenicillin
cm	centimeters
CRISPR	clustered regularly interspaced short palindromic repeats
DAPI	4′,6-diamidino-2-phenylindole
ddH_2O	double distilled water
DMSO	dimethyl sulfoxide
DNA	deoxyribonucleic acid
dNTPs	deoxyribonucleotides
EDTA	ethylenediaminetetraacetic acid
EMS	ethyl methanesulfonate
Et al.	et alii
EtOH	ethanol
FDA	fluorescein diacetate
g	grams
GFP	green fluorescent protein
h	hours
HBSS	Hank’s balanced salt solution
HDR	homology-directed repair

his	histidine
Kan	kanamycin
kb	kilobase
L	liter
LB	lysogeny broth
M	molar concentration
MBP	maltose-binding protein
MES	2-(N-morpholino)ethanesulfonic acid
mg	milligrams
min	minutes
mL	milliliter
mM	millimolar
mm	millimeter
NAB domain	NET actin-binding domain
NCBI	National Center for Biotechnology Information
ng	nanogram
NLS	nuclear localization signal
nm	nanometer
O/N	over night
OD	optical density
ORF	open reading frame
p	promoter
PAM	protospacer adjacent motif
PCR	polymerase chain reaction
PI	propidium iodide
Rif	rifampicin
RNA	ribonucleic acid
rpm	revolutions per minute

RT	room temperature
SDS page	odium dodecyl sulfate polyacrylamide gel electrophoresis
sec	seconds
Spec	spectinomycin
T-DNA	transfer DNA
w/v	weight per volume
Y2H	Yeast two-hybrid
YFP	yellow fluorescent protein

1 Introduction

1.1 Plant cell morphogenesis as a precisely controlled process

Plant morphogenesis arises from coordinated processes that control cell division, cell expansion and differentiation. In contrast to animal cells, plant cells are surrounded by rigid cell walls and remain physically connected to neighbouring cells, which prevents cell migration. Consequently, the shape of plant organs is primarily determined by spatially regulated patterns of cell growth and division. Precise control of cell expansion is therefore a fundamental determinant of plant morphology and tissue architecture.

Cell expansion is largely driven by internal turgor pressure generated through osmotic water uptake. This hydrostatic pressure acts as the mechanical force underlying cell enlargement. However, expansion occurs only when the surrounding cell wall yields to this pressure. Thus, the rate and direction of growth depend on the mechanical properties and extensibility of the primary cell wall, which are dynamically regulated by biochemical and cellular processes (Cosgrove, 2005).

The primary cell wall is a complex structure composed mainly of cellulose microfibrils embedded in a matrix of hemicelluloses and pectins. This organization provides both mechanical strength and flexibility, allowing the wall to withstand turgor pressure while permitting controlled expansion. Cellulose microfibrils form the principal load-bearing network, whereas the surrounding polysaccharide matrix contributes to wall plasticity and hydration. Regulation of wall extensibility, for example through the activity of cell wall-modifying proteins such as expansins, enables localized wall loosening and thereby directs cell growth (Cosgrove, 2005).

A key feature of plant cell morphogenesis is anisotropic growth. Rather than expanding uniformly in all directions, many plant cells grow along defined axes, resulting in diverse cell shapes. This directional growth is largely determined by the orientation of cellulose microfibrils within the cell wall. The spatial arrangement of these microfibrils constrains the direction of expansion, as the wall is mechanically strongest parallel to microfibril orientation and more extensible perpendicular to it (Baskin, 2001; Cosgrove, 2005).

The cytoskeleton plays a central role in controlling the spatial organization of cell expansion. Cortical microtubules located beneath the plasma membrane guide the movement of cellulose synthase complexes and thereby influence the orientation of newly deposited cellulose microfibrils (Baskin, 2005). Through this mechanism, microtubules contribute to the establishment of directional growth patterns and ultimately to cell shape determination.

In addition to microtubules, actin filaments are critical regulators of plant cell morphogenesis. Actin networks are involved in vesicle trafficking, organelle positioning and targeted secretion of cell wall components to specific regions of the plasma membrane. These processes are essential for sustained cell expansion and for the establishment of polarized growth domains (Smith & Oppenheimer, 2005; Szymanski, 2005). Continuous remodelling of actin filaments by actin-binding proteins enables dynamic cytoskeletal reorganization during growth and development.

Plant cell morphogenesis therefore results from the integration of turgor-driven mechanics, cell wall architecture and cytoskeletal organization. Increasing evidence suggests that these systems function as a coordinated network in which mechanical feedback from the cell wall can influence cytoskeletal organization, while cytoskeletal dynamics regulate the deposition and modification of wall components (Baskin, 2005).

Understanding the mechanisms underlying plant cell morphogenesis is essential for explaining how specialized cell types acquire their characteristic shapes. Highly polarized cells such as root hairs, pollen tubes and leaf trichomes represent powerful model systems for studying these processes, as their morphogenesis involves pronounced spatial control of cell expansion (Hülskamp, 2004; Szymanski et al., 2000).

1.2 Trichomes as a model for plant cell morphogenesis

Leaf trichomes of *Arabidopsis thaliana* have become a widely used system for investigating plant cell morphogenesis. Trichomes of *A. thaliana* are specialized epidermal cells that differentiate into large, branched, unicellular structures. They function as a physical and chemical defence against herbivores and contribute to tolerance of abiotic stress (Dalin et al., 2008; Glas et al., 2012; Hauser, 2014). Because each trichome originates from a single cell and follows a defined developmental program, this system provides a powerful framework for

studying how genetic and cellular processes control cell shape (Hülskamp, 2004; Szymanski et al., 2000).

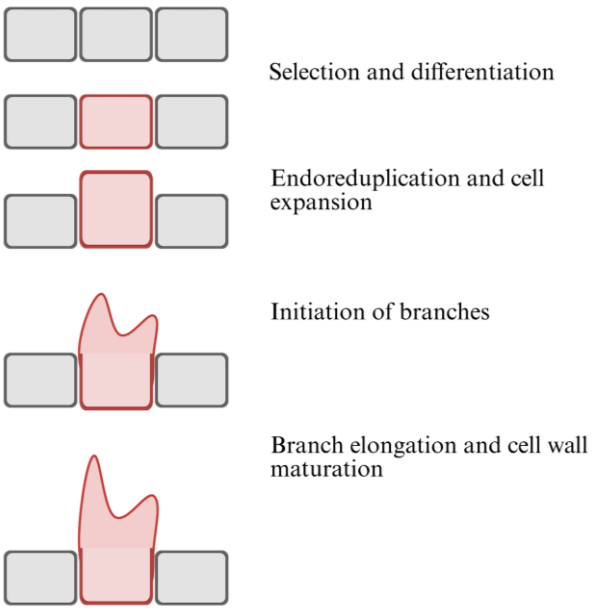

Fig. 1: Stages of leaf trichome development in *A. thaliana*.

Schematic representation of trichome development in *A. thaliana*. Trichome formation begins with selection and differentiation of a single epidermal cells followed by repeated rounds of endoreduplication, leading to increased nuclear DNA content and cell expansion. Subsequently, branch initiation occurs at defined positions on the trichome surface, followed by branch elongation and maturation of the cell wall. Adapted from Hülskamp, 2019. Created with BioRender.

Trichome development proceeds through distinct stages including cell fate specification, endoreduplication, cell expansion and branch formation. Following specification, trichome precursor cells exit the mitotic cell cycle and undergo repeated rounds of endoreduplication, resulting in increased nuclear DNA content and cell enlargement (Hülskamp, 2004; Szymanski & Marks, 1998). As development progresses, lateral branches are initiated at defined positions on the cell surface. Mature trichomes typically develop three branches, although this number can vary depending on genetic and environmental conditions (Folkers et al., 1997).

Because the entire branched structure forms within a single cell, trichomes provide an experimentally tractable system for analysing how polarized growth and intracellular organization generate complex cellular architectures (Hülskamp, 2004; Szymanski et al., 2000).

1.3 Trichome branching is controlled by the cytoskeleton

Branch formation represents one of the most characteristic features of leaf trichomes in *A. thaliana*. These branches are formed in a distinct direction and pattern, indicating a highly controlled initiation process (Hülskamp, 2004; Mathur, 2006). Genetic and cell biological studies have revealed that trichome branching is controlled by the coordinated action of multiple regulatory pathways, including cytoskeletal organization, cell cycle regulation, and membrane trafficking (Hülskamp, 2004; Szymanski et al., 2000). Even though these pathways have been intensively studied over the past decades, it is still not fully resolved how trichome branching is regulated.

The cytoskeleton plays a central role in the establishment and maintenance of trichome branch architecture (Fig. 2). As a basic principle, two coupled systems are identified: a) microtubules dictate cellulose fiber orientation, leading to mechanical anisotropy of the cell wall and b) actin is responsible for vesicle transport and cell wall component distribution. Growth is a result of an interplay between cell wall mechanics (microtubules) and component distribution (actin) (Li et al., 2019).

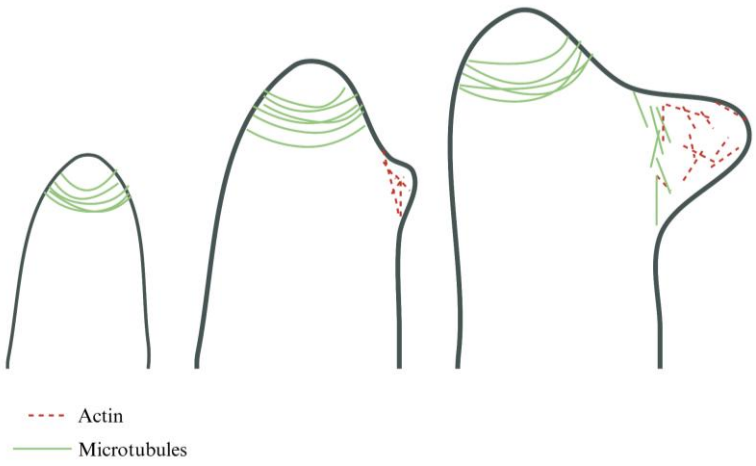

Fig. 2: Model for cortical microtubule and actin function in trichome branching.

During trichome branching, a cortical microtubule collar (green) forms at the branch site. The primary tip elongates, but the marked spot develops into a bulge. F-actin (red) is present in the newly formed bulge before microtubules form a collar again. Figure modified from Sambade et al., 2014. Created with BioRender.

Sambade et al., 2014 demonstrated by live-imaging that before branch initiation, a cortical microtubule collar forms near the trichome tip, marking the future branching site. A branch bulge then develops just below this collar and surprisingly contains little or no microtubules.

The authors conclude that microtubules mark positions of new branches rather than driving outgrowth. During branching, the trichome apex continues to elongate via tip growth (Sambade et al., 2014). Consistently, earlier studies reported that changes in microtubule organization correlate with branch initiation sites, indicating that microtubule dynamics contribute to defining sites of polarized growth (Mathur, 2005; Szymanski et al., 2000). Genetic evidence supporting the importance of microtubules in trichome morphogenesis comes from mutants affecting microtubule-associated proteins. For example, mutations in the kinesin-like calmodulin-binding protein ZWICHEL lead to defects in branch formation and result in trichomes with reduced or abnormal branching patterns, indicating that microtubule-based motor activity contributes to the proper organization of cytoskeletal structures required for branch development (Oppenheimer et al., 1997; Szymanski et al., 2000).

After bulging, a new microtubule collar forms *de novo* at the bulge base. It becomes narrow and defines the branch. The microtubule collar results in a gradient in cellulose orientation and therefore also in cell wall stiffness. The branch develops at the corner of this gradient proximal to the collar. It is important to note that only cortical and no endoplasmic microtubule arrays are involved in this process (Sambade et al., 2014).

The “gap” of cytoskeletal organization during branching is filled by actin. The microscopic live-cell imaging of Sambade et al., 2014 shows that before bulging, no actin signal is visible. Only when the bulge develops, F-actin accumulates at the center. Later on, actin forms an apical cap and a kind of cable to the inner cell. Therefore, it can be concluded that actin plays a key role in forming and growth of trichome branches.

During branch growth, microtubules are initially oriented transversely to the growth axis and later reorganize into helical arrays, contributing to anisotropic cell expansion through their influence on cellulose orientation (Sambade et al., 2014). At the tip of the growing branch, a microtubule depletion zone (MDZ) is present and is flanked by transversely oriented microtubules. The MDZ is associated with a high amount of organized cellulose, corresponding to a more isotropic cell wall structure. Together with the surrounding regions, this organization contributes to the formation of a tapered branch morphology (Li et al., 2019).

At the tip of the tapered branch, ARP (actin-related protein) 2/3-dependent actin forms an apical network (Li et al., 2019). The ARP2/3 complex is highly conserved in plants and attaches new actin subfragments to existing filaments, often referred to as “daughter” and “mother”

fragments, respectively. The complex alone is inactive and needs nucleation-promoting-factors (NPFs) for activation. In plants, activation mainly takes place via the WAVE/SCAR complex (reviewed in Jelínková et al., 2026). The resulting actin networks are involved in intracellular transport processes that deliver vesicles, membrane components and cell wall materials to sites of active growth (Mathur, 2005; Szymanski et al., 2000; Xu et al., 2024). Mutations affecting actin regulatory complexes frequently cause severe defects in trichome morphology, including reduced branching or distorted cell shapes. In particular, components of the ARP2/3 complex and its regulatory factors have been shown to control actin filament nucleation during trichome development, highlighting the importance of actin-mediated trafficking for localized cell expansion (Jelínková et al., 2026; Le et al., 2003; Szymanski et al., 1999).

1.4 Genetic regulators modulating trichome branch number

In *A. thaliana*, trichome branch number is genetically controlled by multiple loci that either promote or restrict branching, often in association with pathways that link cytoskeletal organization, cell cycle progression and localized cell expansion (Hülskamp, 2004). Mutations resulting in reduced branching reveal positive regulators of branch initiation, whereas over-branched phenotypes identify negative regulators or modulators of developmental timing.

At the transcriptional level, trichome initiation and endoreduplication are controlled by the MYB-bHLH-WD40 activator complex consisting of GLABRA1 (GL1), GLABRA3/ENHANCER OF GLABRA3 (GL3/EGL3) and TRANSPARENT TESTA GLABRA1 (TTG1) (Hülskamp et al., 1994; Zhao et al., 2008). This activator complex positively regulates trichome differentiation and promotes endoreduplication, which is strongly correlated with branch number (Pattanaik et al., 2014).

Positive regulators such as *STICHEL* (*STI*) and the uncharacterized *BRANCHLESS TRICHOMES* (*BLT*) are required for branch initiation (Hülskamp et al., 1994). Loss-of-function mutations in either gene result in strongly reduced or completely absent branching, even in genetic backgrounds that normally promote increased branch formation (Kasili et al., 2011; Marks et al., 2009). Epistasis analyses indicate that these regulators are organized in a hierarchical manner, in which branch initiation represents a genetically distinct and essential step that cannot be bypassed by mutations increasing branch number (Kasili et al., 2011; Marks et al., 2009). In double mutant analyses, combinations of hypomorphic *sti* and *blt* alleles can

produce intermediate branching phenotypes, suggesting partial functional overlap or participation in a shared regulatory module. In contrast, null alleles result in a complete loss of branching, indicating that both proteins are essential components of the branch initiation pathway (Marks et al., 2009). Additional evidence for a functional relationship between *STI* and *BLT* was provided by the characterization of two novel *sti* alleles and subsequent interaction analyses. The N-terminal region of STI was shown to interact directly with BLT, while mutations within this region caused severe branch initiation defects, supporting the idea that *STI* and *BLT* function together during early trichome morphogenesis (Xi et al., 2018).

SPIRRIG (*SPI*) displays a "distorted" gene and its mutant has not only less, but also deformed or irregular branches (Saedler et al., 2009). Distorted mutants normally define a class of genes required for proper actin-dependent cell morphogenesis in *Arabidopsis* trichomes (Szymanski, 2005). The WD/BEACH-domain protein SPI is no typical actin nucleator, but stabilizes microtubules and seems to work together with ZWICHEL (ZWI/KCBP), a kinesin-related motor protein (L. Chen et al., 2016; Folkers et al., 1997; Saedler et al., 2009). The latter is known to bind to microtubules and also to actin, which makes it a linker protein in cytoskeletal arrangement. *zwi* mutants show less and deformed trichome branches and reduced branch elongation (L. Chen et al., 2016). Double mutants of *spi* and *zwi* are almost branchless, indicating their function in the same pathway (Niu et al., 2024). Biochemical and genetic analyses further showed that ZWI interacts with microtubule-associated proteins involved in microtubule stabilization and organization (L. Chen et al., 2016). One such factor is TRICHOME CELL SHAPE1 (TCS1), a microtubule-binding protein that promotes microtubule assembly and stability. *tcs1* mutants exhibit reduced branch number and increased sensitivity to microtubule-disrupting drugs, while genetic analyses demonstrated that *zwi* is epistatic to *tcs1* with respect to trichome branch number (L. Chen et al., 2016).

Further microtubule-associated regulators include the microtubule-severing protein FRAGILE FIBER2 (FRA2) and the CTD-kinesin ANGUSTIFOLIA (AN). Mutations in *FRA2* reduce trichome branch number, supporting a role for regulated microtubule severing during branch formation (Li et al., 2019). *AN* mutants typically form fewer branches and were genetically interpreted as defects in secondary branching specification (Folkers et al., 1997).

In contrast, mutants with over-branched trichomes frequently arise from disruption of genes that act as negative regulators of branch formation or modulate endoreduplication. The R3-MYB-protein TRIPTYCHON (TRY*)* functions as such a negative regulator that limits branch

number and influences trichome patterning in competing with GL1 for interaction with GL3/EGL3 (Pattanaik et al., 2014; Schnittger et al., 1999). The *try* mutant also produces trichomes with elevated nuclear DNA content, linking endoreduplication with branching events (Hülskamp et al., 1994; Szymanski & Marks, 1998). In *sti try* double mutants, loss of TRY does not restore branching in strong *sti* alleles, indicating that STI function is required upstream of branch formation (Folkers et al., 1997). Weak *sti* alleles may show partial restoration of branching depending on gene dosage when combined with *try* mutants, suggesting that TRY primarily modulates branching downstream or in a parallel pathway and branch initiation and branch modulation can be genetically separated (Ilgenfritz et al., 2003).

Further evidence for an endoreduplication-independent *STI* pathway was provided by the characterization of *GLABROUS INFLORESCENCE STEMS* (*GIS*). *gis* mutants display increased trichome branch numbers despite unchanged nuclear DNA content, indicating that GIS regulates branching independently of ploidy levels (An et al., 2012). Genetic and expression analyses further suggested that *GIS* acts downstream of *STI* and connects *STI*-dependent branch regulation with gibberellic acid signaling pathways (An et al., 2012).

Other over-branching mutants such as *kaktus* (*kak*), *rastafari* (*rfi*) and *polychome* (*pym*) also produce trichomes with supernumerary branches, often accompanied by increased endoreduplication, further supporting the association between DNA content and branch number (Perazza et al., 1998, 1999).

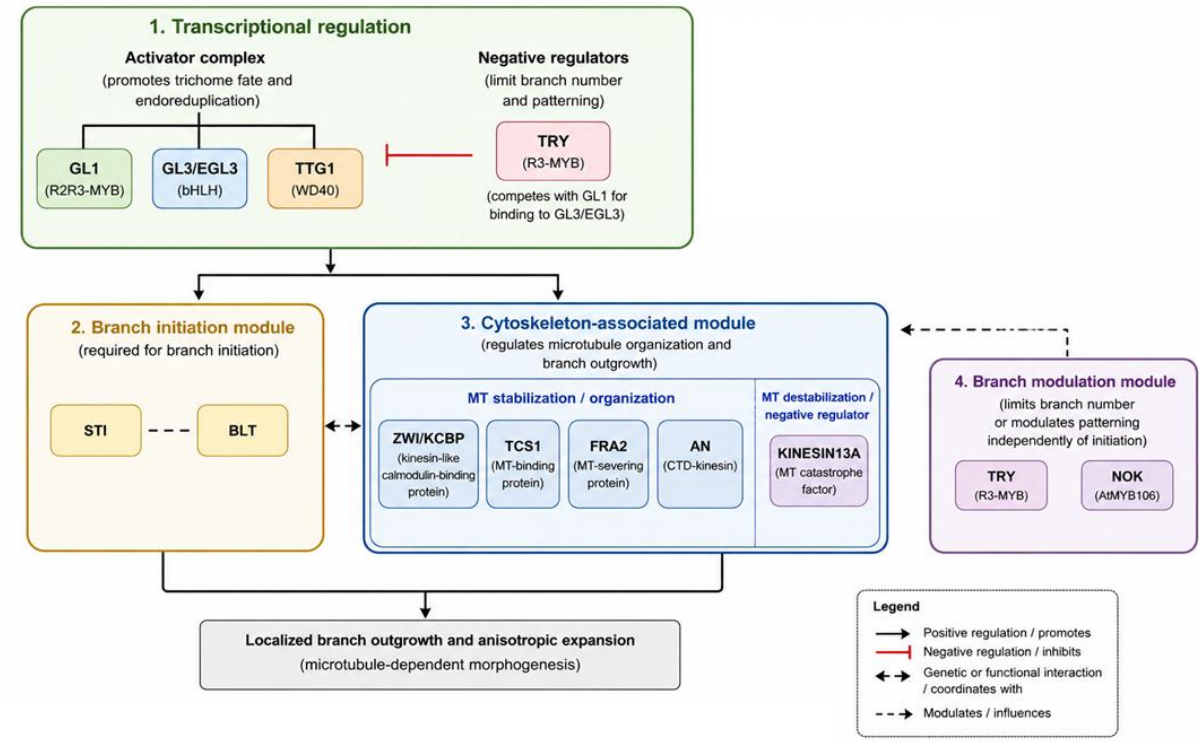

Fig. 3: Interacting genetic modules controlling trichome morphogenesis and branch initiation in *A. thaliana*.

This model summarizes current knowledge from genetic and molecular studies. The activator complex positively regulates trichome differentiation and promotes endoreduplication, which correlates with branch number. Direct hierarchical relationships between the branch initiation module (STI/BLT) and the cytoskeletal module (ZWI, FRA2, AN, KINESIN13A) have not been demonstrated. Developed based on Chen et al., 2016; Folkers et al., 1997; Gilding & Marks, 2010; Hülskamp et al., 1994; Ilgenfritz et al., 2003; Kasili et al., 2011; Li et al., 2019; Niu et al., 2024; Pattanaik et al., 2014; Payne et al., 2000; Saedler et al., 2009; Sambade et al., 2014; Schnittger et al., 1999; Schwab et al., 2000; Stracke et al., 2001.

In contrast to positive regulators of microtubule stabilization, KINESIN13A acts as a putative microtubule catastrophe factor. *kinesin13a* mutants exhibit increased trichome branch numbers, suggesting that local microtubule destabilization negatively regulates branch initiation frequency (Li et al., 2019). The precise signalling mechanisms controlling KINESIN13A activity during trichome morphogenesis, however, remain unresolved.

noek (*nok*) mutants exhibit increased branch numbers without a corresponding increase in endoreduplication, further indicating that branching can be regulated independently of ploidy levels (Folkers et al., 1997). *NOK*, also known as *AtMYB106*, was originally identified as a member of the *Arabidopsis R2R3-MYB* gene family (Stracke et al., 2001) and later functionally characterized as a MIXTA-like transcription factor regulating epidermal cell differentiation and

trichome branching (Gilding & Marks, 2010). Double mutant analyses with *sti* demonstrate that strong *sti* alleles remain largely unbranched even in the absence of *NOK* function. In weaker allele combinations, partial restoration of branching can occur, resulting in intermediate phenotypes. These observations indicate that *STI* is required for branch initiation, whereas *NOK* modulates branching extent and pattern (Folkers et al., 1997).

Despite these insights, the molecular mechanisms by which these genetic pathways are translated into spatially restricted growth remain poorly understood. In particular, it is unclear how proteins required for branch initiation are linked to cytoskeletal organization and membrane-associated processes at sites of branch formation.

Taken together trichome branch formation is controlled by at least two functionally distinct but interacting modules:

A **branch initiation module**, requiring the positive regulators *STI* and *BLT*

A **branch modulation module**, involving negative regulators such as *TRY* and *NOK*

Positive regulators are essential for the initiation of branching, and their loss cannot be compensated by mutations that increase branch number. In contrast, negative regulators influence the extent and pattern of branching but do not override the requirement for branch initiation factors.

1.5 *STICHEL*: A key regulator of trichome branching

The *STI* gene was identified as a principal genetic determinant of trichome branch number in *A. thaliana*. Positional cloning and sequencing of multiple independent *sti* alleles confirmed that mutations in a single locus result in a loss of trichome branching, with alleles showing variable effects on branch formation depending on the nature and position of the mutation in the coding sequence (Ilgenfritz et al., 2003). Northern blot analysis demonstrated that *STI* transcripts are detectable in a range of tissues, including roots, stems, leaves and siliques, indicating a ubiquitous expression pattern. This widespread transcript presence also extends to *gl1* mutant plants, which lack trichomes entirely, suggesting that *STI* mRNA expression is not limited to trichome cells. However, because *Arabidopsis* contains at least one closely related homolog (AT1G14460) with similarity in the conserved domain, cross hybridization of probes cannot be fully excluded when interpreting these northern blot results (Ilgenfritz et al., 2003).

1.5.1 Limitations of the constitutive GFP-STI reporter system

Given the absence of alterations in DNA content and the lack of homology to known transcription factor families, subcellular localization studies were undertaken to gain insight into the cellular context of STI function. A transgenic line expressing an N-terminal GFP-STI fusion protein driven by the constitutive Cauliflower mosaic virus 35S promoter was able to complement the trichome branching defect of *sti* mutants, demonstrating that the fusion protein is functional *in vivo* (Ilgenfritz et al., 2003). However, although the reporter line has branched trichomes, it still displays a phenotype, as the trichomes are wavy and distinguishable from the wild type (Fig. 4).

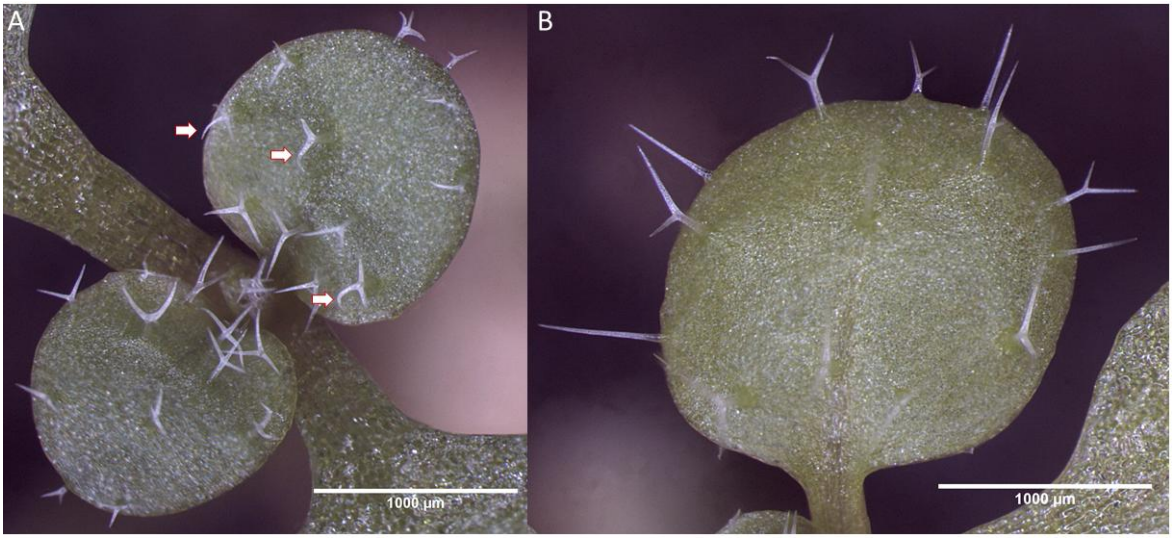

Fig. 4: Trichome phenotypes observed in transgenic *Arabidopsis* plants expressing the 35S::GFP-STI construct.

A: Representative examples of abnormal trichome morphology observed. Red arrows indicate malformed or irregularly branched trichomes. B: Example of incomplete complementation of the *sti* mutant phenotype by 35S::GFP-STI expression. While branched trichomes were partially restored (two instead of three branches), several trichomes still displayed unbranched trichomes. Scale bars = 1000 µm.

Confocal microscopy revealed that GFP-STI accumulates at sites of emerging trichome branches in young trichomes rather than being concentrated in nuclei (Fig. 5), despite the presence of predicted nuclear localization signals in the protein sequence (Ilgenfritz et al., 2003). Fluorescence is most prominently observed in youngest developing trichomes and decreases already at the second branch initiation site. Adult trichome stages almost completely lack GFP-STI. In a plasmolysis study, GFP-STI was clearly located at the plasma membrane (Herrmann, 2007). These expression and localization analyses suggest that STI may act at

specific subcellular sites to regulate the early stages of branch formation, rather than functioning primarily through modulating endoreduplication or general cell cycle progression.

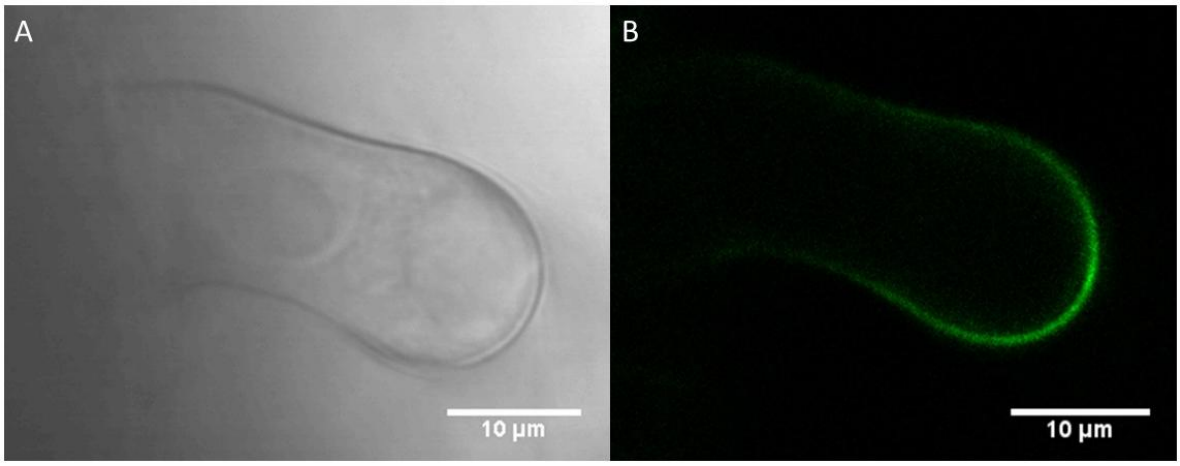

Fig. 5: Localization of GFP-STI during early trichome development.

A: bright-field image of a developing *A. thaliana* trichome at an early stage of morphogenesis. B: Fluorescence microscopy of the same cell expressing 35S::GFP-STI. The GFP signal is enriched at the cell cortex

The signal intensity of the reporter line was close to the detection limit of the experimental setup, even though this line was selected because it showed the best signal (Herrmann, 2007). The latter author was not able to recreate this fluorescent line and all experiments with other fluorophores, backgrounds and fusion directions were unsuccessful in the past decades.

Since a functional line with a strong fluorescent signal is a crucial tool for analysing expression and localisation of STI, a main aim of this study focuses on generating a new reporter line.

1.5.2 Structural features and functional implications of STICHEL

The STI protein consists of 1,218 amino acids and contains a single prominent conserved region embedded within an otherwise poorly characterized sequence (Ilgenfritz et al., 2003). This central domain, spanning approximately amino acids 449-799, shows detectable similarity to bacterial DNA polymerase III γ subunits, which function in clamp loading during DNA replication. This observation suggests a potential relationship to proteins associated with the AAA^+ ATPase superfamily, although STI does not exhibit the canonical domain architecture of well-characterized AAA^+ proteins (Erzberger & Berger, 2006). In addition, two PEST motifs (amino acids 273-304 and 425-449) and three predicted nuclear localization signals (NLS),

including one in the N-terminal region and two located in the C-terminal region, have been described (Ilgenfritz et al., 2003), see Fig. 6.

AAA$^+$ ATPases represent a conserved family of proteins that typically couple ATP binding and hydrolysis to conformational changes, thereby enabling the remodelling of macromolecular complexes (Erzberger & Berger, 2006; Hanson & Whiteheart, 2005). However, sequence similarity alone does not allow direct conclusions about biochemical activity or molecular function, particularly in multidomain proteins that may have diverged from canonical family members. Up to now, no experimental evidence supports a role for STI in DNA replication or canonical ATPase activity. Consistent with this, *sti* mutants do not display altered levels of endoreduplication or other phenotypes typically associated with defects in DNA replication or cell cycle regulation (Ilgenfritz et al., 2003). However, constructs with point mutations in the ATP binding motif (STI^{E574Q})[1], a presumed ATP hydrolysis motif (STI^{K619A}) or both (STI$^{E574Q/K619A}$)[2] were transformed under the constitutive 35S promoter into the *sti* mutant. The assignment of K619 as a residue associated with ATP hydrolysis appears to have been incorrect. None of the constructs were able to rescue the phenotype. It must be noted that transformation of the unmutated *STI* did also not consistently rescue the *sti* phenotype (Huang, 2008).

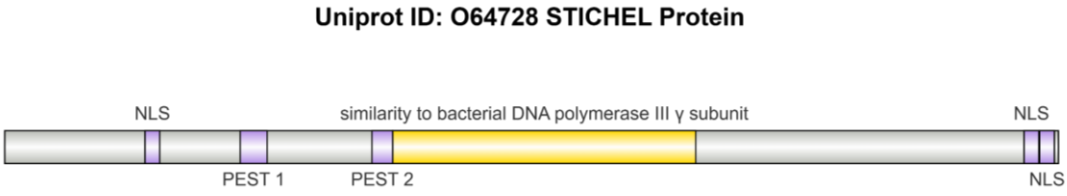

Fig. 6: STI annotation according to UNIPROT and Ilgenfritz et al., 2003.
Motifs and domains annotated based on current information published.

Given the limited functional annotation of STI, experimental approaches are required to elucidate its molecular role and to identify potential interaction partners involved in trichome branch initiation. Since previous approaches were not sufficient or even showed ambiguous

[1] Reported as STI^{E573Q} in Huang, 2008, corrected here according to the actual amino acid position.

[2] Reported as STI$^{E573Q/K619A}$ in Huang, 2008, corrected here according to the actual amino acid position.

results, this study focuses on the expression of the STI ATPase domain and testing its ATPase activity *in vitro*.

1.6 NETWORKED (NET) proteins and actin-membrane interactions in plant cell morphogenesis

The spatial organization of the actin cytoskeleton is a central determinant of plant cell morphogenesis, particularly in processes that require localized cell expansion such as tip growth and branch formation. In *A. thaliana*, members of the NETWORKED (NET) protein family have been identified as plant-specific actin-binding proteins that function at the interface between the actin cytoskeleton and membrane compartments (Deeks et al., 2012).

NET proteins are characterized by a conserved N-terminal actin-binding domain, referred to as the NET actin-binding (NAB) domain, which is sufficient for direct interaction with filamentous actin (F-actin). This domain defines a unique, evolutionarily conserved protein family specific to the plant lineage (Deeks et al., 2012). Among the NET family members, NET1A, NET1B, NET1C and NET1D form a closely related subgroup that localizes to membrane-associated cortical regions and plasmodesmata. Fluorescent protein fusions revealed that NET1 associates with filamentous structures underlying the plasma membrane and exhibit a pattern consistent with cortical actin networks (Deeks et al., 2012). This localization supports the hypothesis that NET1 proteins may contribute to the stabilization and spatial organization of cortical actin arrays by linking them to membrane sites.

A large-scale yeast two-hybrid assay revealed NET1 to interact with STI fragments (Huang, 2008). At the time of publication, only gene numbers were available and corresponding proteins were listed as “unknown protein”. Specifically, AT3G22790, today identified as *NET1A*, interacted with an N-terminal S1 fragment of STI. *NET1B* (AT4G14760) also interacted with the same fragment, as well as with the C-terminal S3 fragment of STI. *NET1D* (AT1G03080) was found to interact only with the S1 fragment. Interestingly, *NET1C* (AT4G02710) was not detected as an interaction partner of any STI fragment (Fig. 7). Besides the study of Huang, 2008, there is no published evidence of interaction. The aim of this study is thus to first confirm the interaction of NET1 and STI and, if possible, restrict it to a certain part of the proteins.

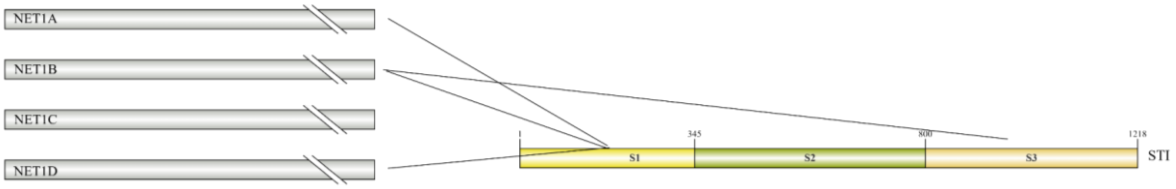

Fig. 7: Identification of interactions in the yeast-two-hybrid study in Huang, 2008.

The STI S1 fragment was found to interact with NET1A, NET1B and NET1D. The STI S3 fragment was found to interact with NET1B. No interaction for NET1C was detected

Given that localized reorganization of the actin cytoskeleton is required for the initiation of cellular outgrowths such as trichome branches (Mathur et al., 1999; Szymanski, 2005; Szymanski et al., 1999), proteins that mediate the attachment of actin filaments to membrane compartments are likely to play an important role in defining sites of branch initiation and directional growth (Deeks et al., 2012; Smith & Oppenheimer, 2005). A recent study focusing on NET3 revealed a multiprotein complex linking F-actin, microtubules and the endoplasmic reticulum (ER) at ER-plasma membrane contact sites (Duckney et al., 2025). These findings illustrate how members of the NET protein family can participate in the spatial organization of the cytoskeleton while simultaneously connecting membrane-associated compartments. Although comparable interaction networks have not been demonstrated for NET1 proteins, the possibility arises that NET1 family members may similarly contribute to localized cytoskeletal organization together with STI during trichome branch initiation. To investigate this possibility, this study investigates whether NET1 proteins interact with STI, which would be a prerequisite for the proposed mechanism.

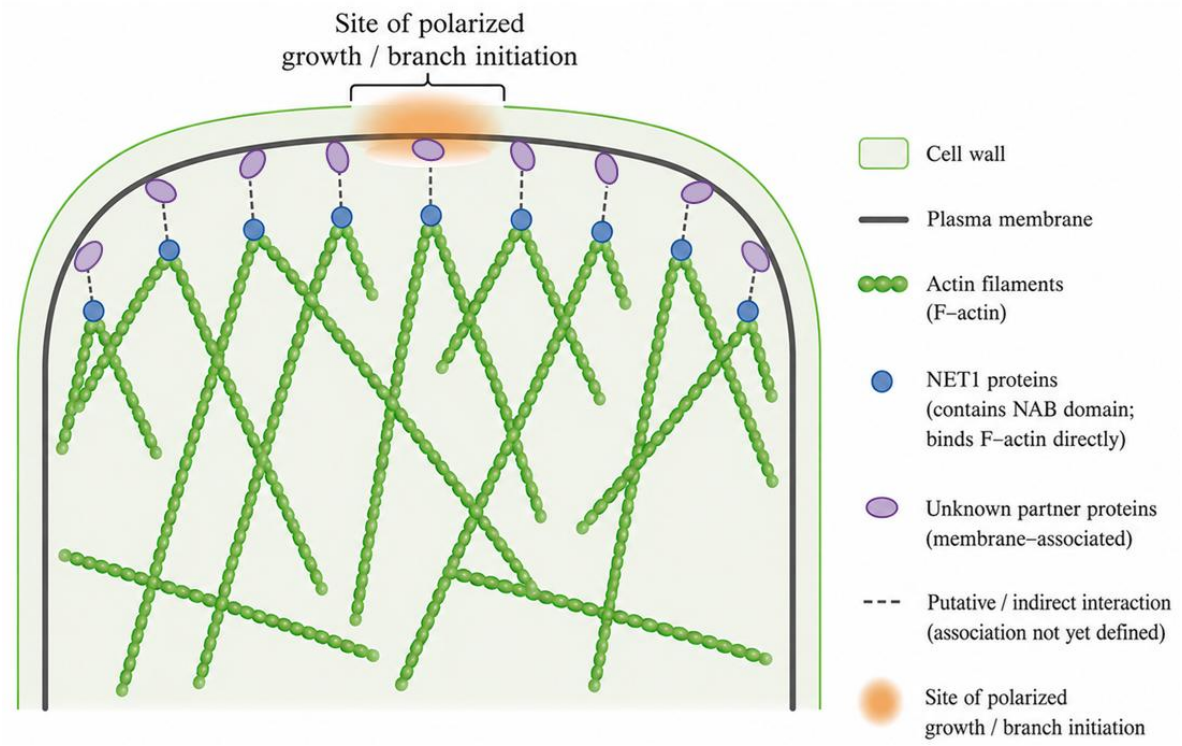

Fig. 8: Schematic putative model of NET1-mediated cortical actin organization at sites of polarized growth and branch initiation.

NET1 proteins localize to cortical regions beneath the plasma membrane and bind directly to F-actin via their conserved NAB domain (Deeks et al., 2012). Association of NET1 proteins with the plasma membrane is likely indirect and may involve additional membrane-associated partner proteins that are not yet molecularly defined (Duckney et al., 2025). Dashed lines indicate putative indirect interactions between NET1 proteins and membrane-associated factors. For simplicity, NET1 proteins are shown at terminal regions of selected actin filaments; however, there is currently no evidence that NET1 binding is restricted to filament ends. The model illustrates a possible contribution of NET1 proteins to the spatial organization of cortical actin arrays associated with sites of polarized growth and branch initiation and is based on current knowledge of NET family proteins and cortical actin association in plants (Deeks et al., 2012; Duckney et al., 2025; Hussey et al., 2006).

Although a direct role of NET1 proteins in trichome branching has not been demonstrated, their biochemical properties and subcellular localization suggest that they may contribute to the establishment of polarized growth domains. No clear trichome morphological phenotype has been reported for *net1* mutants, likely due to functional redundancy within the NETWORKED protein family (Deeks et al., 2012). Given the unresolved molecular function of STI and its proposed role in early branch initiation, proteins that link actin organization to membrane-associated processes represent plausible candidates for interaction partners. In this context, NET1 proteins constitute a relevant group of factors to investigate potential connections between STI function and cytoskeletal organization during trichome morphogenesis.

2 Aim of this study

Despite the identification of *STI* as a key regulator of trichome branch initiation, its molecular function remains unknown. This study is split in three parts to shed light on the molecular mechanism contributing to trichome branching, biochemical properties of the identified domains of the STI protein and to create a robust reporter line to investigate STI localization *in vivo*.

To examine STI structure, a comprehensive *in silico* approach using new bioinformatic tools including structure prediction was used to analyse the STI sequence. Based on new insights, such as identifying a potential structural AAA^+ ATPase domain, this specific domain was expressed in bacteria. Previous approaches could not clarify whether this domain is catalytically active (e.g. Huang, 2008), so this study aimed for a straightforward ATPase assay, testing the isolated domain itself. Proving that STI contains a functional AAA^+ ATPase *in vitro* would justify further investigation and hypothetical models in how this domain is responsible for active remodelling of structures that in the end lead to trichome branch formation.

Besides unknown biochemical properties, it is also unclear how STI is mechanistically linked to cytoskeletal organization and membrane-associated processes that underlie localized cell growth. A particular focus of this study was therefore placed on members of the NET1 protein family, which have been proposed to interact with STI and represent candidates for linking actin organization to membrane-associated processes. Protein-protein interaction assays and domain mapping strategies were used to identify interacting regions between STI and NET1 proteins. A robust interaction between STI and NET1 proteins would indicate a potential role in actin-dependent processes during branch morphogenesis.

The main focus of this study was to generate a new *STI* reporter line. This study aimed to generate two independent *STI* reporter lines, a T-DNA insertion line and a knock-in line generated via CRISPR/Cas9 genome editing. These lines should confirm STI localization *in vivo* and should provide a robust system allowing further investigation like interaction studies or time series of developing trichomes.

3 Material and Methods

3.1 Material

3.1.1 List of chemicals

Tab. 1: List of chemicals used in this study.

Chemical	Manufacturer
3-amino-1,2,3,4-triazole	Roth
Acetosyringon (Dimethoxy4-hydroxyacetophenon)	Sigma-Aldrich
Adenine	Sigma-Alderich
Adenosine 5'-triphosphate	Sigma-Aldrich
Agar (Micro agar)	Duchefa
Agar (Plant agar)	Duchefa
Agarose (LE Agarose)	Biozym
Aluminiumsulfat-(14-18)-Hydrat	Roth
Ammonium sulphate	Roth
Bacto-Peptone	Roth
Bacto-Yeast-Extract	Difco
BP enzyme mix	Thermo Fisher Scientific
Calcium chloride dihydrate (CaCl2*2H2O)	Sigma-Aldrich
CBB-G250	Sigma-Aldrich
DO Supplement w/o Leu Try His	Thermo Fisher Scientific
Dimethyl sulfoxide (DMSO)	Thermo Fisher Scientific
Dipotassium hydrogen phosphate (K2HPO4)	Roth
Disodium phosphate (Na2HPO4)	Roth
Ethylenediaminetetraacetic acid (EDTA)	Roth
Ethidium bromide	Roth
Ethanol (EtOH) absolute	VWR Chemicals
D-Glucose	Sigma-Aldrich
Difco peptone	VWR Chemicals
Glutamine	Sigma-Aldrich
Glycerol	Roth
Histidine	Sigma-Alderich
LiAc	Sigma-Alderich
LR enzyme mix	Thermo Fisher Scientific
NaOH	Roth
Magnesium sulfate heptahydrate	Roth
Maltose	Roth
Methanol	Roth
PEG 3350	VWR Chemicals
ortho- Phosphoric acid	Roth
Potassium chloride (KCl)	Roth
Potassium dihydrogen phosphate KH2PO4	Roth
Protease Inhibitor Cocktail (EDTA-free)	Roche
Sucrose	Roth
Tricine	Roth

Chemical	Manufacturer
Trypton	Roth
Yeast nitrogen base	Difco
Yeast extract	Difco

3.1.2 List of plasmids

Tab. 2: List of general plasmids used in this study.

Plasmid number	Plasmid	Description	Resistance	Publication/Origin
	pDONR201	Gateway entry vector	Kan	Invitrogen
HY001	pAMPAT	Gateway expression vector; p35S followed by GW cassette	Carb, Chlor	Based on GenBank ID AY436765
HY006	pDE-Cas9	Gateway expression vector, Cas9 expression cassette	Spec	Schiml et. al 2016
HY003	pEN-Chimera	Gateway entry vector; sgRNA expression system	Carb	Promega Corp., Fitchburg, WI, USA
HY039	pETG40a	Gateway expression vector, Gateway cassette followed by Maltose-binding-protein tag	Carb	Invitrogen
	pHEE401E	Egg cell-specific promoter-controlled expression of 3×FLAG-NLS-zCas9-NLS. Contains gRNA scaffold for GG insertion of target sequence (U6-26 promoter)	Hyg	Adgene
HY048	pAS	gateway expression vector, bait for yeast two-hybrid	Carb	Ilona Zimmermann
HY049	pACT	gateway destination vector, prey for yeast two-hybrid	Carb	Ilona Zimmermann
HY112	pEC1.2_EC1.1 spCas9_GFP	(Empty Backbone) CRISPR plasmid with spCas9 expressed under egg cell promoter - TagRFP seed selection	Kan	Addgene
HY120	pEC1.2_pEC1.1 Cas9i_TagRFP	(Empty Backbone) CRISPR plasmid with Cas9i expressed under egg cell promoter - TagRFP seed selection	Kan	Addgene
HY114	pEC1.2_pEC1.1 spCas9_TagRFP	(Empty Backbone) CRISPR plasmid with spCas9 expressed under egg cell promoter - TagRFP seed selection	Kan	Addgene
HY082	pMpGWB313	Gateway expression vector, Gateway cassette followed by tdTomato tag	Hyg	Addgene
HY002	pFAST-R06	Gateway destination vector, OLE1 RFP Tag for seed selection	Spec	Shimada et al., 2010

Tab. 3: List of specific plasmids used in this study.
For vector backbones/cloned originals see Tab. 2.

Plasmid number	Plasmid name	Description	Resistance	Publication/ Origin
HY090	pEN-Chimera PAM1	Donor vector with PAM1 (directs N-terminal cut in STI)	Kan	This study
HY091	pEN-Chimera PAM2	Donor vector with PAM2 (directs C-terminal cut in STI)	Kan	This study
HY007	pDE-Cas9 w/o promoter	HY006 without promoter of Cas9	Spec	This study
HY008	pDE-Cas9 w/o promoter w/o Cas9	HY007 without Cas9 gene	Spec	This study
HY009	pDE-Cas9 empty	HY008 without terminator of Cas9	Spec	This study
HY010	pDE-Cas9-empty w/o Basta	HY009 without BASTA resistance gene	Spec	This study
HY011	pDE-Cas9-OLE1	HY010 with OLE1 seed fluorescence cassette	Spec	This study
HY012	pUc GW- repair fragment PAM1	repair fragment for PAM1 CRISPR Cas experiment (STI tagged with tdTomato N-terminal) in PuC vector,	Kan	Genewiz gene synthesis service
HY013	pUc GW- repair fragment PAM2	repair fragment for PAM2 CRISPR Cas experiment (STI tagged with tdTomato c terminal) in PuC vector	Kan	Genewiz gene synthesis service
HY014	pET40a-STI CDS	STI CDS in pET40a (Maltose binding protein tag)	Carb	Dr. Lisa Stephan
HY038	pET40a STI ATPase extended	ATPase fragment of STI including predicted Domain in S3 in pET40a (Maltose binding protein tag)	Carb	This study
HY040	pET40a STI S2	STI S2 in pET40a (Maltose binding protein tag)	Carb	This study
HY041	pDONR201- STI S2	STI S2 CDS in pDONR201	Kan	Dr. Lisa Stephan
HY043	pDONR201- STI S3	STI S2 CDS in pDONR201	Kan	This study
HY053	pAS-STI	Y2H bait STI full length	Carb	This study
HY054	pACT-STI	Y2H prey STI full length	Carb	This study
HY055	pAS-STI S1	Y2H bait STI S1	Carb	This study
HY056	pAS-STI S2	Y2H bait STI S	Carb	This study
HY059	pACT-STI S1	Y2H prey STI S1	Carb	This study
HY060	pACT-STI S2	Y2H prey STI S2	Carb	This study
HY065	pACT-STI S3	Y2H prey STI S3	Carb	This study
HY077	pAS-STI S3	Y2H bait STI S3	Carb	This study
HY080	pDONR201-STI CDS + Introns+ STOP	STI CDS + Introns in donor vector with STOP Codon	Kan	Dr. Lisa Stephan
HY101	pDONR201-STI CDS + Introns w/o STOP	STI CDS + Introns in donor vector without STOP Codon	Kan	This study
HY094	pDE-Cas9 w/o Basta w/o OLE1-PAM1neu	LR HY090 and HY010, does not include repair fragment	Carb	This study

Plasmid number	Plasmid name	Description	Resistance	Publication/ Origin
HY095	pDECas9-expression clone PAM1neu (wo repair fragment)	LR HY011 + HY090, does not include repair fragment	Carb	This study
HY096	pDE-Cas9 w/o Basta w/o OLE1-PAM2neu	LR HY010+HY091, does not include repair fragment	Carb	This study
HY097	pDECas9-expression clone PAM2neu (wo repair fragment)	LR HY011 + HY091, does not include repair fragment	Carb	This study
HY098	pDECas9-PAM1neu+repair fragment	final CRIPSR clone, ligation repair fragment into HY095	Carb	This study
HY099	pDE-Cas9 w/o Basta w/o OLE1-PAM1neu+repair fragment	HY094+repair fragment PAM1	Carb	This study
HY100	pDECas9-PAM2neu+repair fragment	final CRIPSR clone, ligation repair fragment into HY097	Carb	This study
HY102	35S-GW td tomato-STI CDS+Introns w/o STOP	HY082 with STI CDS + Introns w/o STOP Codon	Carb	This study
HY115	pEC1.2_EC1.1 spCas9_GFP_STI_KO_N-terminal	HY112 + Protospacer for STI KnockOut n-terminal	Kan	This study
HY116	pEC1.2_EC1.1 spCas9_GFP_NOEK_KO_N-terminal	HY112 + Protospacer for NOK KnockOut n-terminal	Kan	This study
HY117	pEC1.2_EC1.1 spCas9_GFP_STI_KO_C-terminal	HY112 + Protospacer for STI KnockOut c-terminal	Kan	This study
HY118	HY114_PAM1	HY114 + Protospacer for tdTomato n-terminal Knock IN	Kan	This study
HY119	HY114_PAM2	HY114 + Protospacer for tdTomato c-terminal Knock IN	Kan	This study
HY121	HY120_PAM1	HY120 + Protospacer for tdTomato n-terminal Knock IN	Kan	This study
HY122	HY120_PAM2	HY120 + Protospacer for tdTomato c-terminal Knock IN	Kan	This study
HY123	pUC-GW-NET1B_CDS	NET1B CDS with attB sites in PuC vector	Kan	Genewiz gene synthesis service
HY124	pUC-GW-NET1C_CDS	NET1C CDS with attB sites in PuC vector	Kan	Genewiz gene synthesis service
HY125	pUC-GW-NET1D_CDS	NET1D CDS with attB sites in PuC vector	Kan	Genewiz gene synthesis service
HY160	pUc GW-repairfragment 1 mNeonGreen	repair fragment for Protospacer for CRISPR Cas experiment (STI tagged with mNeonGreen N-terminal) in PuC vector	Kan	Genewiz gene synthesis service
HY161	pUc GW-repairfragment 2 mNeonGreen	repair fragment for Protospacer cut CRISPR Cas experiment (STI tagged with mNeonGreen c terminal) in PuC vector,	Kan	Genewiz gene synthesis service
HY162	pUc GW-NET1A_NAB domain CDS	NET1A NAB Domain CDS with attL sites in PuC vector	Kan	Genewiz gene synthesis service
HY163	pUc GW-NET1C_NAB domain CDS	NET1C NAB Domain CDS with attL sites in PuC vector	Kan	Genewiz gene synthesis service

Plasmid number	Plasmid name	Description	Resistance	Publication/ Origin
HY198	HY118+repairfragment1mNeonGreen	final clone for CRISPR KI STI n-termtag, new repair fragment with mNeonGreen via Mfe/Spe ligation into HY118	Kan	This study
HY199	HY119+repairfragment2mNeonGreen	final clone for CRISPR KI PAM1 STI c-termtag, new repair fragment with mNeonGreen via Mfe/Spe ligation into HY119	Kan	This study
HY201	HY122+repairfragment2mNeonGreen	final clone for CRISPR KI PAM1 STI c-termtag, new repair fragment with mNeonGreen via Mfe/Spe ligation into HY122	Kan	This study
HY050	pDONR201-NET1A	NET1A CDS including intron of 170 bp in cterm3 in donor vector	Kan	This study
HY164	pDONR201-NET1A NAB CDS	NET1A NAB domain CDS in donor vector	Kan	This study
HY051	pDONR201-NET1A_cterm full	NET1A C-terminal CDS including 170 bp intron in cterm3 in donor vector	Kan	This study
HY165	pDONR201-NET1A C-terminal1 CDS	NET1A C-terminal 1 CDS in donor vector	Kan	This study
HY166	pDONR201-NET1A C-terminal2 CDS	NET1A C-terminal 2 CDS in donor vector	Kan	This study
HY167	pDONR201-NET1A C-terminal3 CDS	NET1A C-terminal 3 CDS including 170 bp intron in donor vector	Kan	This study
HY168	pAS-NET1A full length CDS	Y2H bait NET1A CDS including intron of 170 bp in cterm3	Carb	This study
HY169	pAS-NET1A NAB CDS	Y2H bait NET1A domain CDS	Carb	This study
HY170	pAS-NET1A C-terminal full CDS	Y2H bait NET1A C-terminal CDS including 170 bp intron in cterm3	Carb	This study
HY171	pAS-NET1A C-terminal1 CDS	Y2H bait NET1A C-terminal 1 CDS	Carb	This study
HY172	pAS-NET1A C-terminal2 CDS	Y2H bait NET1A C-terminal 2 CDS	Carb	This study
HY173	pAS-NET1A C-terminal3 CDS	Y2H bait NET1A C-terminal 3 CDS including 170 bp intron	Carb	This study
HY174	pACT-NET1A full length CDS	Y2H prey NET1A CDS including intron of 170 bp in cterm3	Carb	This study
HY175	pACT-NET1A NAB CDS	Y2H prey NET1A NAB domain CDS	Carb	This study
HY176	pACT-NET1A C-terminal full CDS	Y2H prey NET1A C-terminal CDS including 170 bp intron in cterm3	Carb	This study
HY177	pACT-NET1A C-terminal1 CDS	Y2H prey NET1A C-terminal 1 CDS	Carb	This study
HY178	pACT-NET1A C-terminal2 CDS	Y2H prey NET1A C-terminal 2 CDS	Carb	This study
HY179	pACT-NET1A C-terminal3 CDS	Y2H prey NET1A NAB C-terminal 3 CDS including 170 bp intron	Carb	This study
HY127	pDONR201-NET1B full length CDS	NET1B CDS in donor vector	Kan	This study
HY128	pDONR201-NET1B NAB CDS	NET1B NAB domain CDS in donor vector	Kan	This study
HY129	pDONR201-NET1B C-terminal full CDS	NET1B C-terminal CDS in donor vector	Kan	This study
HY130	pDONR201-NET1B C-terminal1 CDS	NET1B C-terminal 1 CDS in donor vector	Kan	This study
HY131	pDONR201-NET1B C-terminal2 CDS	NET1B C-terminal 2 CDS in donor vector	Kan	This study
HY132	pDONR201-NET1B C-terminal3 CDS	NET1B C-terminal 3 CDS in donor vector	Kan	This study
HY134	pAS-NET1B full length CDS	Y2H bait NET1B CDS	Carb	This study

Plasmid number	Plasmid name	Description	Resistance	Publication/ Origin
HY135	pAS-NET1B NAB CDS	Y2H bait NET1B NAB domain CDS	Carb	This study
HY136	pAS-NET1B C-terminal full CDS	Y2H bait NET1B C-terminal CDS	Carb	This study
HY137	pAS-NET1B C-terminal1 CDS	Y2H bait NET1B C-terminal 1 CDS	Carb	This study
HY138	pAS-NET1B C-terminal2 CDS	Y2H bait NET1B C-terminal 2 CDS	Carb	This study
HY139	pAS-NET1B C-terminal3 CDS	Y2H bait NET1B C-terminal 3 CDS	Carb	This study
HY140	pACT-NET1B full length CDS	Y2H prey NET1B CDS	Carb	This study
HY141	pACT-NET1B NAB CDS	Y2H prey NET1B NAB domain CDS	Carb	This study
HY142	pACT-NET1B C-terminal full CDS	Y2H prey NET1B C-terminal CDS	Carb	This study
HY143	pACT-NET1B C-terminal1 CDS	Y2H prey NET1B C-terminal 1 CDS	Carb	This study
HY144	pACT-NET1B C-terminal2 CDS	Y2H prey NET1B C-terminal 2 CDS	Carb	This study
HY145	pACT-NET1B C-terminal3 CDS	Y2H prey NET1B C-terminal 3 CDS	Carb	This study
HY180	pDONR201-NET1C full length CDS	NET1C CDS in donor vector	Kan	This study
HY181	pDONR201-NET1C NAB CDS	NET1C NAB domain CDS in donor vector	Kan	This study
HY182	pDONR201-NET1C C-terminal full CDS	NET1C C-terminal CDS in donor vector	Kan	This study
HY183	pDONR201-NET1C C-terminal1 CDS	NET1C C-terminal 1 CDS in donor vector	Kan	This study
HY184	pDONR201-NET1C C-terminal2 CDS	NET1C C-terminal 2 CDS in donor vector	Kan	This study
HY185	pDONR201-NET1C C-terminal3 CDS	NET1C C-terminal 3 CDS in donor vector	Kan	This study
HY186	pAS-NET1C full length CDS	Y2H bait NET1C CDS	Carb	This study
HY187	pAS-NET1C NAB CDS	Y2H bait NET1C NAB domain CDS	Carb	This study
HY188	pAS-NET1C C-terminal full CDS	Y2H bait NET1C C-terminal CDS	Carb	This study
HY189	pAS-NET1C C-terminal1 CDS	Y2H bait NET1C C-terminal 1 CDS	Carb	This study
HY190	pAS-NET1C C-terminal2 CDS	Y2H bait NET1C C-terminal 2 CDS	Carb	This study
HY191	pAS-NET1C C-terminal3 CDS	Y2H bait NET1C C-terminal 3 CDS	Carb	This study
HY192	pACT-NET1C full length CDS	Y2H prey NET1C CDS	Carb	This study
HY193	pACT-NET1C NAB CDS	Y2H prey NET1C NAB domain CDS	Carb	This study
HY194	pACT-NET1C C-terminal full CDS	Y2H prey NET1C C-terminal CDS	Carb	This study
HY195	pACT-NET1C C-terminal1 CDS	Y2H prey NET1C C-terminal 1 CDS	Carb	This study
HY196	pACT-NET1C C-terminal2 CDS	Y2H prey NET1C C-terminal 2 CDS	Carb	This study
HY197	pACT-NET1C C-terminal3 CDS	Y2H prey NET1C C-terminal 3 CDS	Carb	This study
HY146	pDONR201-NET1D full length CDS	NET1D CDS in donor vector	Kan	This study
HY046	pDONR201-NET1D_NAB domain	NET1D NAB domain CDS in donor vector	Kan	This study
HY047	pDONR201-NET1D_cterm	NET1D C-terminal CDS in donor vector	Kan	This study

Plasmid number	Plasmid name	Description	Resistance	Publication/ Origin
HY147	pDONR201-NET1D C-terminal1 CDS	NET1D C-terminal 1 CDS in donor vector	Kan	This study
HY148	pDONR201-NET1D C-terminal2 CDS	NET1D C-terminal 2 CDS in donor vector	Kan	This study
HY149	pDONR201-NET1D C-terminal3 CDS	NET1D C-terminal 3 CDS in donor vector	Kan	This study
HY150	pAS-NET1D full length CDS	Y2H bait NET1D CDS	Carb	This study
HY151	pAS-NET1D NAB CDS	Y2H bait NET1D NAB domain CDS	Carb	This study
HY152	pAS-NET1D C-terminal1 CDS	Y2H bait NET1D C-terminal 1 CDS	Carb	This study
HY153	pAS-NET1D C-terminal2 CDS	Y2H bait NET1D C-terminal 2 CDS	Carb	This study
HY154	pAS-NET1D C-terminal3 CDS	Y2H bait NET1D C-terminal 3 CDS	Carb	This study
HY155	pACT-NET1D full length CDS	Y2H prey NET1D CDS	Carb	This study
HY156	pACT-NET1D NAB CDS	Y2H prey NET1D NAB domain CDS	Carb	This study
HY157	pACT-NET1D C-terminal1 CDS	Y2H prey NET1D C-terminal 1 CDS	Carb	This study
HY158	pACT-NET1D C-terminal2 CDS	Y2H prey NET1D C-terminal 2 CDS	Carb	This study
HY159	pACT-NET1D C-terminal3 CDS	Y2H prey NET1D C-terminal 3 CDS	Carb	This study

3.1.3 List of oligonucleotides

All oligo nucleotides listed as “this study” were were synthesised by Sigma (http://www.sigmaaldrich.com/DE/de/product/sigma/oligo).

Tab. 4: List of oligo nucleotides used in this study.

Oligo nucleotide	Sequence 5' to 3'	Provided by
HJ001_SS42	TCCCAGGATTAGAATGATTAGG	Dr. S. Schellmann
HJ002_SS43	CGACTAAGGGTTTCTTATATGC	Dr. S. Schellmann
HJ003_SS62	GAGCTCCAGGCCTCCCAGCTTTCG	Dr. S. Schellmann
HJ004_SS129 (M13)	CACAGGAAACAGCTATGAC	Dr. S. Schellmann
HJ005_SS102	CACCATGTTATCACATCAATCC	Dr. S. Schellmann
HJ024_fw (M13)	TGTAAAACGACGGCCAGT	Dr. S. Schellmann
HJ025_rev	ATCCCAAAGAGTGTAGCTTTGA	Dr. L. Stephan
HJ027_attb_STI-AAATPase_short_fw	GGGGACAAGTTTGTACAAAAAAGCAGGCTTAGTAATCCCAGCACTGTTGGA	This study
HJ031_attb_STI-AAATPase_long_rev	GGGGACCACTTTGTACAAGAAAGCTGGGTAGTTGGTCATTTCTGGTTTCC	This study
HJ047_ATPaseupdated_attb_fw	GGGGACAAGTTTGTACAAAAAAGCAGGCTTAAAGTACAGACCAATGTTTTT	This study
HJ048_ATPaseupdated_attb_rev	GGGGACCACTTTGTACAAGAAAGCTGGGTTTTGGTGAGGGACAACGAGTA	This study
HJ054_STI_CDS_attb_fw	GGGGACAAGTTTGTACAAAAAAGCAGGCTTAATGTCAGGTTCGAGAGTTTC	This study

Oligo nucleotide	Sequence 5' to 3'	Provided by
HJ055_STI_CDS_attb_rev	GGGGACCACTTTGTACAAGAAAGCTGGGTTTCATCTTCTAATGTTACCTT	This study
HJ056_attB1	ACAAGTTTGTACAAAAAAGCAGGCT	Dr. H. Bechtel
HJ057_attB2	ACCACTTTGTACAAGAAAGCTGGGT	Dr. H. Bechtel
HJ058_n-tag STI seq fw	AGGTAAGCATTCTATTCTACCATATACAAATA	This study
HJ059_n-tag STI seq rev	AATTACTCAATTCCTCCTCTGT	This study
HJ060_c-tag STI seq fw	GAAGAGTCGGTTCTCTCTGT	This study
HJ061_c-tag STI seq fw	GTTTGTCGCGGAGAATAAATTATA	This study
HJ062_c-tag STI seq fw	GAAACCGCTTGGTTACAAAC	This study
HJ063_c-tag STI seq fw	TAAGTTCTTTAGTCATGAAAAACAAAATT	This study
HJ064_c-tag STI seq rev	TATAATTTATTCTCCGCGACAAAC	This study
HJ065_c-tag STI seq fw_long	TTCGCGGAGAAATCGGAAGAGTCGGTTC	This study
HJ066_c-tag STI seq rev_long	TATAATTTATTCTCCGCGACAAACCCTTTG	This study
HJ067_c-tag STI seq rev_long	AATTTTGTTTTTCATGACTAAAGAACT	This study
HJ068_NET1A_CDS_attb_fw	GGGGACAAGTTTGTACAAAAAAGCAGGCTTAATGGCTACTGTCTTGCACTC	This study
HJ069_NET1A_CDS_attb_rev	GGGGACCACTTTGTACAAGAAAGCTGGGTTCTACTCTTCATTACCGGAAG	This study
HJ070_NET1A_NAB_attb_rev	GGGGACCACTTTGTACAAGAAAGCTGGGTTTTGGTTAGGGAACGCCTCAG	This study
HJ071_NET1A_C-terminal_attb_fw	GGGGACAAGTTTGTACAAAAAAGCAGGCTTAGTGCCTTTCGACATGATTGA	This study
HJ072_NET1B_attB1_fw	GGGGACAAGTTTGTACAAAAAAGCAGGCTTAATGGCCAGTCTGTCGCAGTC	This study
HJ073_NET1B_attb2_rev	GGGGACCACTTTGTACAAGAAAGCTGGGTTCTACTCTTCTTTAGTCGAAG	This study
HJ074_NET1B_NAB_attb_rev	GGGGACCACTTTGTACAAGAAAGCTGGGTTCTGGTTAGGAAACGCCTCAA	This study
HJ075_NET1B_C-terminal_attb_fw	GGGGACAAGTTTGTACAAAAAAGCAGGCTTAATGTCTTTTGACATGATTGA	This study
HJ076_NET1C_CDS_attb_fw	GGGGACAAGTTTGTACAAAAAAGCAGGCTTAATGGAGATTGCAGCAAAGAG	This study
HJ077_NET1C_CDS_attb_rev	GGGGACCACTTTGTACAAGAAAGCTGGGTTTCAAGGAGACTCTGGCTGCT	This study
HJ078_NET1C_NAB_attb_rev	GGGGACCACTTTGTACAAGAAAGCTGGGTTTTGGTTTGGAAACGCTTCTG	This study
HJ079_NET1C_C-terminal_attb_fw	GGGGACAAGTTTGTACAAAAAAGCAGGCTTAGTTCCTTTGATATTTGGTGA	This study
HJ080_NET1D_CDS_attb_fw	GGGGACAAGTTTGTACAAAAAAGCAGGCTTAATGACTGCTGTTGTGAATGG	This study
HJ081_NET1D_CDS_attb_rev	GGGGACCACTTTGTACAAGAAAGCTGGGTTTCAAGGAGATGGAGGCGGTT	This study
HJ082_NET1D_NAB_attb_rev	GGGGACCACTTTGTACAAGAAAGCTGGGTTTTGGTTTGGGAAGGCTTCAG	This study
HJ083_NET1D_C-terminal_attb_fw	GGGGACAAGTTTGTACAAAAAAGCAGGCTTAGACCCTATGATGTTTGGTGA	This study
HJ084_STI_S1_attb_rev	GGGGACCACTTTGTACAAGAAAGCTGGGTTTTGGCTGAAGCTTCGGATTG	This study
HJ085_STI_S2_attb_fw	GGGGACAAGTTTGTACAAAAAAGCAGGCTTAAAGTACAGACCAATGTTTTT	This study
HJ086_STI_S2_attb_rev	GGGGACCACTTTGTACAAGAAAGCTGGGTTAAGCTGAAGCAAAGTCGCTG	This study
HJ087_STI_S3_attb_fw	GGGGACAAGTTTGTACAAAAAAGCAGGCTTAGGGTCAATGCCTTCTCCTGG	This study
HJ090_n-tag STI_fw	TGAGAGAGGAGAAGGAAGAAATC	This study

Oligo nucleotide	Sequence 5' to 3'	Provided by
HJ091_n-tag STI_rev	CCTCAAATCCTCTGAATTACTCA	This study
HJ092_c-tag STI_rev	GATGATATATATAGAAAATAAATTAC	This study
HJ093_c-tag STI_rev	TTAAAATATACTCCACTAAATTTTTGGA	This study
HJ094_c-tag STI_rev	TTGTTCATCAACTAAAATACCGA	This study
HJ095_c-tag STI_rev	GTAGCAATGCCGAAGGAAAGAAG	This study
HJ096_tdTomato_fw	ACGAGCGCTCCGAGGGCCGCCACC	This study
HJ097_tdTomato_rev	TCTGGGTGCCCTCGTAGGGGCGG	This study
HJ098_c-tag STI_fw	TCAACATTATTCCTATAATAAAGATA	This study
HJ099_c-tag STI_fw	TTCAGCCTAAACTTGGATTATGGAT	This study
HJ100_MpSTI_S2_fw	GGGGACAAGTTTGTACAAAAAAGCAGGCTTAAAATACCGACCCAGATCATT	This study
HJ101_MpSTI_S2_rev	GGGGACCACTTTGTACAAGAAAGCTGGGTTAAATTGCAGAAGAGCGGCAG	This study
HJ102_MpSTI_ATPase_updated_rev	GGGGACCACTTTGTACAAGAAAGCTGGGTTGGCCAGCGTTATCTGCAGTT	This study
HJ103_NET1Aseq_fw	GAACTAAATGATTCTTCTATGATC	This study
HJ115_MpSTI_S2_wQwSTOP_attb1	GGGGACAAGTTTGTACAAAAAAGCAGGCTTAATGAAATACCGACCCAGATC	This study
HJ116_PAM1_FW	ATTG AATGTCAGGTTCGAGAGTTT	This study
HJ117_PAM1_REV	AAAC AAACTCTCGAACCTGACATT	This study
HJ118_PAM2_FW	ATTG TTAATGGATGTGCTAAGCCA	This study
HJ119_PAM2_REV	AAAC TGGCTTAGCACATCCATTAA	This study
HJ120_STIseq	GTAAAACCCGAAAGGAATCAG	This study
HJ121_STIseq	CTAAGGCGAAGCGTAGAGGT	This study
HJ122_STIseq	ATTCTCGTTGCTTATATCGC	This study
HJ123_STI_attb2_woSTOP_rev	GGGGACCACTTTGTACAAGAAAGCTGGGTTTCTTCTAATGTTACCTTCTG	This study
HJ115_MpSTI_S2_wQwSTOP_attb1	GGGGACAAGTTTGTACAAAAAAGCAGGCTTAATGAAATACCGACCCAGATC	This study
HJ116_PAM1_FW	ATTG AATGTCAGGTTCGAGAGTTT	This study
HJ117_PAM1_REV	AAAC AAACTCTCGAACCTGACATT	This study
HJ118_PAM2_FW	ATTG TTAATGGATGTGCTAAGCCA	This study
HJ119_PAM2_REV	AAAC TGGCTTAGCACATCCATTAA	This study
HJ120_STIseq	GTAAAACCCGAAAGGAATCAG	This study
HJ121_STIseq	CTAAGGCGAAGCGTAGAGGT	This study
HJ122_STIseq	ATTCTCGTTGCTTATATCGC	This study
HJ123_STI_attb2_woSTOP_rev	GGGGACCACTTTGTACAAGAAAGCTGGGTTTCTTCTAATGTTACCTTCTG	This study
HJ128_SDM_STIwoSTOP_fw	GTAACATTAGAAGAAACCCAGCTTTCTTGTAC	This study
HJ129_SDM_STIwoSTOP_rev	GCTGGGTTTCTTCTAATGTTACCTTCTGCTTTCC	This study
HJ158_NET1D_seq_rev	ACTCTTCCTTTAAGCTGCTCAATCTC	This study

Oligo nucleotide	Sequence 5' to 3'	Provided by
HJ159_NET1D_seq_rev	TCTCCGACAGAAGCAAAGAGAT	This study
HJ160_NET1D_seq_rev	AATCTGCACTTGTTTCCCAATAT	This study
HJ161_STI_seq_fw	ATCAGGATCAGGAAGAGTTGGTTGT	This study
HJ158_NET1D_seq_rev	ACTCTTCCTTTAAGCTGCTCAATCTC	This study
HJ159_NET1D_seq_rev	TCTCCGACAGAAGCAAAGAGAT	This study
HJ160_NET1D_seq_rev	AATCTGCACTTGTTTCCCAATAT	This study
HJ161_STI_seq_fw	ATCAGGATCAGGAAGAGTTGGTTGT	This study
HJ174_STI_KO_N-terminal_fw	ATTG ATCGAGAGGAGATTTCCAGG	This study
HJ175_STI_KO_N-terminal_rev	AAAC CCTGGAAATCTCCTCTCGAT	This study
HJ176_NOEK_KO_N-terminal_fw	ATTG ATGTCAGAGACCGGGAAAAG	This study
HJ177_NOEK_KO_N-terminal_rev	AAAC CTTTTCCCGGTCTCTGACAT	This study
HJ178_STI_KO_C-terminal_fw	ATTG AGGGAACTCCTGTTCGTTCG	This study
HJ179_STI_KO_C-terminal_rev	AAAC CGAACGAACAGGAGTTCCCT	This study
HJ174_STI_KO_N-terminal_fw	ATTG ATCGAGAGGAGATTTCCAGG	This study
HJ175_STI_KO_N-terminal_rev	AAAC CCTGGAAATCTCCTCTCGAT	This study
HJ176_NOEK_KO_N-terminal_fw	ATTG ATGTCAGAGACCGGGAAAAG	This study
HJ177_NOEK_KO_N-terminal_rev	AAAC CTTTTCCCGGTCTCTGACAT	This study
HJ178_STI_KO_C-terminal_fw	ATTG AGGGAACTCCTGTTCGTTCG	This study
HJ179_STI_KO_C-terminal_rev	AAAC CGAACGAACAGGAGTTCCCT	This study
HJ180_NET1A_cterm1_CDS_attb_rev	GGGGACCACTTTGTACAAGAAAGCTGGGTTTTTGGGATCCAAACCTGCAA	This study
HJ181_NET1A_cterm2_CDS_attb_fw	GGGGACAAGTTTGTACAAAAAAGCAGGCTTATTTGGATCCCAAATCCCTTG	This study
HJ182_NET1A_cterm2_CDS_attb_rev	GGGGACCACTTTGTACAAGAAAGCTGGGTTTCAGAATTCCGCTTCTCTAA	This study
HJ183_NET1A_cterm3_CDS_attb_fw	GGGGACAAGTTTGTACAAAAAAGCAGGCTTAAAGCGGAATT	This study
HJ184_NET1B_cterm1_CDS_attb_rev	GGGGACCACTTTGTACAAGAAAGCTGGGTTCCTCGAGCTTTTCTTTCATT	This study
HJ185_NET1B_cterm2_CDS_attb_fw	GGGGACAAGTTTGTACAAAAAAGCAGGCTTAAAGCTCGAGGAAGAAGTTGC	This study
HJ186_NET1B_cterm2_CDS_attb_rev	GGGGACCACTTTGTACAAGAAAGCTGGGTTCGTCTACATTAGAAACCTGA	This study
HJ187_NET1B_cterm3_CDS_attb_fw	GGGGACAAGTTTGTACAAAAAAGCAGGCTTAATGTAGACGAAATCTTGGAA	This study
HJ188_NET1C_cterm1_CDS_attb_rev	GGGGACCACTTTGTACAAGAAAGCTGGGTTTCAGCTTCCTGGAAATGCAA	This study
HJ249_NET1C_cterm2_attb1	GGGGACAAGTTTGTACAAAAAAGCAGGCTTAGAAGCTGAGACCGCGTTTCA	This study
HJ250_NET1C_cterm2_attb2	GGGGACCACTTTGTACAAGAAAGCTGGGTTCTTGCATGCTTCAGCAAGCT	This study
HJ192_NET1D_cterm1_CDS_attb_rev	GGGGACCACTTTGTACAAGAAAGCTGGGTTAGTAGACCATCCAGTTCAGA	This study
HJ193_NET1D_cterm2_CDS_attb_fw	GGGGACAAGTTTGTACAAAAAAGCAGGCTTAAAGATCTGGAGAAAGAACAT	This study
HJ194_NET1D_cterm2_CDS_attb_rev	GGGGACCACTTTGTACAAGAAAGCTGGGTTGTCTAGATCCTCGTTTAGTT	This study
HJ195_NET1D_cterm3_CDS_attb_fw	GGGGACAAGTTTGTACAAAAAAGCAGGCTTAGATC	This study

Oligo nucleotide	Sequence 5' to 3'	Provided by
HJ251_NET1C_cterm3_attb1	GGGGACAAGTTTGTACAAAAAAGCAGGCTTAGAAGCATGCAAGAACCTTGA	This study
HJ252_NET1C_cterm3_attb2	GGGGACCACTTTGTACAAGAAAGCTGGGTTTCAAGGAGACTCTGGCTGCT	This study
HJ235_NET1A_PAM_seq_fw	CAAGAAGCGGCCTGAGCTTA	This study
HJ235_NET1A_PAM_seq_rev	CTCCAAATTCTGATCAAACT	This study
HJ237_NET1B_PAM_seq_fw	AACCCGGATGAGTTCCAACAAGATG	This study
HJ238_NET1B_PAM_seq_rev	TTCTCCTCAGAAAACTTTAACTTAGCAAC	This study
HJ239_NET1C_PAM_seq_fw	TAACGGATCTATCCCTCATC	This study
HJ240_NET1C_PAM_seq_rev	AACACCAGAAATCTCAACTG	This study
HJ241_NET1D_PAM_seq_fw	GTGAGGAAGATGATCGCTAAGTCT	This study
HJ242_NET1D_PAM_seq_rev	TGATGATGAGATCCTTCTTAACC	This study
HJ243_NET1C_PAM_seq_fw	CAAGAAGCGGCCTGAGCTTA	This study
HJ244_NET1C_PAM_seq_fw	CTCCAAATTCTGATCAAACT	This study
HJ245_Cas9_detect_fw	AACCCGGATGAGTTCCAACAAGATG	This study
HJ246_Cas9_detect_rev	TTCTCCTCAGAAAACTTTAACTTAGCAAC	This study
HJ247_Cas9_detect_fw	TAACGGATCTATCCCTCATC	This study
HJ248_Cas9_detect_rev	AACACCAGAAATCTCAACTG	This study
L708	CTCCGAGGACAACAACATG	Dr. Lisa Stephan

3.1.4 Bacterial and yeast strains

Tab. 5: List of bacterial and yeast strains used in this study.

Organism	Strain	Property	Reference	Use
E. coli	DH5α	F-, ϕ80lacZ ΔM1, Δ(lacZYA-argF), U169, deoR, recA1, endA1, hsdR17, (rk-, mk+), phoA, supE44, thi-1, gyrA96, relA1, -λ	Hanahan, 1983	Amplification of plasmids that do not carry a ccdB operon
	DB3.1	F-gyrA462 endA1 glnV44 Δ(sr1-recA) mcrB mrr hsdS20(rB-, mB-) ara14 galK2 lacY1 proA2 rpsL20(Smr) xyl5 Δleu mtl1	Bernard & Couturier, 1992; T. Miki et al., 1992	Amplification of plasmids that do carry a ccdB operon
	BL21(DE3)	fhuA2 [lon] ompT gal (λ DE3) [dcm] ΔhsdS λ DE3 = λ sBamHIo ΔEcoRI-B int::(lacI::PlacUV5::T7 gene1) i21 Δnin5	Studier & Moffatt, 1986	Protein expression
A. tumefaciens	GV3101:pMP90RK and GV3101:pMP90	pTiC58ΔT-DNA	Koncz & Schell, 1986	Transformation of *Arabidopsis*
S. cerevisiae	AH109	MATa, trp1-901, leu2-3, 112, ura3-52, his3-200, gal4Δ, gal80Δ, LYS2: : GAL1UAS-GAL1TATAHIS3, MEL1 GAL2UAS-GAL2TATA-ADE2, URA3::MEL1UAS-MEL1TATA-lacZ	Fields & Song, 1989	Yeast Two-Hybrid interaction studies

3.1.5 Wild type and mutant plants

Tab. 6: List of wild type and mutant plants used in this study.

Line	Ecotype	Target ID	Reference/Source
Col-0		Col-0	
sti146	Ler	AT2G02480	Illgenfritz et al. 2003

3.1.6 Stably transformed *A. thaliana* lines

The constructs used to generate stable lines are listed in table 7 together with the respective provider.

Tab. 7: List of stabily transformed *A. thaliana lines* used in this study.

Construct	Background	Source/Reference
DD45	Col-0	Mao et al., 2016
HY115	Col-0	This study
HY116	Col-0	This study
HY117	Col-0	This study
HY102	Col-0	This study
HY0100	DD45	Mao et al., 2016/this study

3.1.7 Solutions and media

Tab. 8: List of antibiotics used in this study.

Antibiotics	Stock [mg/mL]	Stored in	Conc. *E. coli* [µg/mL]	Conc. *A. tumefaciens* [µg/mL]
Carbenicillin	50	H_2O	50	50
Gentamycin	25	H_2O	25	-
Hygromycin	25	H_2O	25	25
Kanamycin	50	H_2O	50	50
Rifampicin	50	MeOH	-	25-150
Spectomycin	50	H_2O	50	50

LB Medium

Lysogeny-Broth (LB) medium was prepared by dissolving 20 g yeast extract, 40 g Bacto-peptone, and 40 g sodium chloride in distilled water to a final volume of 4 L. The pH was adjusted to 7.0 using sodium hydroxide if required. For solid medium, 6.4 g agar was added to 400 mL of liquid LB. The medium was sterilized by autoclaving for 20 minutes.

YEB Medium

Yeast extract-beef (YEB) medium was prepared by combining 20 g beef extract, 4 g yeast extract, 20 g sucrose and 20 g peptone in distilled water, followed by the addition of 8 mL of 1 M magnesium sulphate heptahydrate solution. The final volume was adjusted to 4 L. For plate preparation, 6.4 g agar was added per 400 mL medium. Sterilization was performed by autoclaving for 20 minutes.

MS Medium

Murashige and Skoog (MS) medium was prepared in two concentrations: Full-strength (1× MS): 40 g sucrose and 17.6 g MS basal salts were dissolved in water to a final volume of 4 L. Half-strength (½× MS): 20 g sucrose and 8.8 g MS basal salts were dissolved and adjusted to 4 L. The pH of both media was set to 5.8 using 2 M potassium hydroxide. For solidification, 3.2 g plant agar was added to 400 mL medium. All MS media were autoclaved for 20 minutes.

YPAD Medium

YPAD medium was prepared by dissolving 8 g peptone, 4 g yeast extract, and 40 mg adenine in 380 mL distilled water. The pH was adjusted to 5.8 using concentrated hydrochloric acid. After autoclaving (20 minutes), the medium was cooled to approximately 55 °C, and 20 mL of sterile 40% glucose solution was added aseptically.

SD-LW Medium

Synthetic defined medium lacking leucine and tryptophan (SD-LW) was prepared by dissolving 0.68 g yeast nitrogen base, 2 g ammonium sulphate, 0.24 g dropout supplement (without leucine, tryptophan and histidine), 8 mg histidine, and 40 mg adenine in 380 mL distilled water. Agar (7.2 g per 400 mL bottle) was added prior to sterilization. The pH was adjusted to 5.8 using 1 M sodium hydroxide. The medium was autoclaved for 12 minutes and cooled to 55 °C before use.

TB Medium

Terrific Broth (TB) medium was prepared by dissolving 12 g tryptone, 24 g yeast extract, and 4 mL glycerol in distilled water to a final volume of 900 mL. The solution was autoclaved at 121 °C. After cooling, 100 mL of sterile 1 M phosphate buffer (prepared from 1 M KH_2PO_4 and 1 M K_2HPO_4 mixed to pH 7.5) was added under sterile conditions. The buffer solution was sterilized separately by filtration prior to addition.

3.1.8 Solutions & buffers

50× TAE buffer

A 50× TAE stock solution was prepared by dissolving 242 g Tris base in distilled water, followed by the addition of 57.1 mL glacial acetic acid and 100 mL of 500 mM EDTA (pH 8.0). The final volume was adjusted to 1 L with distilled water.

HEPES buffer

A 1 L stock solution of HEPES buffer was prepared by dissolving 11.92 g HEPES and 24.22 g NaCl in distilled water. The pH was adjusted to 8.0 using NaOH or HCl, and the final volume was brought to 1 L with distilled water.

TBS buffer

A 1 L stock solution of TBS buffer was prepared by dissolving 6.06 g Tris base and 8.77 g NaCl in distilled water. The pH was adjusted to 7.4 using HCl, and the final volume was brought to 1 L with distilled water.

MBP purification / elution buffer

For MBP-tagged proteins, the HEPES buffer was supplemented with 10 mM maltose. Maltose concentrations in the elution buffer spanned the range of 10-30 mM for optimization of protein elution.

10× DNA loading dye

The DNA loading dye (10×) was prepared by combining 6.25 mL of 80% (w/v) glycerol, 1 mL of 0.5 M EDTA (pH 8.0), 10 mg xylene cyanole, 25-50 mg Orange G, and 100 µL of 1 M Tris-HCl (pH 8.0). The mixture was brought to a final volume of 10 mL with distilled water.

Protein loading dye

The protein loading dye (2 x) was prepared combining 50 mM Tris / HCl pH 6.8, 2 % SDS, 10% Glycerol, 0,1% Bromophenol Blue, 100 mM DTT to a final volume of 50 mL with distilled water.

Agromix

A 10× Agromix stock solution was prepared by dissolving 2.03 g $MgCl_2 \cdot 6H_2O$ and 1.95 g MES in distilled water to a final volume of 100 mL. The pH was adjusted to 5.6 using 1 M NaOH. For preparation of 1× Agromix, 0.9 mL of the 10× stock solution was mixed with 0.1 mL acetosyringone (3 mg/mL in 100% ethanol) and 9 mL distilled water immediately prior to tobacco infiltration.

$CaCl_2$ solution for competent *E. coli*

A solution containing 60 mM $CaCl_2$ and 10 mM PIPES buffer was prepared and adjusted to pH 7.0 using NaOH. Glycerol was added to a final concentration of 15 % (v/v). The solution was sterilized by autoclaving for 15 minutes.

Colloidal Coomassie staining solution

The Coomassie staining solution was prepared by dissolving 80 mg Coomassie Brilliant Blue G-250 in distilled water, followed by the addition of hydrochloric acid to a final concentration of 35 mM. The solution was adjusted to a final volume of 1 L with distilled water and mixed thoroughly. Prior to first use, the staining solution was incubated overnight with gentle shaking to ensure complete dissolution of the dye.

Extraction buffer for genomic DNA isolation

For preparation of 50 mL extraction buffer, 10 mL of 1 M Tris-HCl (pH 8.0), 2.5 mL of 5 M NaCl, 2.5 mL of 0.5 M EDTA (pH 8.0), and 2.5 mL of 10% SDS were combined and filled up to 50 mL with distilled water.

10× running buffer for SDS-PAGE

A 10× running buffer was prepared by dissolving 30.3 g Tris base and 188.0 g glycine in approximately 900 mL distilled water. After complete dissolution, 100 mL of a 10% (w/v) SDS solution was added to achieve a final SDS concentration of 1%. The solution was mixed thoroughly and adjusted to a final volume of 1 L with distilled water.

Magic buffer for genomic DNA isolation

To prepare 100 mL of Magic buffer, 5 mL of 1 M Tris-HCl (pH 7.2), 6 mL of 5 M NaCl, and 10 g sucrose were dissolved in distilled water. The final volume was adjusted to 100 mL.

3.2 Molecular methods

3.2.1 Genomic DNA extraction from plant tissue

A piece of plant tissue (< 1 cm) was transferred into a 1.5 mL SafeSeal Eppendorf tube containing 3-4 glass beads. Subsequently, 300 µL of Magic buffer for genomic DNA isolation was added, and the sample was homogenized using a TissueLyser (Qiagen) at 30 Hz for 1.5 minutes. The resulting extract was used directly for PCR-based amplification of genomic DNA from *Arabidopsis* samples and was stored at -20 °C only for short-term use.

3.2.2 PCR

DNA amplification was carried out using polymerase chain reaction (PCR). Different DNA polymerases were selected depending on the intended downstream application and the characteristics of the target fragment.

Phusion polymerase PCR

Owing to its high fidelity and low error rate, Phusion™ High-Fidelity DNA polymerase (Thermo Fisher Scientific) was employed for amplification of DNA fragments intended for cloning and sequencing. The PCR reactions were performed using the reaction mixture and cycling program described below.

Tab. 9: Phusion polymerase PCR reaction mixture and cycling program used in this study.

Component	**Volume**	**PCR Program**		
Template DNA	1 µL	98 °C	60 s	
Forward primer (10 µM)	0.5 µL	98 °C	10 s	35 cycles
Reverse primer (10 µM)	0.5 µL	TA	30 s	
dNTP mix (10 mM each)	0.5 µL	72 °C	15-30 s/kb	
5× High-Fidelity buffer	5 µL	72 °C	10 min	
Phusion DNA polymerase (2 U/ µL)	0.3 µL	8 °C	∞	
ddH_2O	17.2 µL			

PCR-mediated site-directed mutagenesis

Single or multiple base pair changes (1-3 bp) within a DNA sequence were introduced using primers containing the desired mutation in a PCR-based approach. Primers were designed according to the following guidelines: the 5′ end of the primer could be positioned as close as 4 bp from the mutation site, while the 3′ end was placed at least 8 bp away; each primer included at least 8 non-overlapping nucleotides at the 3′ end, contained at least one G or C at each terminus, and had a melting temperature (T_m) ≥ 78 °C. PCR amplification of the entire plasmid was carried out using Phusion™ DNA polymerase with the reaction mixture and cycling program described previously. To eliminate the parental template, 1 µL of DpnI was added to 50 µL of PCR product and incubated at 37 °C for 2 hours. The enzyme was subsequently inactivated by heating at 80 °C for 20 minutes, and 1 µL of the treated PCR mix was used for transformation.

PCR for AT-rich sequences

PCR amplification of AT-rich DNA regions can be difficult due to sequence composition. To improve amplification efficiency, reactions targeting AT-rich sequences were carried out using Phusion™ DNA polymerase with the reaction mixture and cycling conditions described below.

Tab. 10: Polymerase PCR for AT-rich sequences; reaction mixture and cycling program used in this study.

Component	**Volume**
Template DNA	2 µL
Forward primer (10 µM)	0.8 µL
Reverse primer (10 µM)	0.8 µL
dNTP mix (10 mM each)	0.4 µL
5× High-Fidelity buffer	4 µL
Phusion DNA polymerase (2 U/ µL)	0.2 µL
$MgCl_2$ [50 mM]	1.2 µL
ddH_2O	10.6 µL

PCR Program		
98 °C	90 s	
98 °C	30 s	35 cycles
Gradient (TA+5 °C to 72°C)	3 min	
Gradient (TA+5 °C to 72°C)	7 min	
12 °C	∞	

GreenTaq polymerase PCR

GreenTaq DNA polymerase was used for routine PCR amplifications where standard fidelity was sufficient, such as analytical or screening reactions. The premixed GreenTaq master mix offers several advantages, including reduced pipetting steps, minimized risk of contamination, consistent reagent concentrations, and the inclusion of loading dye for direct gel loading, which streamlines PCR setup and downstream analysis. The reactions were performed according to the composition and cycling program detailed below.

Tab. 11: GreenTaq polymerase PCR reaction mixture and cycling program used in this study.

Component	Volume	PCR Program		
Template DNA	1 µL	95 °C	2 min	
Forward primer (10 µM)	0.5 µL	95 °C	30 s	30-40 cycles
Reverse primer (10 µM)	0.5 µL	TA	30 s	
GreenTaq Ready-to-Use Master Mix (2×)	10 µL	72 °C	30-60 s / kb	
5× GreenTaq reaction buffer	5 µL	72 °C	10 min	
ddH_2O	8 µL	8 °C	∞	

Colony PCR

Colony PCR was performed to screen bacterial transformants for the presence of the desired insert. Individual colonies were picked using a sterile pipette tip and resuspended in ddH_2O. 1 µL of this suspension was used directly as template for PCR. The reactions were performed according to the composition and cycling program detailed below. PCR products were analyzed by agarose gel electrophoresis to verify the presence and size of the expected fragments. Colonies showing the correct band pattern were sent for sequencing.

Tab. 12: Colony PCR reaction mixture and cycling program used in this study.

Component	Volume
Culture solution	1 µL
Forward primer (10 µM)	0.8 µL
Reverse primer (10 µM)	0.8 µL
dNTPs (10 mM)	0.4 µL
2× DreamTaq buffer	2 µL
DreamTaq	0.1 µL
ddH_2O	14.9 µL

PCR Program		
95 °C	5 min	
95 °C	30 s	30 cycles
TA	30 s	
72 °C	30-60 s / kb	
72 °C	10 min	
8 °C	∞	

3.2.3 Gel electrophoresis

Gel electrophoresis was used to separate and visualize DNA fragments following PCR amplification or restriction digestion. Standard agarose gels (1%) were prepared using 1× TAE buffer, obtained by diluting 50 × stock solution with distilled water. DNA was visualized by incorporating ethidium bromide (0.25 µg/mL) directly into the gel. Gels were placed in an electrophoresis chamber filled with 1× TAE buffer, and DNA samples were combined with 10× loading dye prior to loading, if needed. Electrophoresis was performed at 120-150 V. DNA size markers, GeneRuler 1 kb (Thermo Fisher Scientific) and GeneRuler 1 kb Plus (Thermo Fisher Scientific), were used as references. Gels containing ethidium bromide were imaged using either a Bio-Rad Universal Hood II with Quantity One software (v4.5.0) or an INTAS Gel Jet Imager (GDS Touch 2, v2.1.4).

3.2.4. DNA gel extraction

PCR products or restriction-digested plasmid fragments were isolated by excising the corresponding DNA band from an agarose gel. DNA was purified using the GeneJET Gel Extraction Kit (Thermo Fisher Scientific) following the manufacturer's instructions.

3.2.5 DNA plasmid preparation

Plasmid DNA was obtained from overnight bacterial cultures. Single colonies were grown in 5 mL of selective medium at 37 °C or 28 °C with shaking at 220 rpm. Cells were harvested by

centrifugation at 8,000 rpm for 2 minutes, and plasmid DNA was purified using the GeneJET Plasmid Miniprep Kit (Thermo Fisher Scientific) according to the manufacturer's instructions.

3.2.6 Restriction digest

Cloning verification and assessment of vector integrity were performed using restriction enzyme digestions. All enzymes were obtained from Thermo Fisher Scientific. For standard digestions, reaction mixtures contained 2 µL plasmid DNA, 2 µL of the corresponding enzyme buffer, 0.3 µL restriction enzyme, and 15.7 µL distilled water. Reactions were incubated at 37 °C for 1 hour. For FastDigest enzymes, 2 µL plasmid DNA was combined with 2 µL FastDigest buffer, 1 µL FastDigest enzyme, and 15 µL water. Double digests were carried out following the manufacturer's instructions.

3.2.7 Linearization of vectors

Linearization of plasmid vectors was performed to improve cloning efficiency. For a 20 µL reaction, 2-5 µL of plasmid DNA was combined with 2 µL of the appropriate enzyme buffer, 0.5 µL restriction enzyme, and 1 µL FastAP phosphatase (Thermo Fisher Scientific). The mixture was incubated overnight at 37 °C. The following morning, an additional 1 µL of enzyme was added, and digestion was continued for 2-3 hours. The reaction was subsequently heat-inactivated at 80 °C for 20 minutes.

3.2.8 Cloning

Gateway cloning

Most vectors used in this study were compatible with the Gateway cloning system, which employs a recombination mechanism derived from bacteriophage λ (Invitrogen). In this system, the DNA fragment of interest is first amplified by PCR with flanking recombination sites. The amplified fragment is then integrated into an entry vector via a BP recombination reaction, in which recombination occurs between attB and attP sites to generate attL-flanked entry clones. The resulting entry vector can subsequently be used in an LR recombination reaction, where recombination between attL and attR sites transfers the insert into a destination vector to generate the final expression construct. The terms BP and LR originate from the corresponding bacteriophage λ recombination reactions: BP refers to recombination between attB and attP

sites, whereas LR describes recombination between attL and attR sites. The reaction mixtures for BP and LR recombination are summarized in Tab. 13.

Tab. 13: BP and LR recombination mixture used in this study.

Component	BP Reaction (µL)	LR Reaction (µL)
Enzyme mix	0.5	0.5
Donor / Entry vector	0.25	0.5
PCR product / Insert	1.75	-
Destination vector	-	0.25
Water	1.25	1.25

Partial restriction digest

A partial restriction digest was performed to generate a series of DNA fragments with varying degrees of digestion. A master mix containing plasmid DNA and the appropriate restriction buffer was prepared and distributed into five separate reaction tubes with decreasing reaction volumes. Restriction enzyme was added only to the first tube at a concentration corresponding to approximately 3-10 U per µg DNA. To create a gradient of enzyme concentration, a serial dilution approach was applied: 10 µl of the reaction mixture from the first tube was transferred to the second tube and mixed thoroughly. This step was repeated sequentially from tube two to tube five, resulting in progressively lower enzyme concentrations across the series. All reactions were incubated for 15 minutes under conditions appropriate for the restriction enzyme used. The reactions were subsequently heat-inactivated at 80 °C for 20 minutes to terminate enzymatic activity. Aliquots of each reaction were analysed by agarose gel electrophoresis to assess the extent of DNA digestion and to identify conditions yielding partial digestion patterns.

Ligation

DNA fragments containing compatible restriction sites were ligated into linearized vectors using T4 DNA ligase (Thermo Fisher Scientific). For each reaction, 50 ng of vector DNA was combined with the insert at a molar ratio ranging from 1:1 to 1:10, with 1:5 being most commonly applied. The appropriate amount of insert was determined using the NEB Ligation Calculator (New England Biolabs, 2026; https://nebiocalculator.neb.com/#!/ligation). Ligation reactions were assembled according to the manufacturer's protocol, with adjustments depending on whether sticky- or blunt-ended fragments were used. Reactions were incubated

at room temperature for 30 minutes to overnight. Subsequently, 5 µL of the ligation mixture was used to transform 50 µL of competent *E. coli* cells (DB3.1 or DH5α).

Site-directed mutagenesis of vector LS658

In addition to restriction enzyme-based cloning, the donor vector LS658 was modified by PCR-mediated site-directed mutagenesis. This step was required to remove a pre-existing stop codon from the vector sequence. Mutagenic primers HJ128 and HJ129 were designed to introduce the desired sequence change during PCR amplification of the plasmid.

3.2.9 Guide RNA design and protospacer cloning for CRISPR/Cas9-mediated genome editing

Guide RNA target sequences were designed using the CHOPCHOP web tool (https://chopchop.cbu.uib.no; Labun et al., 2019). Target sites were selected based on predicted efficiency and off-target scores. CHOPCHOP outputs include the protospacer sequence followed by the PAM motif (NGG). For cloning purposes, only the 20 bp protospacer sequence was used, excluding the PAM sequence.

Complementary oligonucleotides encoding the protospacer sequences were synthesized with appropriate BbsI-compatible overhangs. Typically, a 5′ ATTG overhang was added to the forward oligonucleotide and a corresponding 5′ AAAC overhang to the reverse oligonucleotide to enable directional cloning into the vector. Oligonucleotides were annealed by incubation at 95 °C for 5 minutes, followed by gradual cooling to room temperature for 20 minutes. The annealed oligonucleotides were ligated into a BbsI-digested CRISPR/Cas9 donor vector (see below) using standard cloning procedures.

3.2.10 Cloning strategy for CRISPR/Cas9 constructs

CRISPR/Cas9 constructs for *A. thaliana* were generated using a modular cloning strategy that combined protospacer insertion, vector backbone modification, and, where required, integration of repair templates for knock-in applications.

Insertion of protospacer sequences

Protospacer sequences were introduced into different vector systems using type IIS restriction enzyme cloning. Single-stranded oligonucleotides encoding the target-specific protospacers were annealed to form double-stranded DNA fragments with compatible overhangs.

The Gateway-compatible donor vector pEN-Chimera was used for subsequent recombination-based cloning. Protospacer sequences were inserted via BbsI-mediated digestion and ligation (Thermo Fisher), generating directional overhangs for efficient incorporation of annealed oligonucleotides.

In addition, non-Gateway CRISPR/Cas9 expression vectors pEC1.2_EC1.1 spCas9_GFP (HY112), pEC1.2_pEC1.1 spCas9 TagRFP (HY114), and pEC1.2_pEC1.1 Cas9i TagRFP (HY120) were used. In these vectors, protospacer sequences were introduced analogously using BsaI-mediated cloning (Thermo Fisher). Successful insertion of protospacers was verified by colony PCR and agarose gel electrophoresis.

The vector HY112 was used for CRISPR/Cas9-mediated knockout experiments and directly employed for plant transformation via floral dipping.

Modification of the pDe-Cas9 backbone

For knock-in applications, the pDe-Cas9 vector was modified to generate a suitable backbone for targeted sequence insertion. This involved a series of restriction digests and re-ligation steps.

A partial digestion with EcoRI (Thermo Fisher) was performed to remove the Cas9 promoter. Due to the presence of multiple EcoRI sites within the vector backbone, a partial digest was required. The resulting construct was re-ligated and subsequently digested with AsCI (Thermo Fisher) to remove the Cas9 coding sequence, followed by another re-ligation. The BASTA resistance cassette was removed by HindIII digestion (Thermo Fisher) and re-ligation. Subsequently, the Cas9 terminator was excised using SacI (Thermo Fisher), resulting in a minimized backbone. To introduce an alternative selection system, a cassette encoding *OLEOSIN* (*OLE1*) for fluorescent seed selection was excised from the pFAST-R06 vector using HindIII (Thermo Fisher) and ligated into the modified pDe-Cas9 backbone.

Assembly of final knock-in constructs

For pDe-Cas9-derived knock-in constructs, protospacer sequences cloned into pEN-Chimera were transferred into the modified pDe-Cas9 destination vector by Gateway LR recombination. Repair fragments containing the desired homologous sequences and the fluorophore were designed with flanking AsCI restriction sites, synthesized by Genewiz, and delivered in a pUC vector. To avoid repeated Cas9-mediated cleavage after successful HDR integration, synonymous (silent) mutations were introduced into the sgRNA target region of the donor construct without altering the encoded amino acid sequence. Following excision by AsCI digestion (Thermo Fisher), these fragments were ligated into the corresponding AsCI-linearized pDe-Cas9-derived vectors.

For knock-in constructs based on HY114 and HY120, repair fragments were introduced via restriction site mediated ligation. After insertion of the respective protospacer sequences, the vectors were digested with SpeI and MfeI (Thermo Fisher). Repair fragments containing the desired homologous sequences and the fluorophore carrying compatible SpeI and MfeI restriction sites were synthesized by Genewiz and delivered in a pUC vector. These fragments were excised by double digestion with SpeI and MfeI and ligated into the correspondingly linearized vectors.

Thus, different construct series were generated depending on the experimental purpose: HY112-based vectors for knockout experiments, and HY114-, or HY120-derived vectors for knock-in applications.

An overview of the vectors used, the corresponding protospacer oligonucleotides, the cloning strategy, and the final construct purpose is provided in Tab. 14.

Tab. 14: Overview of the vectors, corresponding protospacer oligonucleotides, cloning strategy, and the final construct purpose used in this study.

Construct ID	Backbone	Cloning strategy	Protospacer ID	Repair template	Tag / insertion	Application
HY098	HY011	pEN-Chimera (BbsI) + LR + AsCI	HJ116 + HJ117	HDR template STI N-term	tdTomato (N-terminal)	Knock-in
HY100	HY011	pEN-Chimera (BbsI) + LR + AsCI	HJ118 + HJ119	HDR template STI C-term	tdTomato (C-terminal)	Knock-in
HY115	HY112	BsaI	HJ174 + HJ175	-	-	Knockout (STI N-term)
HY116	HY112	BsaI	HJ176 + HJ177	-	-	Knockout (NOEK)
HY117	HY112	BsaI	HJ178 + HJ179	-	-	Knockout (STI C-term)
HY198	HY114	BsaI + SpeI/MfeI	HJ116 + HJ117	HDR template STI N-term	mNeonGreen (N-terminal)	Knock-in
HY199	HY114	BsaI + SpeI/MfeI	HJ118 + HJ119	HDR template STI C-term	mNeonGreen (C-terminal)	Knock-in
HY201	HY120	BsaI + SpeI/MfeI	HJ118 + HJ119	HDR template STI C-term	mNeonGreen (C-terminal)	Knock-in

3.2.11 Generation of heat-shock competent bacteria

Competent *Escherichia coli*

To prepare heat-shock competent *E. coli*, a 5 mL pre-culture in LB medium without antibiotics was inoculated with 50 µl of competent cells and incubated overnight at 37 °C with shaking at 220 rpm. The following day, 200 mL of LB medium was inoculated with 2 mL of the pre-culture and grown at 37 °C with shaking at 200 rpm. After approximately 2 hours, the optical density at 600 nm (OD_{600}) was measured, and the culture was used for further processing only if the OD did not exceed 0.4. The culture was then split into four 50 mL aliquots, pelleted by centrifugation at 1600 g for 7 minutes at 4 °C, and the supernatant discarded. The pellets were resuspended in 10 mL of ice-cold 0 M $CaCl_2$ solution. Following a second centrifugation at 1100 g for 5 minutes at 4 °C, the pellets were resuspended again in 10 mL ice-cold $CaCl_2$ and incubated on ice for 30 minutes. After a final centrifugation, the cells were combined and resuspended in 2 mL $CaCl_2$. Aliquots were prepared, frozen in liquid nitrogen, and stored at -70 to -80 °C until use.

Competent *Agrobacterium tumefaciens*

For preparation of heat-shock competent *A. tumefaciens*, a 5 mL pre-culture in YEB medium containing the appropriate antibiotics was inoculated with 50 µl of competent cells and incubated overnight at 28 °C with shaking at 220 rpm. The next day, 200 mL YEB medium with antibiotics was inoculated with 2 mL pre-culture and grown at 28 °C and 220 rpm. Growth was monitored until OD_{600} reached 0.5-0.6. The culture was divided into four aliquots and centrifuged at 4000 rpm for 10 minutes at 4 °C. Each pellet was resuspended in 5 mL ice-cold 0.15 M NaCl; pairs of pellets were pooled afterwards. After 15 minutes on ice, the cells were centrifuged again and finally resuspended in 15 mL ice-cold 20 mM $CaCl_2$. Aliquots were frozen in liquid nitrogen and stored at -70 to -80 °C.

3.2.12 Transformation of heat-shock competent bacteria

E. coli transformation

For plasmid introduction into *E. coli*, 50 µl of competent cells were incubated on ice and mixed with 0.5 µl of plasmid DNA or the total BP/LR reaction volume. The cells were incubated on ice for 30 minutes, followed by a heat shock at 42 °C for 2 minutes. Immediately afterward, the

cells were returned to ice for 2 minutes. Subsequently, 300 µl of LB medium without antibiotics was added, and cells were allowed to recover at 37 °C with shaking at 600 rpm for 1 hour. The cells were then pelleted, resuspended in the remaining medium, and plated on LB agar containing the appropriate antibiotic. Plates were incubated overnight at 37 °C to allow colony formation.

A. tumefaciens transformation

Competent *A. tumefaciens* cells (50 µl) were incubated on ice and with 2 µl plasmid DNA for 30 minutes. Cells were heat-shocked at 42 °C for 2 minutes and immediately placed on ice for 2 minutes. Afterward, 700 µl of YEB medium without antibiotics was added, and cells were incubated at 28 °C with shaking at 650 rpm for 1.5 hours to recover. Subsequently, 100 µl of the culture was plated on selective YEB agar and incubated at 28 °C for 3-4 days until colonies appeared.

3.2.13 Preparation of glycerol stocks

Single colonies of *E. coli* or *A. tumefaciens* were used to inoculate 5 mL of selective LB or YEB medium, respectively. After overnight incubation at 37 °C (*E. coli*) or 28 °C (*A. tumefaciens*) with shaking at 220 rpm, 800 µl of culture was mixed with 400 µl of 60 % sterile glycerol. The suspension was vortexed briefly, frozen in liquid nitrogen, and stored at -70 °C for long-term preservation.

3.2.14 Yeast two-hybrid (Y2H) assays

Yeast transformation

Yeast transformation for yeast two-hybrid assays was performed using a lithium acetate/polyethylene glycol (LiAc/PEG)-based protocol. A pre-culture was prepared by inoculating yeast cells into 10 mL YPAD medium and incubating overnight at 30 °C with shaking. The following day, 1 mL of the overnight culture was used to inoculate 50 mL YPAD medium and grown at 30 °C until an OD_{600} of 0.6-0.8 was reached.

Cells were harvested by centrifugation (5 min, 4000 rpm) and resuspended in 0.1 M lithium acetate (LiAc). After a second centrifugation step, the pellet was resuspended in transformation master mix. The master mix for one sample consisted of 240 µL 50% PEG 3350, 36 µL 1M LiAc, 10 µL ssDNA (10 mg/mL), boiled at 99 oC for 10 min, and 61 µL ddH_2O. For each

transformation, 2 µl of each plasmid (activation domain and binding domain constructs) were added to a microcentrifuge tube, followed by 350 µl of the yeast suspension. Samples were vortexed thoroughly and incubated at 42 °C for 40 minutes to facilitate DNA uptake. Cells were subsequently pelleted briefly, resuspended in 100 µl sterile water, and plated on selective SD medium lacking leucine and tryptophan (-LW). Plates were incubated at 30 °C for 3-4 days until transformant colonies appeared.

Drop assay

Protein-protein interactions were assessed using a serial dilution drop assay. Transformed yeast colonies were resuspended in sterile water, and serial dilutions were prepared in a 96-well plate by sequential transfer of cell suspensions. 100 µl of water was used for the initial suspension, followed by 1 : 10 and 1 : 100 dilution steps into wells containing 90 µl water. Dilutions were transferred onto selective SD plates lacking leucine and tryptophan (-LW) as well as higher stringency media lacking leucine, tryptophan, and histidine (-LWH), supplemented with increasing concentrations of 3-amino-1,2,4-triazole (3-AT). A sterile replica-plating stamp was used to transfer cells from the dilution plate onto agar plates. Plates were allowed to dry before incubation and subsequently grown at 30 °C for 7 days. Growth on selective media was used as an indicator of protein-protein interaction strength.

3.3 Protein biochemistry

3.3.1 Protein expression in *Escherichia coli*

Recombinant protein expression was performed in *Escherichia coli* Rosetta (RIL) cells. Overnight cultures (5 mL) were prepared in TB medium with the appropriate antibiotic at 37 °C with shaking. For main cultures, 1 mL of the overnight culture was used to inoculate 200 mL TB medium. Cultures were grown at 37 °C until an OD_{600} of 0.5-1.0 was reached.

Protein expression was induced by addition of IPTG to a final concentration of 0.5-1 mM. To optimize expression conditions, different induction parameters were tested, including temperature and incubation time. Cultures were incubated at 20 °C for 6 hours or at 16 °C overnight (approximately 16 hours). Inductions were performed at both lower and higher cell densities within the tested OD_{600} range.

Samples for SDS-PAGE analysis were collected at defined time points. Aliquots of the culture were pelleted by centrifugation (8000 rpm, 2 min, 4 °C), resuspended in 5 µl protein sample buffer, and denatured prior to analysis.

3.3.2 SDS-PAGE and Coomassie staining

Protein samples were separated by a 12% SDS-PAGE and visualized by Coomassie staining. Following electrophoresis, gels were briefly rinsed and heated in water to facilitate fixation. Subsequently, gels were incubated in Coomassie staining solution and heated until staining was achieved. Excess dye was removed by repeated washing steps in water, including heating cycles to accelerate destaining. If required, gels were incubated in staining solution overnight prior to destaining. Protein sizes were estimated using the PageRuler™ Plus Prestained Protein Ladder (Thermo Scientific) according to the manufacturer's instructions.

3.3.3 Protein purification and pulldown

All purification steps were carried out at 4 °C to maintain protein stability. Pellets obtained from 100 mL cultures were resuspended in 10 mL HEPES-based buffer (11.92 g HEPES, 24.22 g NaCl per L, pH adjusted to 8.0) supplemented with EDTA-free protease inhibitor cocktail (1 tablet per 50 mL buffer) and 100 µg/mL lysozyme. Samples were incubated on ice for 20-40 minutes to facilitate cell lysis.

Prior to protein binding, 100 µl amylose beads were equilibrated with 12 mL of HEPES buffer, followed by two centrifugation steps at 3000 g for 1 minute at 4 °C and removal of the supernatant. Cell lysates were sonicated twice for 1 minute at 60 % amplitude and cleared by centrifugation at 3220 rpm for 15 minutes. An aliquot of 50 µl of the supernatant was saved as the "lysate" fraction.

Cleared lysates were incubated with the equilibrated beads for 30 minutes under constant rotation. After incubation, beads were washed three times with 15 mL HEPES buffer, and 50 µl of the final wash was retained as "wash 3". Proteins were eluted using elution buffer containing HEPES pH 8.0 supplemented with 10 to 30 mM maltose. Elution was performed in a 1:1 ratio of buffer to bead volume, with two incubations of 15 minutes on ice, followed by centrifugation at 500 g for 3 minutes. The resulting supernatants were collected as "elution fractions 1-3." Beads were subsequently mixed with 50 µl of 2× protein loading dye, boiled at

95 °C for 5 minutes, and saved as the “bead fraction.” All fractions, as well as the remaining beads, were stored at -20 °C until further analysis.

3.3.4 Protein solubility assay

Protein solubility was assessed by separating soluble and insoluble protein fractions following cell lysis. For this purpose, 10 mL of induced bacterial cultures were collected and pelleted by centrifugation (4000 rpm, 5 min, 4 °C). Cell pellets were resuspended in 2 mL Tris-HCl buffer (50 mM, pH 7.5). Cells were disrupted by sonication using a sonotrode (1 min at 60% amplitude), followed by a short cooling period, with all steps performed on ice to prevent protein degradation. The lysates were subsequently centrifuged (8000 rpm, 2 min, 4 °C) to separate soluble and insoluble fractions. The supernatant (soluble fraction) was mixed 1:1 with protein sample buffer. The pellet (insoluble fraction) was resuspended in distilled water and mixed with protein sample buffer to obtain comparable sample volumes. Both fractions were boiled for 5 minutes at 95-98 °C prior to analysis. Proteins were separated by SDS-PAGE, ensuring equal loading of soluble and insoluble fractions for direct comparison of protein solubility.

3.3.5 Malachite Green assay

ATPase activity was determined using a colorimetric malachite green assay based on the quantification of inorganic phosphate released during ATP hydrolysis, following the manufacturer’s instructions (Malachite Green Phosphate Assay Kit, Merck, MAK307). The assay is based on the colorimetric detection of free inorganic phosphate released during enzymatic reactions. Free orthophosphate reacts with molybdate and Malachite Green dye to form a stable green-coloured complex. ATP hydrolysis results in the liberation of inorganic phosphate, allowing indirect detection of ATPase activity through measurement of phosphate accumulation.

ATPase reactions were performed in HEPES buffer (pH 8.0) supplemented with 2.5 mM $MgCl_2$ to enable ATP hydrolysis. All buffers were prepared phosphate-free to minimize background signal. Reactions were initiated by the addition of 10 µl ATP from a 4 mM stock solution. Samples were incubated at room temperature, and phosphate release was monitored over a period of 30 minutes. Measurements were taken at defined time points during the reaction, with sampling intervals adjusted depending on the experimental setup.

For phosphate detection, 80 µl of each reaction sample was transferred into a transparent flat 96-well plate, followed by the addition of 20 µl freshly prepared working reagent (Reagent A and B mixed at a ratio of 100:1). After gentle mixing, samples were incubated for 30 minutes at room temperature to allow colour development. Absorbance was measured at 620 nm using an Infinite® 200 microplate reader (Tecan).

3.3.6 Enzyme-coupled NADH assay

ATPase activity was determined using an enzyme-coupled assay based on NADH oxidation (Lindsley, 2001). In this system, ATP hydrolysis is coupled to the regeneration of ATP by pyruvate kinase (PK) and the subsequent conversion of pyruvate to lactate by lactate dehydrogenase (LDH), resulting in the oxidation of NADH to NAD^+. The decrease in NADH concentration was monitored spectrophotometrically at 340 nm as an indirect measure of ATPase activity.

The reaction was performed in HEPES buffer supplemented with $MgCl_2$ at a final concentration of 1 mM. The reaction master mix contained final concentrations of 50 mM HEPES (pH 8.0), 60 µg/mL pyruvate kinase (Roche), 32 µg/mL lactate dehydrogenase (Roche), 9 mM phosphoenolpyruvate (PEP, Roche), and 0.15 mM NADH (Roche).

For each reaction, 140 µl of master mix was combined with 1 µl of protein sample in a 96-well microplate. Reactions were initiated by the addition of 2 µl ATP from a 0.2 M stock solution. As a positive control, apyrase from potato (Sigma Alderich) was included at 0.5 µl per reaction. Control reactions lacking enzyme and/or proteins were used to determine background signal. The decrease in NADH absorbance at 340 nm was monitored over time using a microplate reader (Infinite® 200 PRO, Tecan), and measurements were recorded at defined intervals to assess reaction kinetics.

3.4 Plant methods

3.4.1 Growth conditions for *A. thaliana*

Arabidopsis plants were grown in the greenhouse on soil under long-day conditions.

3.4.2 Seed sterilisation

Chlorine gas sterilisation provides a highly effective method for surface sterilisation of large seed batches without direct liquid contact, thereby reducing the risk of seed loss or damage during handling. In contrast, ethanol-based sterilisation offers a rapid and easily applicable alternative for smaller sample sizes, although repeated washing steps may increase the risk of seed loss. The choice of method was therefore guided by sample size and handling requirements.

3.4.3 Chlorine gas sterilisation

For sterilisation using chlorine gas, seeds were transferred into open microcentrifuge tubes and placed inside a desiccator. To ensure efficient exposure, seeds were evenly distributed to maximize their surface area. A glass beaker containing 20 mL of 12 % sodium hypochlorite solution was placed in the desiccator, and 2.5 mL of 37 % hydrochloric acid was added to generate chlorine gas. The desiccator was immediately sealed, and the seeds were exposed to the gas for 3-4 hours.

3.4.4 Ethanol-based sterilisation

For liquid sterilisation, seeds were placed in microcentrifuge tubes and incubated in 70 % ethanol supplemented with 0.1 % SDS. The suspension was gently mixed by shaking or rotation at 6 °C for 10-30 minutes. After removal of the solution, seeds were treated with 100 % ethanol containing 0.1 % SDS and incubated again under the same conditions. Following the second incubation, the ethanol was removed, and the seeds were spread onto sterile filter paper (Whatman). After complete evaporation of the ethanol, the seeds were collected and transferred into sterile tubes for subsequent use.

3.4.5 Generation of stably transformed *A. thaliana* by floral dipping

Stable transformation of *A. thaliana* was performed using the floral dip method, a widely established and efficient technique for *Agrobacterium*-mediated gene transfer that does not require tissue culture steps (Clough & Bent, 1998).

A. tumefaciens strains carrying the respective constructs were first used to inoculate a 5 mL pre-culture in selective YEB medium, which was grown overnight at 28 °C with shaking at 220 rpm. The following day, 200 mL of selective YEB medium was inoculated with the pre-culture and incubated under the same conditions until the culture reached a dense, turbid state (1-2 days). Prior to transformation, sucrose (10 g per 200 mL culture) and Silwet L-77 (40 µl) were added to the bacterial suspension to facilitate plant infection. The suspension was incubated briefly for approximately 10 minutes under growth conditions to ensure proper mixing. Flowering *A. thaliana* plants were then inverted and submerged in the *Agrobacterium* solution for approximately 30 seconds, ensuring thorough coverage of all inflorescences.

Following floral dipping, plants were incubated horizontally in a humid and dark environment for 24 hours to promote transformation efficiency. Thereafter, plants were returned to standard greenhouse conditions and allowed to develop seeds.

To identify transgenic progeny, harvested seeds were subjected to selection according to the construct used. Selection was performed either by fluorescence-based screening of seeds, by germination on MS medium supplemented with 25 µg/mL hygromycin, or by direct sowing on soil followed by phenotypic screening. Resistant seedlings were identified after 7-10 days, transferred to individual pots if necessary, and cultivated for further propagation and analysis.

3.4.6 Crossing of *A. thaliana*

For genetic crosses, flowering *A. thaliana* plants were emasculated by carefully removing the anthers while keeping the petals intact. The exposed stigma of the emasculated plants was then pollinated with pollen from the desired crossing partner. Crossed plants were cultivated under standard greenhouse conditions until silique development and maturation of F1 seeds occurred.

3.4.7 Leaf preparation for microscopy

To examine trichome branching in young leaves, seedlings aged 7-10 days grown on soil were used, focusing on leaf 1 or 2 where active branching occurs. Cotyledons, the main part of the

hypocotyl and roots were removed, leaving only a small part of the hypocotyl attached to the target leaf. The prepared sample was positioned on a microscope depression slide containing 1 % Agar. For confocal microscopy, the sample was covered with a coverslip.

3.5 *In silico* methods

3.5.1 Cloning & sequencing analysis

Sequencing was carried out by Eurofins Genomic. All computational cloning, sequence alignments, and analysis, including evaluation of sequencing data, were carried out using CLC DNA Workbench 5.6.1 and CLC Main Workbench 22.

3.5.2 Sequence retrieval and domain annotation

The amino acid sequence of STICHEL (UniProt ID: O64728) from *A. thaliana* was retrieved from the UniProt database. Domain architecture and conserved sequence features were analysed using the InterPro platform, integrating signatures from multiple databases including Pfam and PANTHER. Predicted domains, functional annotations, and Gene Ontology (GO) terms were extracted from the InterPro output (Blum et al., 2021). Theoretical molecular weights of recombinant proteins were calculated using the ExPASy ProtParam tool (Gasteiger et al., 2005, accessed May 2026).

3.5.3 Identification of conserved motifs

Conserved motifs characteristic of P-loop NTP-binding proteins were identified by manual inspection of the protein sequence within the predicted ATPase-like region. The Walker A motif was assigned based on the consensus sequence GxxxxGK[T/S], and the Walker B motif was identified based on the presence of conserved acidic residues, typically hhhhDE, associated associated with ATP hydrolysis (Walker et al., 1982). Motif positions were defined relative to the full-length STI sequence.

3.5.4 Multiple sequence alignment

Multiple sequence alignments were performed using the MAFFT algorithm (Katoh & Standley, 2013). Sequences of representative AAA^+ ATPases, including bacterial and eukaryotic clamp loader subunits, were selected for comparison. For analysis of conserved sequence features

within interacting NET1 fragments, additional motif discovery analysis was performed using the MEME Suite version 5.5.9 (Bailey & Elkan, 1994). Alignments were visualized and analysed using Jalview (Waterhouse et al., 2009), allowing assessment of sequence conservation and motif positioning. Conservation scores and consensus sequences were calculated within Jalview based on residue conservation at each alignment position, taking amino acid identity and physicochemical similarity into account.

3.5.5 Domain architecture visualization

Schematic representations of protein domain organization and motif positions as well as nucleotide schematic representations were generated using IBS Illustrator (Liu et al., 2015). Annotated features included predicted domains, Walker motifs, and domain boundaries were derived from InterPro analysis (Blum et al., 2021).

3.5.6 Structure prediction and visualization

The three-dimensional structure of STICHEL was obtained from the AlphaFold protein structure database (Jumper et al., 2021; Varadi et al., 2022). The predicted model includes per-residue confidence scores (pLDDT), which were used to assess structural reliability. Structural visualization and figure preparation were performed using UCSF ChimeraX (Pettersen et al., 2021). Structures were displayed in cartoon representation and coloured either by pLDDT confidence values or by manually defined residue ranges. Specific regions of interest, including the central domain (amino acids 450-850) and conserved Walker motifs, were highlighted using residue-based selections.

3.5.7 Structural figure generation

For visualization of structural features, the STI model was rendered in ChimeraX (Pettersen et al., 2021) using standard cartoon representations. The central region was highlighted based on residue numbering, and conserved motifs were displayed as stick representations. Figures were exported as high-resolution images for inclusion in the manuscript. Example ChimeraX command generated in assistance with Perplexity is provided in the Appendix.

3.6 Microscopy

3.6.1 Light microscopy

Whole leaves were imaged to assess trichome phenotypes using a LEICA MZ16 F stereomicroscope with the automated z-stack function. Image documentation was performed with the LEICA DFC420 C camera system and the Leica Application Suite X software (version 3.4.2, build 18368).

3.6.2 Confocal laser scanning microscopy

Images were acquired using a Leica Stellaris confocal microscope equipped with a DMI8 inverted stand, a White Light Laser (WLL), and the FALCON Fast Lifetime Contrast system. Image acquisition was controlled using LAS X software (version 3.7.4).

4 Results

4.1 *In silico* characterization of STICHEL (AT2G02480)

The *A. thaliana* protein STICHEL (STI; AT2G02480; UniProt O64728) comprises 1218 amino acids. For functional analyses, the protein has previously been subdivided into three fragments: An N-terminal fragment (S1; amino acids 1-454), a central fragment (S2; amino acids 455-800), and a C-terminal fragment (S3; amino acids 800-1218). Previous studies reported that the central S2 region of STI (amino acids 454-799) shows sequence similarity to the γ subunit of bacterial DNA polymerase III and to replication factor C (RFC)-like ATPase domains (Ilgenfritz et al., 2003; Xi et al., 2018).

Advances in computational biology have substantially expanded the possibilities for protein sequence analysis, structure prediction, and motif identification. In particular, the development of deep learning-based approaches has significantly improved the accuracy of protein structure prediction, most notably through tools such as AlphaFold (Jumper et al., 2021; Varadi et al., 2022). These methods enable high-confidence structural predictions even for proteins lacking experimental structural data. In parallel, a wide range of online tools for sequence analysis and functional annotation has become readily accessible, facilitating the identification of conserved domains, structural features and regulatory motifs. Given these advances, STI was re-evaluated using current bioinformatic approaches to refine domain predictions and guide subsequent experimental design.

4.1.1 Domain prediction of central AAA$^+$-ATPase-like region and identification of conserved nucleotide-binding motifs

To characterize STI sequence features using current bioinformatic approaches, domain prediction analyses were performed with InterPro (Blum et al., 2021), Pfam (Mistry et al., 2021), and the NCBI Conserved Domain Database (Lu et al., 2020). These analyses consistently identified a central region spanning approximately amino acids 450-850 that shows similarity to clamp loader-type AAA$^+$ ATPases. Within this region, several overlapping annotations were identified, including a DNA polymerase III γ/τ-like domain, a P-loop-containing nucleoside triphosphate hydrolase core, and additional subdomains corresponding to an ATPase lid domain, γ/τ domain III, and a post-AAA$^+$ oligomerization domain.

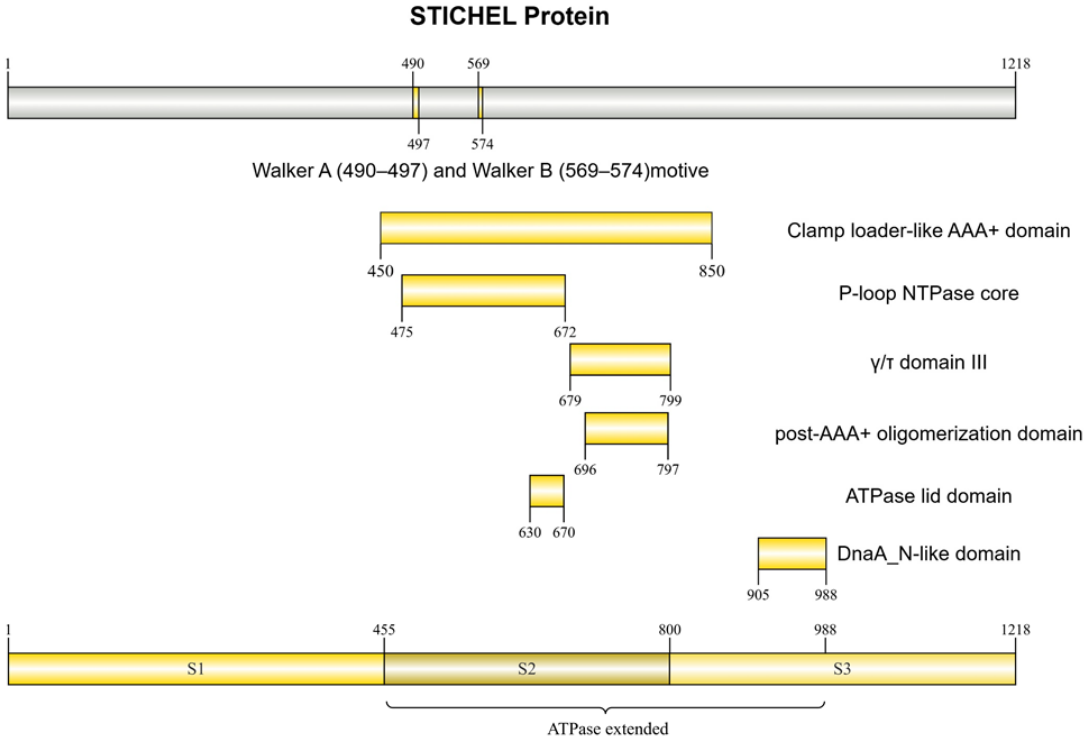

Fig. 9: Domain architecture of STICHEL (AT2G02480).

STI is a 1218 amino acid protein containing a central clamp loader-like AAA$^+$ domain spanning approximately amino acids 450-850. Within this region, a P-loop NTPase core (aa 475-672) and additional subdomains characteristic of γ/τ-like clamp loader ATPases, including the ATPase lid domain (aa 630-670), γ/τ domain III (aa 679-799), and a post-AAA$^+$ oligomerization domain (aa 696-797), were identified based on InterPro and Pfam annotations. Conserved nucleotide-binding motifs were manually annotated, including the Walker A motif (aa 490-497) and Walker B motif (aa 569-574). A distinct C-terminal α/β domain with similarity to DnaA_N-like folds is present at amino acids 905-988. The ATPase extended fragment comprises the S2 fragment and the newly identified DnaA_N-like α/β domain (aa 455-988). Domain boundaries are based on sequence-based predictions. Protein fragments used in this study are indicated below the domain scheme. Figure created in IBS.

In addition to the central region, a distinct C-terminal domain (amino acids ~905-988) was identified and annotated as a STICHEL/DnaA_N-like α/β domain. To include the newly identified C-terminal domain in subsequent functional analyses, an extended construct comprising the S2 fragment and the C-terminal region was generated. It was named “ATPase extended” and ranges from amino acid 455-988. The N-terminal region (amino acids 1-450) did not show clear similarity to characterized domains in the databases used.

The domain organization of STI based on these analyses is shown in Fig. 9.

To further evaluate the predicted ATPase-containing region, conserved sequence motifs characteristic of P-loop NTP-binding proteins were identified by manual sequence inspection

based on established consensus motifs described for Walker-type NTPases (Leipe et al., 2002; Walker et al., 1982).

A Walker A motif consistent with the consensus sequence GxxxxGK[T/S], which is typically associated with nucleotide phosphate binding, was identified at amino acids 490-497 (GPRGTGKT) (Walker et al., 1982). In addition, a sequence matching the general characteristics of a Walker B motif (hhhhDE), commonly involved in ATP hydrolysis, was identified at amino acids 569-574 (VFVIDE) (Erzberger & Berger, 2006; Walker et al., 1982).The spacing between these motifs (~79 amino acids) falls within the range commonly observed for P-loop NTP-binding domains and AAA^+-associated ATPases (Erzberger & Berger, 2006; Leipe et al., 2002). Together, these features raised the possibility that STI may contain a functional ATP-binding and hydrolysis domain.

4.1.2 Conserved Walker motifs in STI align with canonical AAA^+ ATPases

To assess whether the predicted ATPase-like region of STI contains conserved residues and motifs characteristic of functional AAA^+ ATPases, a multiple sequence alignment was performed with representative members of the AAA^+ ATPase superfamily, including bacterial DnaX, yeast RFC1, and *E. coli* ClpX, which represent structurally and functionally distinct ATP-dependent molecular machines (Erzberger & Berger, 2006). The alignment was restricted to the central region identified by domain prediction analyses in order to focus on homologous sequence elements.

Fig. 10: Multiple sequence alignment of the predicted ATPase core region of STI with representative AAA$^+$ ATPases.

Alignment of the central region of *A. thaliana* STICHEL with selected AAA$^+$ ATPases, including bacterial DnaX, yeast RFC1, and *E. coli* ClpX. The Walker A motif (GxxxxGK[T/S]) is highlighted in blue, and the Walker B motif (hhhhDE) is highlighted in red. Amino acid positions correspond to the respective protein sequences. The alignment is restricted to the predicted ATPase-containing region. Conserved residues within the highlighted motifs are visible across the aligned sequences. The alignment was generated using MAFFT (Katoh & Standley, 2013) and visualized in Jalview (Waterhouse et al., 2009).

As shown in Fig. 10, the Walker A motif (highlighted in blue) and the Walker B motif (highlighted in red) are present in the STI sequence and align with corresponding regions in the selected reference proteins.

Sequence analyses therefore suggested that STI contains a central region with characteristic features of P-loop NTP-binding proteins. In addition to the conserved Walker A and Walker B motifs, domain prediction approaches indicated the presence of a central AAA$^+$-like ATPase region and a C-terminal DnaA_N-like α/β domain. To further investigate the structural organization of these predicted domains, AlphaFold-based structural models of STI were subsequently analysed (Jumper et al., 2021; Varadi et al., 2022).

4.1.3 Structural organization of STI predicted by AlphaFold

To further assess the structural organization of STI, a three-dimensional model was obtained from the AlphaFold Protein Structure Database (UniProt ID: O64728) (Jumper et al., 2021; Varadi et al., 2022). The model provides per-residue confidence estimates (pLDDT), allowing discrimination between well-defined and potentially disordered regions.

Visualization of the predicted structure revealed a clear distinction between a compact, well-folded central region and extended peripheral regions with low structural confidence (Fig. 11). The central portion of the protein, corresponding approximately to amino acids 450-750, is characterized by predominantly α-helical and β-sheet elements and exhibits high to intermediate confidence scores, consistent with a structured protein core.

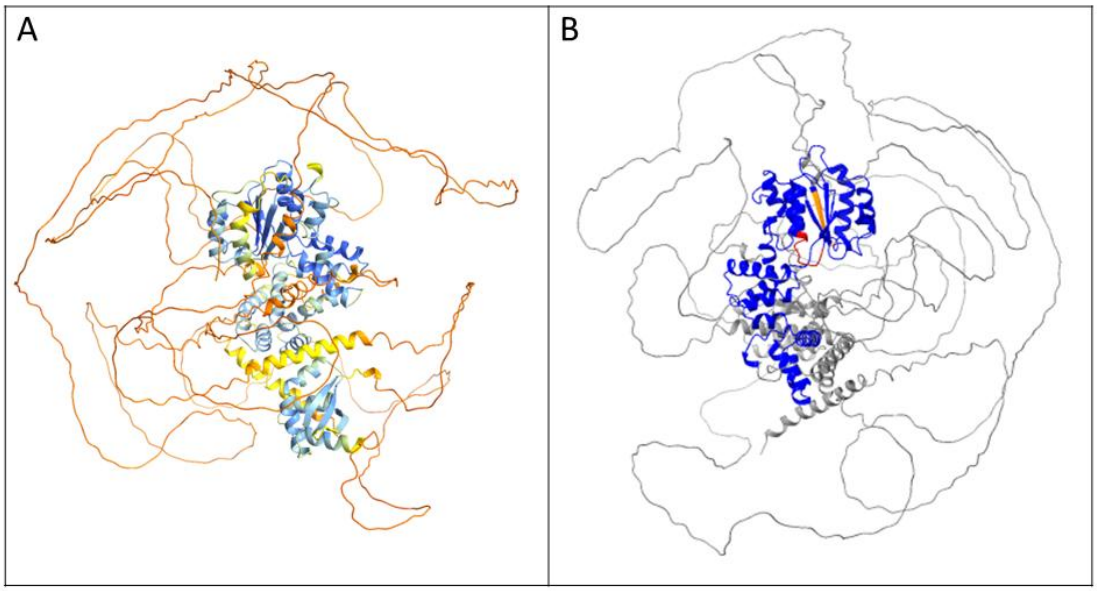

Fig. 11: Structural prediction of STICHEL and localization of conserved ATPase motifs.

A: AlphaFold-predicted structure of STICHEL (UniProt ID: O64728) coloured according to per-residue confidence (pLDDT). Regions of high confidence are shown in blue, intermediate confidence in light blue/yellow, and low confidence in orange, indicating potentially flexible or disordered regions. B: Representation of the central region (amino acids 450-750) highlighted in blue within the full-length structure (grey). The conserved Walker A (amino acids 490-497) and Walker B (amino acids 569-574) motifs are shown as stick representations in red and orange, respectively

In contrast, large parts of the N-terminal and C-terminal regions display low pLDDT values and are predicted to adopt flexible or intrinsically disordered conformations. These regions form extended, loop-like structures surrounding the central folded core.

Mapping of conserved sequence features onto the AlphaFold model showed that the previously identified Walker A (amino acids 490-497) and Walker B (amino acids 569-574) motifs are located within the structured central region (Fig. 11). Both motifs are positioned in spatial proximity within the folded core, consistent with their assignment to a P-loop NTP-binding fold (Erzberger & Berger, 2006; Leipe et al., 2002; Walker et al., 1982)

Since many AAA^+ ATPases act as multimeric assemblies, potential oligomerization of STI represents an important aspect for functional interpretation. However, no higher-order assembly or oligomeric arrangement can be inferred from the AlphaFold monomeric model.

4.2 Recombinant expression and solubility assessment of STI fragments

The comprehensive *in silico* analysis of STI revealed a domain that potentially translates into an ATPase domain with motifs for ATP binding and hydrolysis. AlphaFold-based structural modelling supported the presence of a structured central core within the predicted ATPase-like region and the question arises, if the predicted domain functions as an active ATPase. To assess possible ATPase activity, the predicted ATPase-containing regions S2 and ATPase extended were recombinantly expressed in *E. coli* RIL cells and subsequently purified for biochemical analysis. Different expression conditions were tested to optimize protein production. Optimal expression was achieved using overnight cultures grown at 37°C, followed by induction of the main culture at an OD600 of approximately 0.8 with 0.5 mM IPTG and subsequent incubation at 18°C for 16 h.

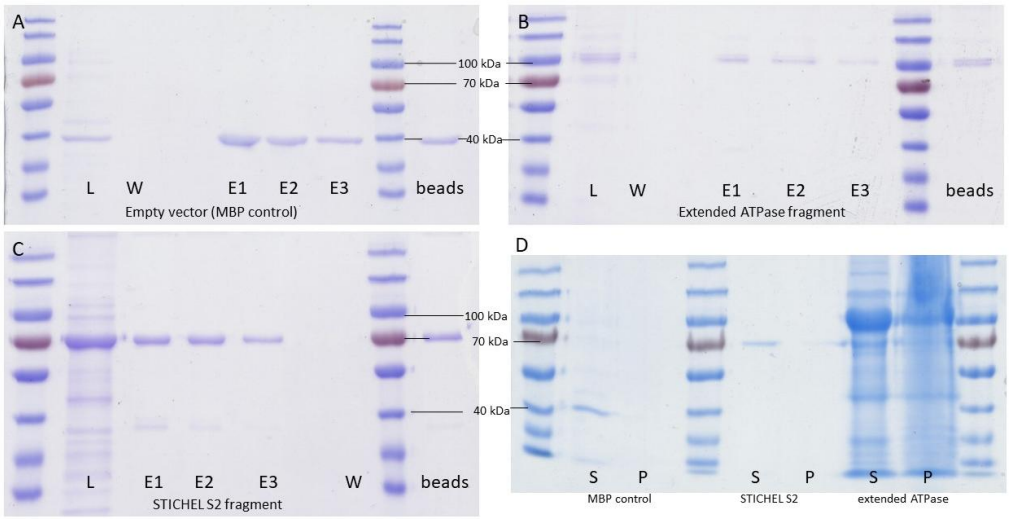

Fig. 12: Purification and solubility of recombinant STI fragments

A-C: Affinity purification of MBP-tagged proteins using amylose resin. The MBP tag has an approximate molecular weight of 40 kDa and contributes to the observed size of all fusion proteins. A: MBP control (empty vector), B: extended ATPase fragment (101.1 kDa), and C: STI S2 fragment (78.7 kDa). Protein fractions are indicated as follows: L, lysate; W, wash; E1-E3, elution fractions obtained with increasing maltose concentrations (E1: 10 mM, E2: 20 mM, E3: 30 mM); beads, amylose resin after elution. D: Solubility analysis of expressed proteins. Samples were separated into soluble (S, supernatant) and insoluble (P, pellet) fractions after cell lysis. Differences in band intensity between samples in panel (D) reflect unequal sample loading due to variations in the amount of material recovered from the pellet and do not allow conclusions regarding relative protein solubility. Molecular weight estimation was performed using the Thermo Scientific PageRuler Prestained Protein Ladder.

Protein solubility was assessed following cell lysis and fractionation into soluble and insoluble fractions (see 3.3.4 Protein solubility assay). Both constructs were detected in the soluble

fraction, indicating that the expressed proteins were present in a soluble form (Fig. 12D). Differences in band intensity observed in the solubility assay are due to unequal sample loading resulting from variations in the amount of material recovered from the pellet and therefore do not reflect differences in protein solubility.

Under these conditions, both the original S2 fragment and the extended ATPase fragment were successfully expressed, as indicated by the presence of protein bands corresponding to the expected molecular weights (Fig. 12). Based on theoretical molecular weight calculations using the ExPASy ProtParam tool (Gasteiger et al., 2005), MBP alone was expected at approximately 39.8 kDa, the MBP-S2 fusion protein at approximately 78.7 kDa, and the MBP-ATPase extended fusion protein at approximately 101.1 kDa.

4.3 ATPase activity analyses of recombinant STI fragments

Previous genetic and bioinformatic studies suggested the presence of ATPase-associated features within *STI* (Ilgenfritz et al., 2003), but available experimental observations remained inconclusive. In particular, inconsistent phenotypic effects observed for ATPase motif mutants *in planta* did not allow clear conclusions regarding the biochemical function of STI (Huang, 2008, Dr. Swen Schellmann pers. communication). To directly assess whether STI possesses intrinsic ATPase activity, recombinant STI fragments containing the predicted ATPase-associated region were analysed using two independent *in vitro* ATPase assay systems.

4.3.1 Assessment of STI ATPase activity by Malachite Green assay reveals no detectable phosphate release

To investigate whether STI exhibits ATPase activity, a colorimetric Malachite Green assay (Sigma-Alderich, see 3.3.5 Malachite Green assay). was performed to detect the release of inorganic phosphate. The assay was conducted according to the manufacturer's protocol with minor adaptations. Instead of generating a full standard curve, a defined phosphate standard was included in each experiment to serve as a reference for phosphate detection. Potato apyrase (A7646, Sigma-Alderich) was used as a positive control to validate assay performance. Apyrases belong to the NTPDase family and catalyse the sequential hydrolysis of ATP and ADP, ultimately generating AMP and inorganic phosphate (Knowles, 2011). Unlike classical

ATPases that typically catalyse a single ATP hydrolysis step, the apyrase control therefore reflects cumulative phosphate release.

Initial experiments were performed to establish suitable assay conditions. Different reaction times, buffer systems (HEPES buffer and TBS buffer), and pipetting schemes were tested (Fig. 32, Fig. 33, Fig. 34). Rapid colour development was observed for the positive control, with signal saturation occurring within a few minutes. Based on these observations, the assay was subsequently evaluated under conditions suitable for qualitative detection rather than quantitative kinetic analysis. A reaction time of 10 min was selected for subsequent experiments, as signal intensities remained saturated. ATP was added last to initiate the reaction, while all other assay components were pre-mixed prior to the start of the assay.

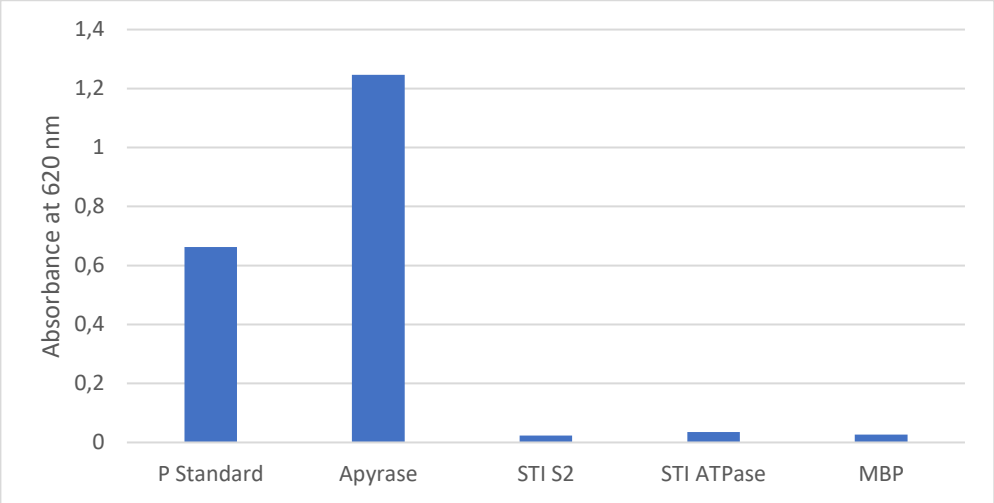

Fig. 13: Representative Malachite green-based ATPase assay of STI-derived protein fragments.

ATPase activity was assessed by measuring the release of inorganic phosphate. A phosphate standard and potato apyrase were included as positive controls. While strong signals were observed for both controls, no detectable phosphate release above background levels was observed for the STI S2 fragment or the extended ATPase fragment under any tested condition. MBP represents a negative control. Shown are representative endpoint measurements after 10 min from one experiment optimized for qualitative detection.

ATPase activity was assessed for the STI S2 fragment and the extended ATPase fragment under various conditions, including freshly purified protein, stored protein (4°C and -20 C), and different preparation states. Across all tested conditions, no detectable phosphate release above background levels was observed for any of the STI-derived samples. Different buffer systems and protein preparations were tested, all yielding comparable negative results (Fig. 32, Fig. 33, Fig. 34).

In contrast, a strong signal was consistently detected for both the phosphate standard and the apyrase control, confirming proper assay performance (Fig. 13).

4.3.2 Assessment of STI ATPase activity by coupled enzymatic assay reveals no detectable ATP hydrolysis

Although the Malachite Green assay successfully detected phosphate release in the positive control, no measurable activity could be observed for the STI fragments, therefore an 3.3.6 Enzyme-coupled NADH assay was subsequently employed as a more sensitive and continuous method to monitor ATP hydrolysis indirectly through enzymatic conversion of reaction products (Lindsley, 2001). In this assay, ATP hydrolysis is linked to NADH oxidation via pyruvate kinase and lactate dehydrogenase, allowing indirect detection of ATP turnover by monitoring the decrease in NADH levels. Reactions were initiated by addition of ATP, and changes in NADH levels were monitored by absorbance measurements over time.

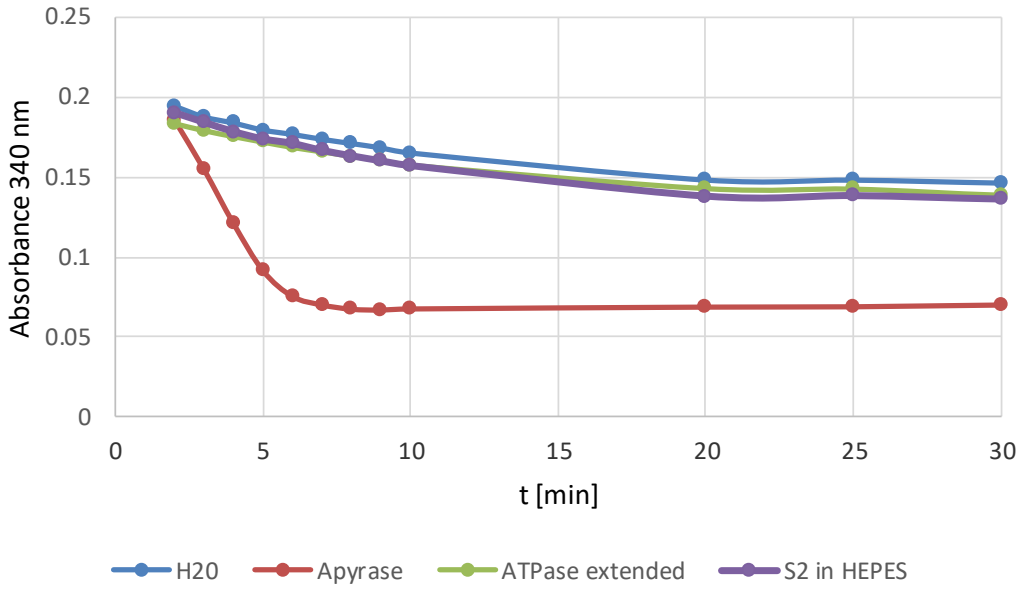

Fig. 14: Coupled enzymatic ATPase assay monitoring NADH consumption over time.

ATPase activity was assessed using a coupled assay linking ATP hydrolysis to NADH oxidation. NADH levels were monitored by measuring absorbance at 340 nm over time. Values shown represent the mean of two replicates per condition. Apyrase served as a positive control and showed a rapid decrease in absorbance, indicating ATP hydrolysis and coupled NADH consumption, followed by a plateau phase after approximately 7 min, consistent with reaction saturation. In contrast, the STI-derived fragments ("ATPase extended" and "S2 in HEPES") displayed absorbance profiles comparable to the H_2O control and no detectable ATPase activity under the tested conditions.

A positive control using potato apyrase (Sigma-Alderich) resulted in a clear decrease in NADH signal, confirming that the assay system was functional (Fig. 14). In contrast, no detectable change in NADH levels was observed for the STI S2 fragment or the extended ATPase fragment under the tested conditions. For additional negative assay results testing TBS and HEPES buffer conditions see Fig. 35. These results are consistent with the findings obtained using the Malachite Green assay. Together, these findings suggest that the tested STI fragments do not exhibit detectable intrinsic ATPase activity under the applied *in vitro* conditions.

4.4 Establishment and evaluation of CRISPR/Cas9 strategies for targeted genome editing in *A. thaliana*

Although the conducted *in vitro* experiments provided important initial insights, such approaches cannot fully reproduce the complex physiological environment present in plant cells, where protein activity and regulation may depend on additional cofactors, interaction partners, cellular compartmentalization, or developmental and environmental cues. To facilitate future investigations of STI under physiological conditions, transgenic reporter lines were generated as a tool for *in planta* analyses of gene expression, protein localization, and potential biological function. The existing GFP-STI reporter line under the constitutive 35S promoter proved to be insufficient to tackle *STI* analysis (see 1.5.1 Limitations of the constitutive GFP-STI reporter system). Genome editing approaches using the CRISPR/Cas9 system to tag the endogenous *STI* with fluorophores were established. Furthermore, T-DNA insertion lines with 35S::STI-tdTomato were generated (see 3.4.5 Generation of stably transformed *A. thaliana* by floral dipping).

4.4.1 CRISPR/Cas9-mediated knock-in using a pre-existing egg cell-specific Cas9 system

An initial strategy for the CRISPR/Cas9-mediated knock-in was based on a previously established *A. thaliana* line expressing Cas9 under the egg cell-specific promoter DD45 (Mao et al., 2016). This parental line carries a mutation in the *GL2* gene, resulting in a trichomeless phenotype and serving as a functional indicator of Cas9 activity (Fig. 15 B). It proved to efficiently generate heritable CRISPR/Cas9-mediated homology-directed repair (HDR)-events in *Arabidopsis* (Mao et al., 2016; D. Miki et al., 2018).

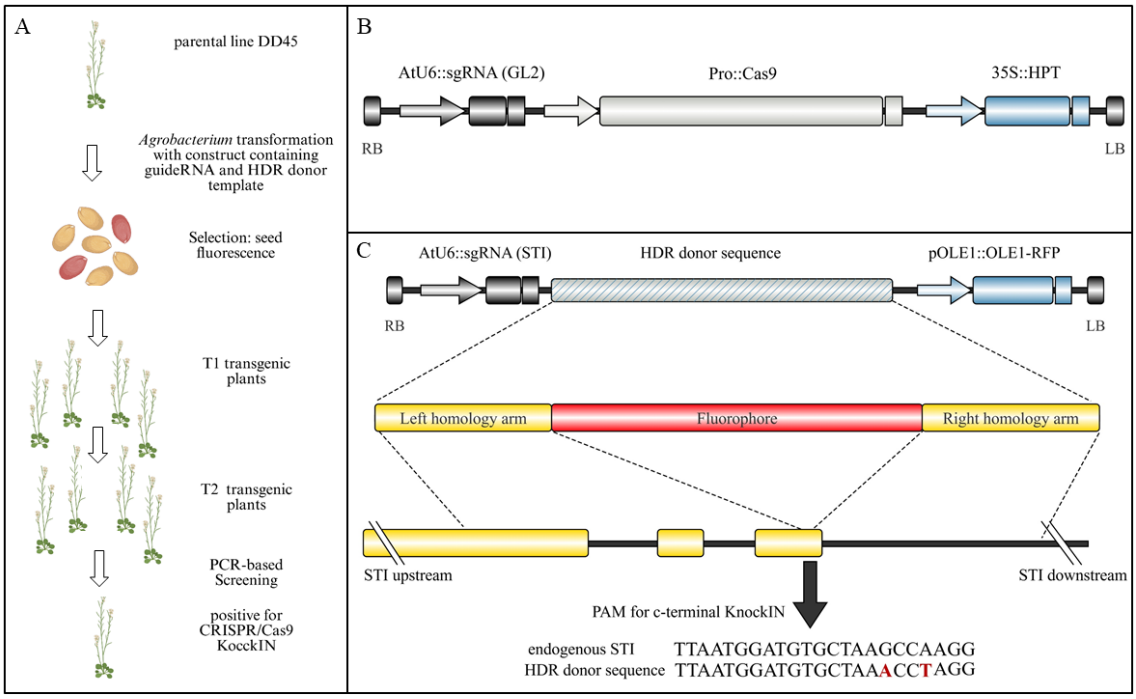

Fig. 15: Strategy for CRISPR/Cas9-mediated HDR knock-in in *A. thaliana* using an egg cell-specific *Cas9* system expressed in a parental line.
A: Schematic overview of the workflow. A parental *A. thaliana* line expressing *Cas9* under control of the DD45 promoter was transformed via *Agrobacterium* with a construct containing a guide RNA (targeting *STI*) and an HDR donor template. Transgenic seeds were identified by seed fluorescence, followed by propagation of T1 and T2 generations and PCR-based screening for positive knock-in events. B: Structure of the parental *Cas9* construct containing an AtU6-driven sgRNA cassette, *Cas9* expression cassette, and the hygromycin resistance marker (*35S::HPT*). C: Structure of the HDR donor construct used for *STI* C-terminal fluorophore knock-in. The construct contains an AtU6-driven sgRNA targeting *STI*, the HDR donor sequence consisting of left and right homology arms flanking the fluorophore sequence, and the seed fluorescence selection cassette *pOLE1::OLE1-RFP*. The lower panel illustrates the targeted *STI* genomic locus and the position of the C-terminal knock-in. Silent nucleotide substitutions were introduced into the donor sequence in the protospacer region to prevent Cas9-mediated re-cutting after homologous recombination. Adapted from (D. Miki et al., 2018). Figure created in BioRender and IBS.

To generate STI fusion constructs, the vectors HY098 and HY100 were introduced into the DD45 background via floral dipping (see 3.4.5). These constructs were designed to fuse the red fluorescent protein tdTomato to the N- or C-terminus of STI, respectively. tdTomato is well suited as a reporter for fluorescence-based localization studies in plant cells due to its high brightness, rapid maturation, and strong photostability (Shaner et al., 2004). Together with the fluorescent protein, flanking homology arms result in the HDR template for the knock-in. The left homology arm represents the upstream sequence of the introduced cut, whereas the right homology arm represents the downstream sequence of the cut. For construct HY098 (N-terminal tag), the STOP Codon of the tdTomato sequence was removed. The left homology arm consisted of 601 bp, ending with the 16th nucleotide of the *STI* CDS. The right homology arm

consisted of 601 bp and ended in the first exon of *STI* (position 617). For construct HY100 (C-terminal tag), the left homology arm consisted of 590 bp, starting in the 4th exon and ending in the 6th and last exon of *STI* at position 3624 of the CDS. The right homology arm consisted of 600 bp and started at position 3625 of the *STI* CDS. A schematic representation for construct design for the C-terminal Knock-in is visible in Fig. 15C, the same figure for the N-terminal knock-in construct is shown Fig. 36. All coding sequences were codon-optimized for expression in *A. thaliana*. Exact sequences are given in the appendix (Sequences of *STI* knock-in constructs).

Due to the high AT content of the *STI* upstream and downstream regions, which reached up to 75%, conventional cloning of the HDR donor sequences was not successful. Therefore, the donor sequences were synthesized commercially by Genewiz Gene Synthesis Service.

After transformation of the parental line with the constructs HY098 and HY100, seeds of the T1 were screened for seed fluorescence. No fluorescence was detected in seeds derived from HY098, and this construct was therefore excluded from further analysis. In contrast, a small number of fluorescent seedlings were obtained from HY100 and propagated to the next generation. In the subsequent T2 generation, five out of six lines derived from HY100 produced fluorescent seeds. The observed segregation pattern of fluorescent versus non-fluorescent seeds in the T2 was approximately consistent with Mendelian inheritance of a single insertion locus (approximately 3:1 fluorescent to non-fluorescent seeds). To enrich for lines with stable integration, about 100 seeds exhibiting the strongest fluorescence were selected for further analysis. The screening workflow for selection is visualized in Fig. 15A.

4.4.1.1 T1 plants display a glabrous phenotype

T1 plants obtained after floral dip transformation of the DD45-Cas9 parental line displayed a strongly reduced trichome phenotype (Fig. 16). The observed phenotype was consistent with the glabrous background of the parental line used for the CRISPR/Cas9-mediated knock-in approach.

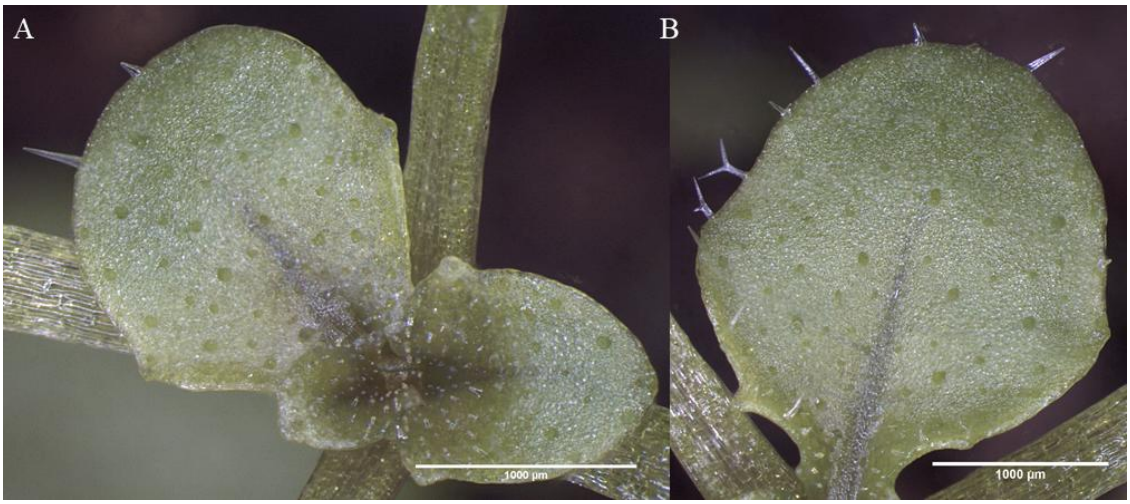

Fig. 16: Reduced trichome formation in T1 plants generated by CRISPR/Cas9-mediated STI-tdTomato knock-in.

Representative T1 plants carrying the endogenous STI-tdTomato knock-in construct. T1 plants displayed strongly reduced trichome formation consistent with the glabrous DD45-Cas9 parental background. Residual trichomes were occasionally observed in individual plants. Scale bars = 1000 µm.

Because the T1 generation still largely resembled the parental glabrous background, subsequent analyses focused on molecular verification of the knock-in event and initial fluorescence characterization.

4.4.1.2 Genotypic verification of knock-in events

To confirm correct genomic integration of the tdTomato sequence, genomic DNA was isolated from selected plants of the T2 population and analysed using two independent PCR strategies.

In the first approach, a primer combination was used to specifically detect knock-in events. Primer L577 annealed within the inserted tdTomato sequence, while primer HJ062 was positioned outside the homology region of the targeting construct to prevent amplification of residual transformation plasmid DNA. Amplification was therefore only possible in plants carrying a genomic tdTomato integration. PCR analysis identified a subset of plants showing amplification products consistent with successful knock-in events, whereas no amplification was detected in negative controls (Fig. 37). Notably, all PCR-positive individuals originated from a single line, indicating that the observed integration event resulted from a single transformation event. Repetition of the PCR analysis using independently isolated genomic DNA confirmed the reproducibility of the observed banding patterns.

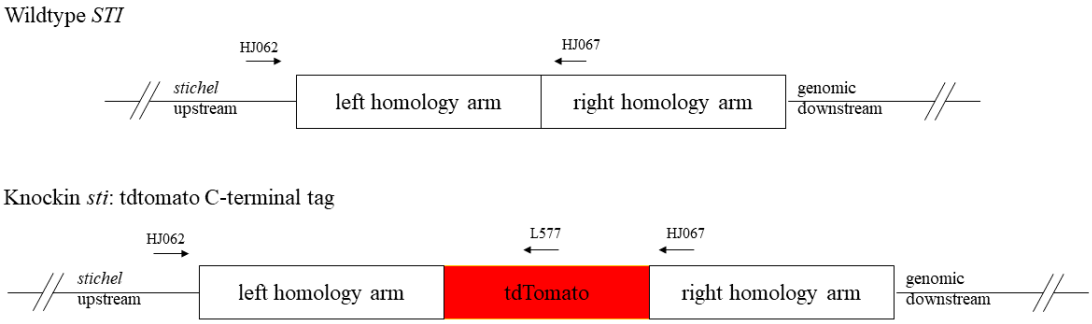

Fig. 17: Schematic representation of PCR strategies used for verification of STI-tdTomato knock-in lines.

In the upper panel, the wild-type *STI* locus is shown without tdTomato insertion. In the lower panel, the knock-in allele carrying a C-terminal tdTomato insertion is depicted. Two independent PCR strategies were used: Primer combination HJ062/L577 specifically detects the knock-in allele, as L577 anneals within the inserted tdTomato sequence and HJ062 anneals outside of the homology arm (to prevent amplification of the transformed plasmid DNA). Primer combination HJ062/HJ067 amplifies both alleles and allows discrimination between genotypes based on fragment size. Amplification of the wild-type allele results in a 728 bp fragment, whereas amplification of the knock-in allele results in a 2159 bp fragment due to insertion of the tdTomato sequence. Created in IBS.

In a second PCR strategy, primers HJ062 and HJ067 were used to distinguish between wild-type and knock-in alleles based on fragment sizes (Fig. 17). In the wild-type locus, amplification resulted in a 728 bp fragment, whereas insertion of the tdTomato sequence increased the fragment size to 2159 bp. Wild-type plants therefore displayed only the smaller 728 bp band, homozygous knock-in plants only the 2159 bp band, and heterozygous plants both bands simultaneously. Based on these banding patterns, plants were classified as homozygous knock-in, heterozygous, or wild type (Fig. 18 and Fig. 38).

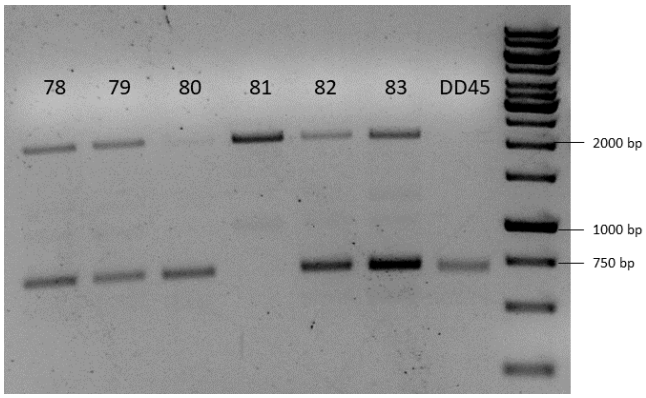

Fig. 18: Gel electrophoresis of PCR-based genotyping of wild-type and knock-in alleles.

Amplification using primers HJ062 and HJ067 resulted in a 728 bp fragment for the wild-type allele and a 2159 bp fragment for the knock-in allele containing the tdTomato insertion. Wild-type plant 80 showed only the 728 bp band, homozygous knock-in plant 81 only the 2159 bp band, and heterozygous plants 78, 79, 82, and 83 both bands. DD45 resembled the parental line and served as a negative control showing the wild-type band. DNA fragment sizes were estimated using the Thermo Scientific GeneRuler 1 kb DNA Ladder. Additional tested plants are shown in Fig. 39.

PCR products corresponding to the knock-in allele were gel-purified and subjected to cloning and sequencing analysis, confirming correct integration of the tdTomato sequence.

4.4.1.3 Initial fluorescence detection in T1 knock-in plants

To assess whether the endogenous STI-tdTomato fusion protein could be detected *in planta*, initial confocal microscopy analyses were performed using T1 plants derived from the CRISPR/Cas9-mediated knock-in approach. Since the parental DD45 Cas9 line displays a glabrous phenotype (Fig. 16), fluorescence analyses were restricted to trichome-like structures.

Weak tdTomato fluorescence signals could be detected in trichome structures (Fig. 19, Fig. 40, Fig. 41). Although the overall fluorescence intensity was low, consistent with endogenous expression of *STI*, fluorescence appeared enriched at the apical region of the developing outgrowths. Additional weaker punctate signals were occasionally observed along the plasma membrane.

These observations demonstrate that the endogenous STI-tdTomato fusion protein is detectable by confocal microscopy despite low expression levels and provide first indications of a non-uniform subcellular localization pattern.

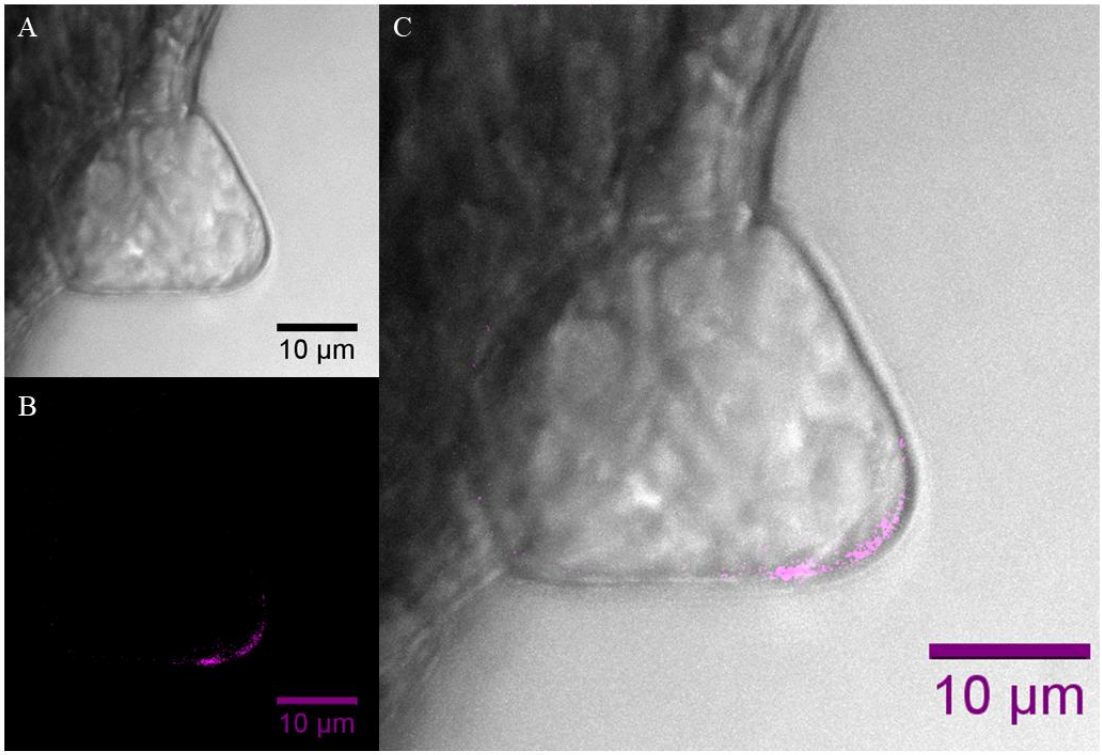

Fig. 19: Weak apical STI-tdTomato fluorescence detected in T1 plants generated by CRISPR/Cas9-mediated knock-in.

Confocal microscopy of epidermal outgrowth structures in T1 plants carrying the endogenous STI-tdTomato knock-in construct. A Brightfield image. B tdTomato fluorescence C Merged image. Weak fluorescence signals were predominantly detected at the apical region of the developing structure. Scale bars = 10 µm.

4.4.1.4 Backcrossing to Col-0 successfully restored the trichome phenotype

To eliminate the CRISPR/Cas9 machinery and obtain stable edited lines, a selected homozygous knock-in plant (number 51) was crossed with a Col-0 wild-type plant using Col-0 pollen. The crossing is not only useful for removing the genome editing components after successful targeting, but also essential because the parental line is glabrous and therefore unsuitable for analysing *STI*-dependent trichome phenotypes and localization patterns in differentiated trichomes (see above). The resulting F1 generation was phenotypically screened with respect to trichome formation. Out of the analysed individuals, 18 plants displayed a wild-type trichome phenotype, whereas 3 plants exhibited a glabrous phenotype (data not shown). Only plants with a wild-type phenotype were selected for further propagation, while glabrous individuals were discarded.

4.4.2 Generation of independent Cas9 parental lines

In parallel to the DD45-parental-line system, additional genome editing strategies were established to increase experimental flexibility and to exclude potential effects of transgene silencing during successive generations. For this purpose, an independent genome editing system with new parental lines expressing Cas9 under the egg cell-specific promoter DD45 were generated using the pEC1.2_EC1.1_spCas9_GFP vector. (HY112).

Because the original parental line described by Mao et al., 2016 was generated and functionally validated using a *GL2*-targeting sgRNA, the resulting plants display a glabrous phenotype. As *STI* function is closely associated with trichome branching, this background was not optimal for phenotypic analysis of *STI*-derived reporter knock-in lines. Therefore, a modified strategy was established in which the CRISPR/Cas9 parental lines were redesigned to target genes directly relevant for the intended downstream analyses. Instead of using *GL2*, independent parental lines were generated carrying sgRNAs targeting *STI* itself as well as *NOK*. This approach provided the additional advantage that successful HDR-mediated knock-in events at the *STI* locus could simultaneously restore the mutant phenotype, thereby directly coupling genome editing success to phenotypic complementation.

To allow insertion of fluorescent tags at different positions within the coding sequence, separate parental lines targeting either the N-terminal or C-terminal region of *STI* were generated, corresponding to the respective HDR insertion sites. In addition, a *NOK*-targeting line was established as an alternative genetic background with a clearly detectable mutant phenotype (Fig. 20). Since *nok* mutants exhibit increased trichome branching (Folkers et al., 1997), this background may facilitate the analysis of STI localization and function in branching-related processes.

Three independent lines were obtained:

HY115: targeting *STI* (N-terminal region)

HY116: targeting *NOK*

HY117: targeting *STI* (C-terminal region)

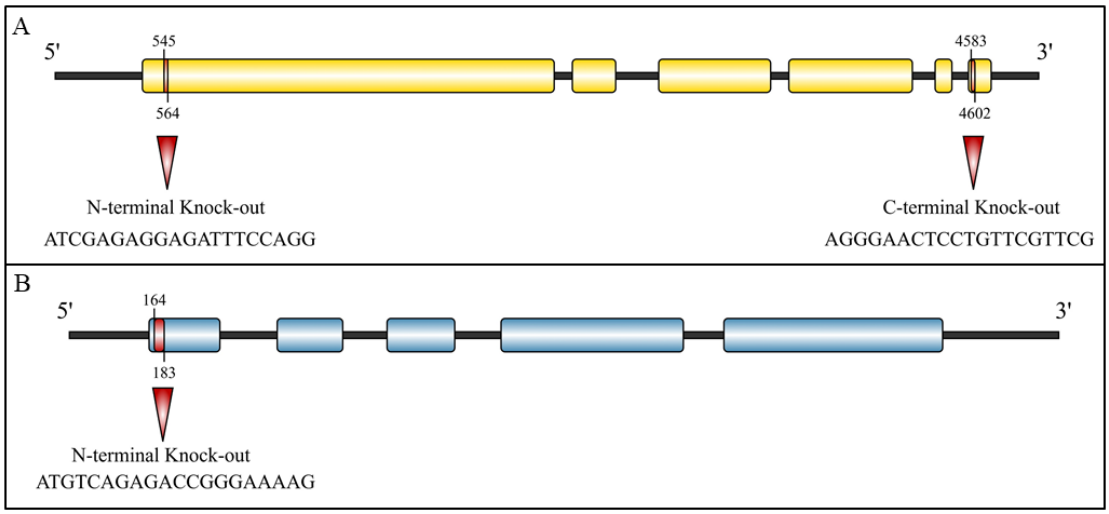

Fig. 20: Schematic representation of CRISPR/Cas9 target sites used for generation of parental knockout lines.

A *STI* target sites used for generation of the parental lines HY115 and HY117. Two independent sgRNAs targeting the N-terminal (HY115) and C-terminal (HY117) coding regions were designed to induce loss-of-function alleles. B *NOK* target site used for generation of the parental line HY116. Exons are represented as coloured boxes. Red arrowheads indicate CRISPR/Cas9 target sites, and the corresponding target sequences are shown below each construct. Numbers indicate genomic positions of the target regions within the respective loci. Created in IBS.

All T1 lines were confirmed via genotyping PCR. Lines HY115 and HY116 displayed phenotypes consistent with loss-of-function mutations in the respective target genes (Fig. 21). These phenotypes confirm the functionality of the CRISPR/Cas9 system in the newly generated parental lines. In contrast, HY117 did not exhibit an obvious phenotype, likely due to targeting within the terminal exon (Fig. 20), which may not fully disrupt protein function.

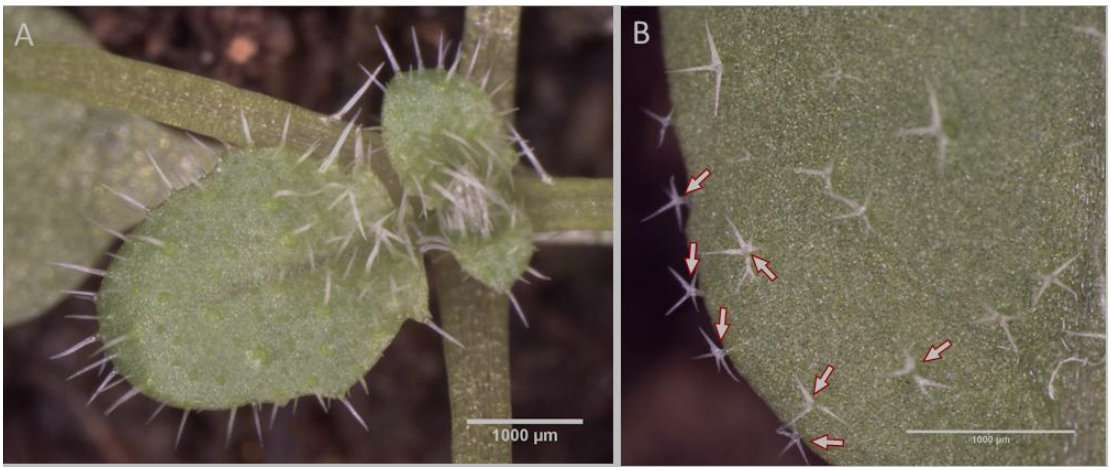

Fig. 21: Phenotypic characterization of CRISPR/Cas9-generated knockout lines.

Representative leaf images of independent CRISPR/Cas9 knockout lines targeting trichome branching genes are shown. (A) Line HY115 targeting *STI* exhibits no trichome branching, resembling the typical *sti* mutant. (B) Line HY116 targeting *NOK* displays increased trichome branching, resembling the typical *nok* mutant. Line HY117 did not display any obvious phenotype (not shown).

4.4.2.1 Transformation of parental lines with a modified HDR construct

To complement the newly generated parental lines, they were subsequently transformed with the established *STI* N-terminal and C-terminal tdTomato HDR constructs HY098 and HY100. In addition, several modified HDR donor constructs were designed to further optimize knock-in efficiency, selection strategies, and downstream functional analyses. The following section summarizes the individual construct modifications and their rationale. For an overview of the selection workflow and the structure of the parental line construct and the HDR construct see Fig. 22.

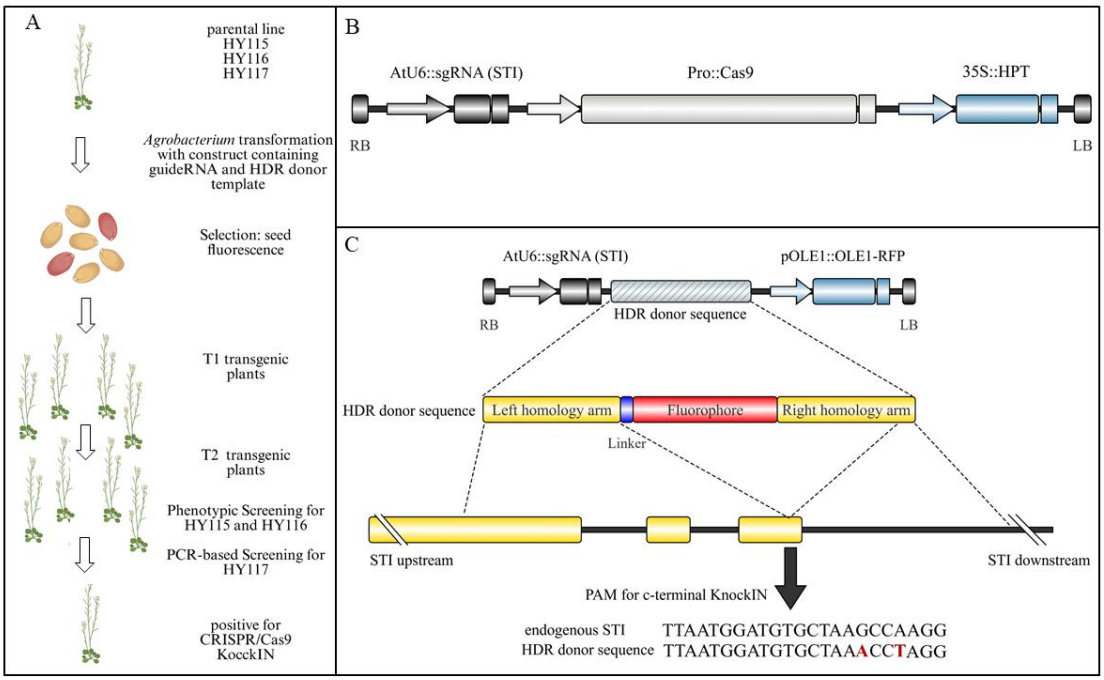

Fig. 22: Strategy for CRISPR/Cas9-mediated HDR knock-in in *A. thaliana* using parental lines generated in this study.

A: Schematic overview of the workflow. A parental *A. thaliana* line expressing Cas9 under control of the DD45 promoter was transformed via *Agrobacterium* with a construct containing a guide RNA (targeting *STI*) and an HDR donor template. Transgenic seeds were identified by seed fluorescence. After propagation of T1 and T2 generations, phenotypic screening and PCR-based screening for positive knock-in events will take place. B: Structure of the parental *Cas9* construct containing an AtU6-driven sgRNA cassette, Cas9 expression cassette, and the hygromycin resistance marker (35S*::HPT*). C: Structure of the HDR donor construct used for *STI* C-terminal fluorophore knock-in. The construct contains an AtU6-driven sgRNA targeting *STI*, the HDR donor sequence consisting of left and right homology arms flanking a linker and the mNeonGreen sequence, and the seed fluorescence selection cassette *pOLE1::OLE1-RFP*. The lower panel illustrates the targeted *STI* genomic locus and the position of the C-terminal knock-in. Silent nucleotide substitutions were introduced into the donor sequence in the protospacer region to prevent Cas9-mediated re-cutting after homologous recombination. Adapted from (D. Miki et al., 2018). Figure created in BioRender and IBS.

Knock-in constructs were cloned based on the vector backbones HY114 (pEC1.2_pEC1.1 spCas9_TagRFP) and HY120 (pEC1.2_pEC1.1 Cas9i_TagRFP). In the vector backbones, the Cas9 cassette was replaced by the respective HDR repair template. Instead of tdTomato, the green fluorescent protein mNeonGreen was selected due to its high fluorescence intensity and suitability for fluorescence imaging and FRET-based applications in plant systems (Denay et al., 2019; Seitz & Krysan, 2020). In addition, cloning and sequencing of constructs containing mNeonGreen proved to be more accessible, most likely because it is smaller in size (674 bp versus 1431 bp) and does not contain any repetitive sequences as tdTomato is a tandem dimer,

mNeonGreen is a monomer. The STOP Codon of the mNeonGreen CDS was deleted for N-terminal insertion.

Furthermore, a flexible Gly-Ser linker $(GGGGS)_2$ was introduced between the protein domains. Glycine-serine repeat linkers are commonly used as flexible spacers in fusion proteins due to their conformational flexibility and low interference with protein folding and function (X. Chen et al., 2013; van Rosmalen et al., 2017). All coding sequences were codon-optimized for expression in *A. thaliana* and synthesized at Genewiz Gene Synthesis. Constructs for both N-terminal and C-terminal tagging of *STI* with mNeonGreen (Tab. 14) were generated and introduced into the respective parental lines via floral dipping. The *STI*-targeting parental line HY115 was transformed with HY098 and HY198, while HY117 was transformed with HY100, HY199, and HY201. The *NOK*-targeting parental line HY116 was transformed with the complete set of available HDR donor constructs. In subsequent generations, candidate lines will be screened phenotypically and genotypically. In HY115-derived lines, successful *STI* knock-in events may be indicated by restoration of trichome branching. In HY116-derived lines, knock-in events may allow analysis of STI localization in a *nok* mutant background and potentially reveal *sti nok* double-mutant phenotypes. Since HY117 does not display an obvious phenotype, PCR-based screening represents the most appropriate strategy to identify successful knock-in events.

4.5 Generation of a stable STI-tdTomato reporter line by random T-DNA integration

In parallel to the HDR-based knock-in strategy, conventional transformation lines were generated to enable rapid assessment of protein localization and to evaluate functional complementation independently of endogenous locus targeting efficiency. To generate a fluorescently tagged STI reporter line, the donor vector LS658 was modified by PCR-mediated site-directed mutagenesis to remove a pre-existing STOP codon, thereby enabling translational fusion of STI with tdTomato under the constitutive 35S promoter. The resulting construct was introduced into *A. thaliana* Col-0 and the *sti146* mutant background via *Agrobacterium*-mediated floral dipping (Clough & Bent, 1998). As this approach relies on T-DNA integration, insertion of the construct occurred randomly within the genome.

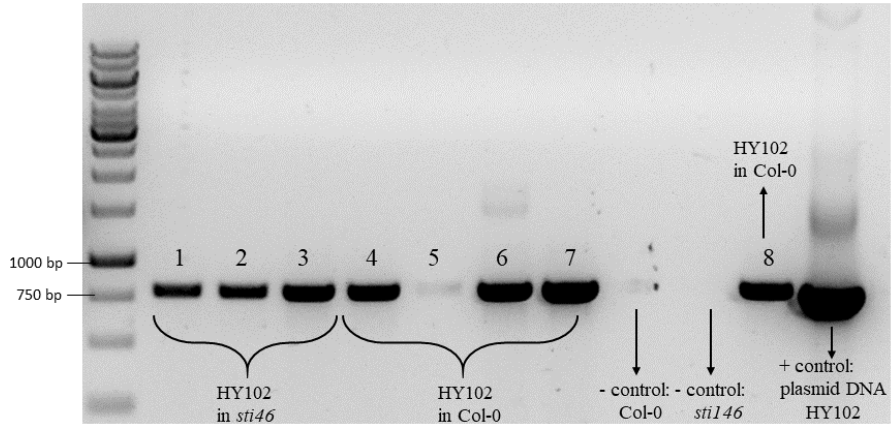

Fig. 23: Gel electrophoresis of genotyping PCR of HY102 T1 plants.

Magic buffer extractions of 3 plants with *sti* mutant background and 5 plants in the Col-0 background were tested. Primers L708 and HJ060 confirmed insertion of the transgene, shown as bands at the expected size of 871 bp. The GeneRuler 1 kb DNA ladder was used.

Transgenic seedlings were selected on hygromycin-containing MS Medium and subsequently transferred to soil. To confirm integration of the transgene, hygromycin-resistant T1 seedlings were subjected to genotyping PCR (Fig. 23). PCR amplification using construct-specific primers HJ060 and L708 verified the presence of the STI-tdTomato insertion in a subset of transformants. Genotyped positive lines were subsequently transferred to soil and propagated to the next generation (T2) for further phenotypic and fluorescence-based analyses.

Plants of the T1 generation already displayed altered trichome phenotypes (Fig. 24). The construct rescued the *sti* mutant and restored branched trichomes, indicating a functional protein. In contrast, phenotypic effects in the Col-0 background were less immediately apparent during initial screening. However, careful inspection suggested a tendency toward increased trichome branching in some lines. This observation was therefore analysed in more detail in Fig. 25, as STI activity is known to be dosage-dependent (Ilgenfritz et al., 2003). Genotyped positive lines were propagated to the next generation (T2) for further phenotypic and fluorescence-based analyses.

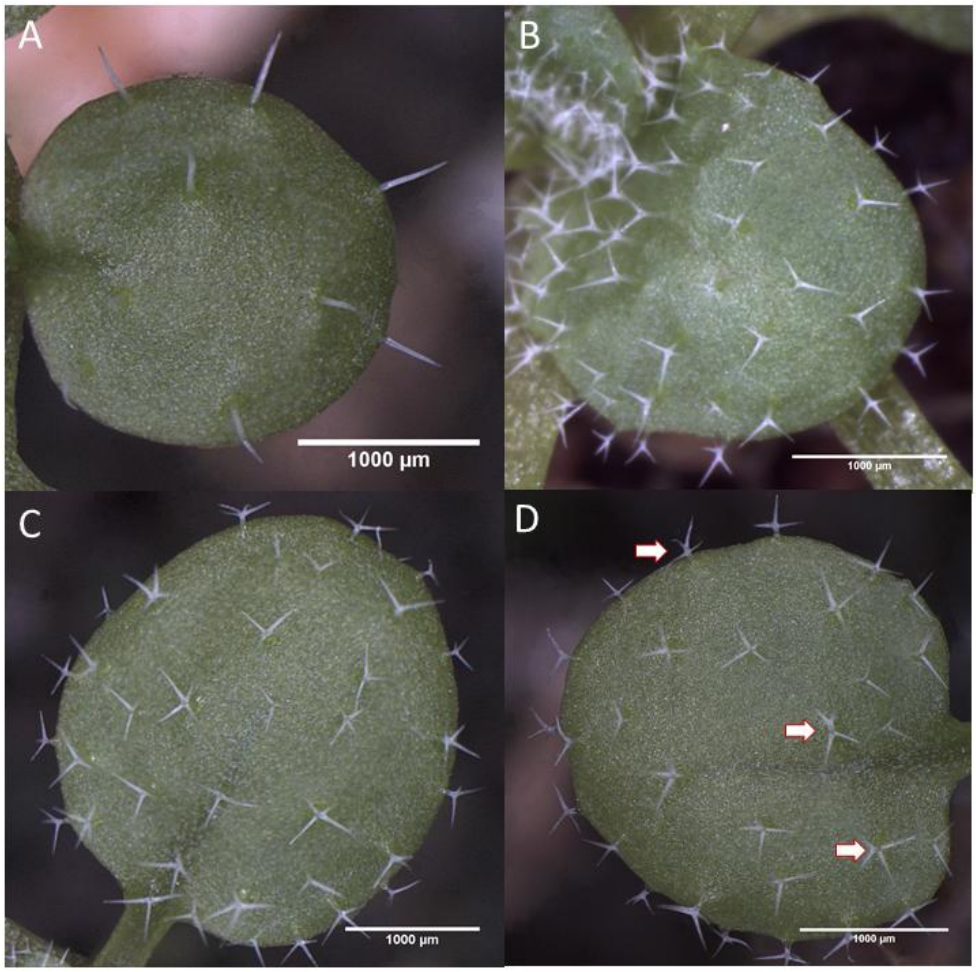

Fig. 24: HY102 expression affects trichome branching in sti146 and Col-0 backgrounds.

A: sti146 mutant showed no trichome branching. B: Expression of HY102 in the sti146 background restores trichome branching. C: Col-0 with wild type trichomes with mostly 3 branches. D: Expression of HY102 in the Col-0 background. Overbranched trichomes are indicated with errors. Scale bars: 1000 µm.

To quantify the effect of HY102 expression on trichome branching, the number of branches per trichome was determined across different genetic backgrounds. Analysis of individual trichomes revealed clear differences in branch number distributions between genotypes (Fig. 25). The third and fourth leave of approximately 14-day old plants were investigated.

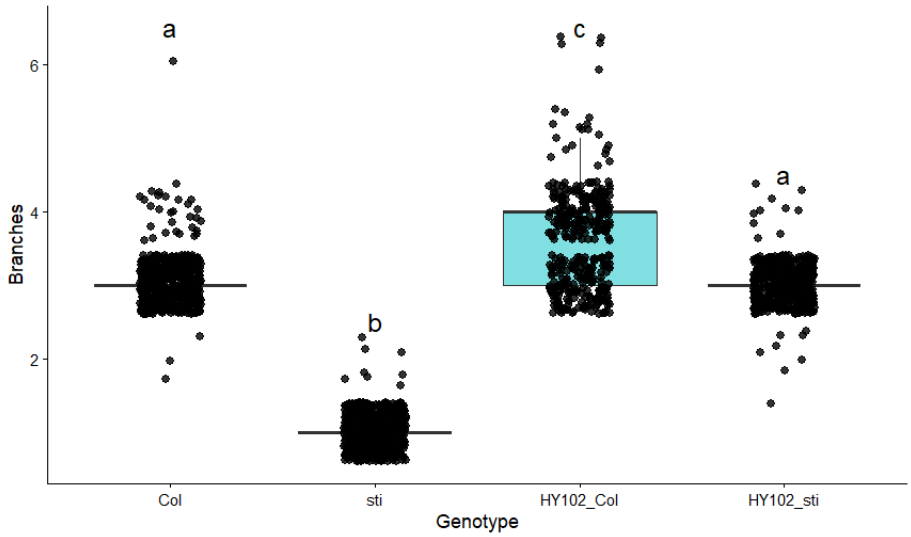

Fig. 25: Quantification of trichome branch number in HY102 in different genetic backgrounds.

Each point represents an individual trichome. Boxplots are shown where visible and indicate the interquartile range with the median. Different letters denote statistically significant differences between groups as determined by Dunn's test with Holm correction ($p < 0.05$). A Kruskal-Wallis test revealed a significant effect of genotype on branch number ($\chi^2 = 1744.80$, $df = 3$, $p < 0.001$). The sti146 mutant exhibits strongly reduced branching, whereas expression of HY102 restores branch number to wild-type levels in the mutant background and increases branching in the Col-0 background.

A Kruskal-Wallis test showed a highly significant effect of genotype on trichome branch number ($\chi^2 = 1744.80$, $df = 3$, $p < 0.001$).

Consistent with its established phenotype, the *sti146* mutant displayed a strongly reduced number of branches compared to Col-0 (Dunn's test with Holm correction: $p < 0.001$), with the majority of trichomes exhibiting only a single branch.

Expression of HY102 in the *sti146* background resulted in a highly significant increase in branch number compared to *sti146* ($p < 0.001$). Importantly, no significant difference was detected between HY102 in the *sti146* background and Col-0 ($p = 0.175$), indicating that branch number was restored to wild-type levels.

In the Col-0 background, expression of HY102 led to a significant increase in branch number compared to Col-0 ($p < 0.001$). Furthermore, HY102 in Col-0 differed significantly from HY102 in the *sti146* background ($p < 0.001$), indicating that the effect of HY102 depends on the genetic context and further supports the hypothesis that STI acts in a dosage-dependent manner (Ilgenfritz et al., 2003).

Taken together, these results demonstrate that HY102 expression is sufficient to restore trichome branching in the *sti146* mutant, indicating functional complementation. Col-0 plants expressing STI-tdTomato displayed increased trichome branching compared to wild type, suggesting that altered STI dosage affects branching behaviour. Having established that the STI-tdTomato fusion protein was functionally active and influenced trichome morphology, the next step was to examine whether the fusion construct also produced detectable fluorescent signals *in planta*.

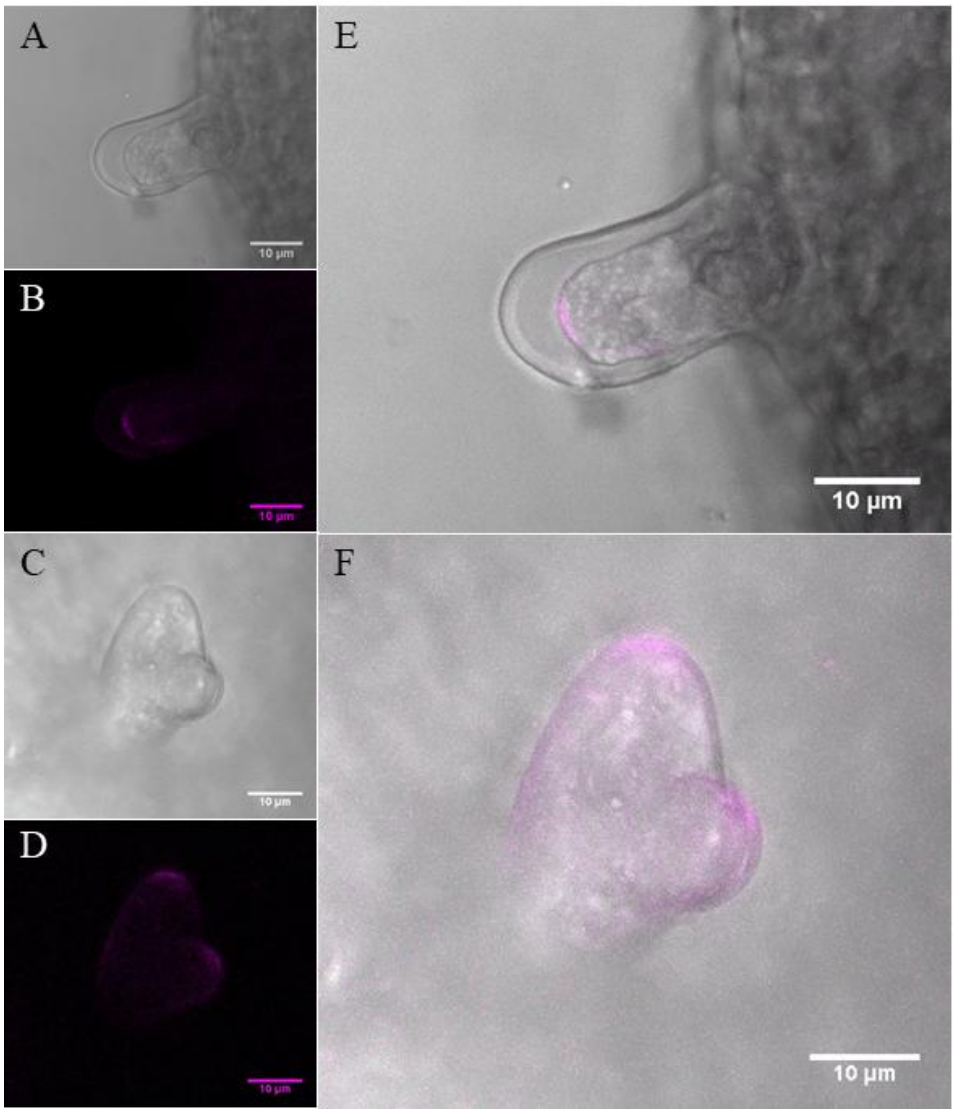

Fig. 26: Confocal images of developing *Arabidopsis* trichomes expressing HY102.

Brightfield images are shown for the *sti* mutant background A and the Col-0 background C. Corresponding fluorescence images are shown in B and D, respectively, while merged representations are displayed in E and F. In both genetic backgrounds, STI-tdTomato accumulated in a distinct cap-like structure at sites of future branch initiation, confirming localization of STI at developing branch formation. Scale bars = 10 µm.

In the following generation (T2), plants were thus selected based on their trichome phenotype and further analysed by 3.6.2 Confocal laser scanning microscopy. A clear tdTomato signal in trichomes was revealed, confirming expression and stability of the fusion protein (Fig. 26).In the merged image (Fig. 26E), STI-tdTomato fluorescence was enriched at the cortical region of the developing branch site. Although no plasmolysis assay was performed in this study, the observed localization pattern is consistent with previously reported plasma membrane-associated localization after plasmolysis(Huang, 2008).

Taken together, these results demonstrate that a stable STI-tdTomato reporter line was successfully established, providing a functional tool for subsequent analyses.

4.6 STI interacts with distinct C-terminal regions of NET1 proteins

A large-scale yeast two-hybrid assay revealed NET1A, NET1C and NET1D to interact with STI fragments among a larger library of possible interactors (Huang, 2008). Given that NET1 is closely related to actin organization and has a defined actin-binding (NAB) domain (Deeks et al., 2012), this study focused on a) confirming the interaction of NET1 and STI in a separate experiment and b) to identify the regions of NET1 proteins mediating interaction with STI.

4.6.1 Identification of NET1 proteins as interaction partners of STI

To test the first hypothesis, yeast two-hybrid assays were performed using full-length STI as well as its subfragments (STI S1, S2, and S3) in combination with full-length NET1 proteins, the isolated N-terminal NAB domain, the complete C-terminal region lacking the NAB domain (full cterm), and subdivided C-terminal regions (cterm 1 - 3). The amino acid ranges of all analysed fragments are listed in Tab. 16. Note that the C-terminal 3 fragment as well as the full C-terminal fragment of NET1A contains an intron of 170 bp. Furthermore, fragment NET1D C-terminal full length was excluded from the analysis because repeated cloning attempts were unsuccessful.

NET1A interaction is mediated predominantly by cterm3

For NET1A, interaction with STI was primarily mediated by the third C-terminal subfragment (cterm3). This fragment showed consistent and robust interaction with STI constructs, including full-length STI as well as STI S2 and STI S3, and in some configurations also STI S1. In several cases, the interaction persisted under increased selection stringency.

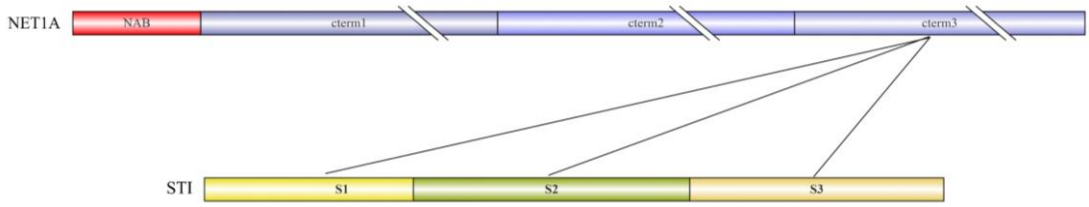

Fig. 27: Schematic overview of NET1A and STI fragments identified by yeast two-hybrid analysis.

NET1A was subdivided into the isolated N-terminal NAB domain and three C-terminal subfragments (cterm1-3). STI was analysed as full-length protein and as subfragments S1-S3. Full-length proteins and the complete NET1A C-terminal region lacking the NAB domain ("full cterm") were additionally tested but are not shown schematically. Observed interactions are summarized in Tab. 15.

In addition, the full C-terminal region also displayed interaction with STI, suggesting that cterm3 represents the core interaction region within this larger fragment. Other NET1A subfragments did not show consistent interaction. Interactions involving NET1A were partially orientation-dependent, with some combinations showing growth only in one bait-prey configuration (Fig. 44 to Fig. 47).

NET1B interacts via its second C-terminal subfragment (cterm2)

For NET1B, interaction with STI was restricted to the second C-terminal subfragment (cterm2). Growth was observed for STI S1 × NET1B cterm2 under increased selection stringency. Full-length NET1B also showed interaction with STI S1, however, this interaction could be attributed to the presence of the cterm2 region.

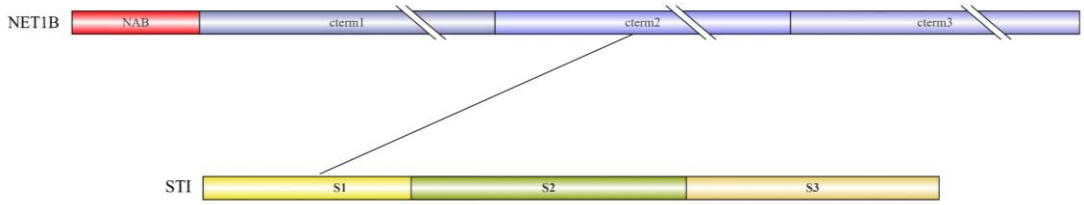

Fig. 28: Schematic overview of NET1B and STI fragments identified by yeast two-hybrid analysis.

NET1B was subdivided into the isolated N-terminal NAB domain and three C-terminal subfragments (cterm1-3). STI was analysed as full-length protein and as subfragments S1-S3. Full-length proteins and the complete NET1B C-terminal region lacking the NAB domain ("full cterm") were additionally tested but are not shown schematically. Observed interactions are summarized in Tab. 15.

No interaction was detected for the NAB domain or the remaining C-terminal subfragments. Interaction between NET1B cterm2 and STI was only observed when NET1B cterm2 was expressed as prey and STI S1 as bait, whereas the reciprocal bait-prey configuration did not result in growth under selective conditions (Fig. 53 to Fig. 57).

NET1C interaction is mediated predominantly by cterm3

For NET1C, interaction-dependent growth under stringent selection conditions was observed predominantly for NET1C cterm3. This fragment showed strong interaction with STI S1 in both vector orientations. In addition, NET1C cterm3 interacted with full-length STI.

NET1C cterm1 displayed weaker but reproducible interaction with STI S1. In contrast, no interaction was detected for the isolated NAB domain. NET1C cterm2 showed growth in combination with empty vector controls, indicating autoactivation in one vector orientation. Therefore, interaction signals observed in this orientation were not considered specific. In the reciprocal vector orientation, no interaction-dependent growth with STI constructs was detected under stringent conditions.

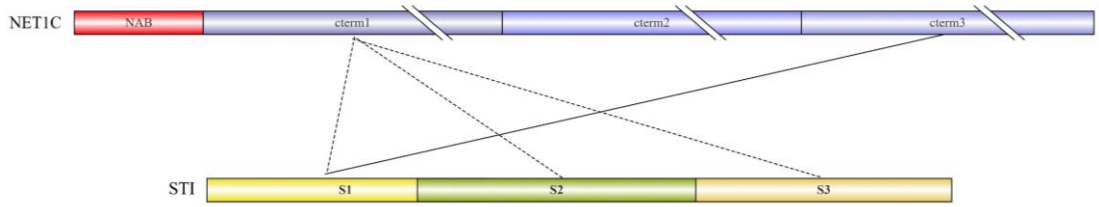

Fig. 29: Schematic overview of NET1C and STI fragments identified by yeast two-hybrid analysis.

NET1C was subdivided into the isolated N-terminal NAB domain and three C-terminal subfragments (cterm1-3). STI was analysed as full-length protein and as subfragments S1-S3. Solid lines indicate prominent reproducible interaction between NET1C cterm3 and STI S1 in both vector orientations. NET1C cterm1 displayed weaker interaction with STI S1. Interactions involving NET1C cterm2 were excluded from interpretation due to autoactivation observed with empty vector controls. Dashed lines indicate weaker interactions detected only in single vector orientations. Full-length proteins and the complete NET1C C-terminal region lacking the NAB domain ("full cterm") were additionally tested but are not shown schematically. Observed interactions are summarized in Tab. 15.

Together, these findings indicate that interaction between NET1C and STI is primarily mediated through defined regions within the extended C-terminus, particularly cterm3.

NET1D interacts predominantly via cterm3

For NET1D, interaction with STI was confined to the third C-terminal subfragment (cterm3). This fragment showed strong and reproducible interaction with full-length STI as well as STI subfragments, STI S1, S2 and S3.

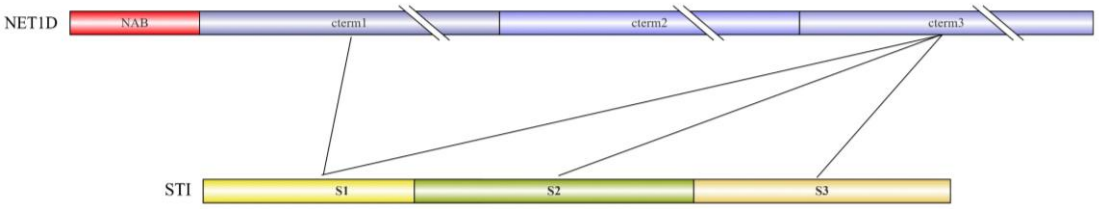

Fig. 30: Schematic overview of NET1D and STI fragments identified by yeast two-hybrid analysis.

NET1D was subdivided into the isolated N-terminal NAB domain and three C-terminal subfragments (cterm1-3). STI was analysed as full-length protein and as subfragments S1-S3. Full-length proteins were additionally tested but are not shown schematically. A NET1D full cterm construct could not be analysed due to unsuccessful cloning. Observed interactions are summarized in Tab. 15.

The interaction between full-length STI and NET1D cterm3 was particularly strong, with growth observed across all selective conditions. In addition, weaker interaction was observed between NET1D cterm1 and STI S1. Reciprocal combinations and interactions involving the

remaining NET1D subfragments were either negative or substantially weaker, further supporting cterm3 as the primary interaction region mediating STI binding (Fig. 50 to Fig. 52).

4.6.2 Summary of Y2H interactions between STI and NET1 proteins

Across all tested combinations, no interaction was detected for any of the NAB domains, indicating that STI binding is not mediated by the conserved N-terminal region of NET1 proteins. Instead, interactions were consistently observed within the C-terminal regions, in most cases via the third C-terminal part.

Tab. 15: Yeast two-hybrid interaction of STI fragments and NET1 fragments.
- negative result + growth on -LWH 5 mM 3AT ++ growth on -LWH 25 mM 3AT. Red marked interactions have been confirmed in three independent experiments. NET1D cterm2 was excluded from the analysis due to autoactivation (Fig. 57).

Bait/Prey	STI full length	STI S1	STI S2	STI S3
NET1 A full length	-	+	-	-
NET1 A NAB	-	-	-	-
NET1A cterm full length	++	++	-	++
NET1A cterm1	-	+	-	-
NET1A cterm2	+	-	-	-
NET1 A cterm3	++	+	++	++
NET1B full length	-	+	-	-
NET1B NAB	-	-	-	-
NET1B cterm full length	++	-	-	-
NET1B cterm1	-	-	-	-
NET1B cterm2	+	++	-	-
NET1B cterm3	-	-	-	-
NET1C full length	++	++	-	-
NET1C NAB	-	-	-	-
NET1C cterm full length	++	++	+	++
NET1C cterm1	+	+	+	+
NET1C cterm2	n.a.	n.a.	n.a.	n.a.
NET1C cterm3	++	++	-	+
NET1D full length	-	-	-	-
NET1D NAB	-	-	-	-
NET1D cterm1	-	+	-	-
NET1D cterm2	-	-	-	-

Bait/Prey	STI full length	STI S1	STI S2	STI S3
NET1D cterm3	++	++	+	+

4.6.3 Sequence analysis of interacting NET1 fragments reveals partial conservation within charged C-terminal regions

To further compare the interacting NET1 fragments, a multiple sequence alignment was performed using the C-terminal fragments NET1A cterm3, NET1C cterm3 and NET1D cterm3, which consistently showed interaction with STI in the yeast two-hybrid assays. NET1B cterm2 was excluded from the analysis, as interaction with STI was only observed in a single vector orientation.

The alignment revealed regions of moderate sequence conservation, particularly within the central part of the analysed fragments. Conserved residues were predominantly enriched in charged amino acids, including lysine, arginine, glutamate and aspartate residues, whereas extended hydrophobic stretches were largely absent (Fig. 31). Additional motif discovery analysis using MEME (Bailey & Elkan, 1994) identified several short locally conserved sequence motifs shared among the analysed fragments. However, no single extended highly conserved linear motif spanning the complete interacting regions could be defined.

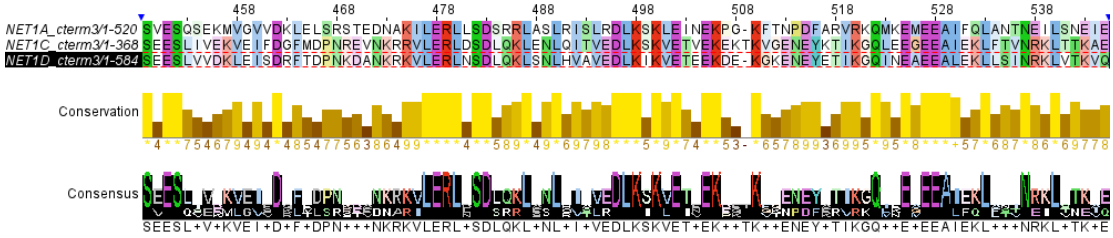

Fig. 31: Multiple sequence alignment of STI-interacting NET1 C-terminal fragments.

Alignment of NET1A cterm3, NET1C cterm3 and NET1D cterm3 generated using MAFFT (Katoh & Standley, 2013) and visualized in Jalview (Waterhouse et al., 2009). The displayed region represents the most conserved part of the alignment. Conserved residues are highlighted according to sequence similarity, and relative conservation across the alignment is indicated below the sequences. Several short locally conserved sequence motifs identified by MEME (Bailey & Elkan, 1994) analysis overlap with the displayed conserved regions.

Together, these observations suggest that STI interaction with NET1 proteins may depend on a combination of short conserved sequence elements and broader physicochemical properties of the charged C-terminal regions, rather than on a single highly conserved interaction motif. A complete alignment of the analysed NET1 fragments is provided in Fig. 59.

5 Discussion

5.1 STI contains conserved ATPase-related features but lacks experimental validation of catalytic activity

Although STI has long been recognized as an important regulator of trichome morphogenesis in *A. thaliana* (Ilgenfritz et al., 2003), its molecular function has remained unresolved. Earlier analyses suggested similarity between the central region of STI and ATPase-associated clamp loader proteins, including the γ subunit of bacterial DNA polymerase III and replication factor C (RFC)-like ATPases (Ilgenfritz et al., 2003). However, the limited bioinformatic resources available at the time did not allow a more detailed structural classification of the protein.

The rapid development of modern bioinformatic and deep learning-based prediction tools has substantially improved the ability to analyse previously uncharacterized proteins. In particular, structure prediction approaches such as AlphaFold now permit high-confidence modelling even in the absence of experimental structural data (Jumper et al., 2021; Varadi et al., 2022). Re-evaluation of STI using current computational approaches consistently supported the presence of a central ATPase-related region containing conserved sequence features characteristic of the AAA^+/P-loop NTPase superfamily, including Walker A- and Walker B-like motifs (Leipe et al., 2002; Walker et al., 1982). The predicted ATPase-associated region further showed similarity to clamp loader and initiator-type ATPases, including RFC- and DnaA-related proteins of the ASCE/AAA^+ lineage (Erzberger & Berger, 2006; Leipe et al., 2002). Together with the observed similarity to clamp loader-associated ATPases, these findings suggest that STI contains an evolutionarily conserved ATPase-like core domain.

5.1.1 Structural organization of STI suggests regulatory or assembly-related functions

At the same time, the computational analyses also indicate that STI differs substantially from canonical AAA^+ ATPases. Rather than forming a uniformly structured ATPase module, the predicted protein architecture consists of a compact central core flanked by extended terminal regions with low structural confidence (Fig. 11). According to the AlphaFold confidence metrics, such low-confidence regions frequently correlate with conformational flexibility or intrinsic disorder rather than failed prediction alone (Jumper et al., 2021; Varadi et al., 2022). Such regions are frequently associated with intrinsic disorder or conformational flexibility and

often function as flexible interaction platforms or dynamic linkers in regulatory proteins (Wright & Dyson, 2015). Furthermore, relative orientations between the predicted central core and terminal regions should be interpreted cautiously, as AlphaFold confidence estimates decrease substantially in flexible multidomain regions (Varadi et al., 2022).

Another notable observation was the identification of a distinct C-terminal α/β domain with similarity to DnaA_N-like folds. Although the functional relevance of this region remains unclear, DnaA-related domains are commonly associated with protein interaction and oligomerization functions in bacterial systems (Duderstadt et al., 2010; Erzberger & Berger, 2006). In DnaA, coordinated interactions between ATPase-associated regions and additional regulatory domains contribute to ATP-dependent conformational switching and assembly dynamics required for origin opening (Duderstadt et al., 2010). Although no comparable mechanism can currently be inferred for STI, the presence of a predicted DnaA_N-like region further supports the idea that STI may function as a multidomain regulatory protein rather than a simple soluble ATPase enzyme. The identification of this additional domain further motivated the generation of an extended ATPase construct for subsequent biochemical analyses.

This organization may therefore reflect a multidomain protein architecture in which the ATPase-like region functions in combination with flexible regulatory domains. In the context of trichome morphogenesis, such an arrangement could be compatible with a role in transient protein interactions, dynamic assembly processes, or spatial organization of cellular components rather than classical enzymatic ATP turnover.

Importantly, AlphaFold predictions currently provide only monomeric structural models and therefore do not allow reliable conclusions regarding possible higher-order assembly states of STI. In addition, AlphaFold models represent static structural predictions and therefore cannot directly resolve dynamic conformational transitions or ATP-dependent assembly processes.

5.1.2 ATPase-like motifs do not necessarily imply canonical ATPase activity

Members of the broader P-loop NTPase superfamily fulfil highly diverse structural and regulatory functions, and conservation of ATPase-like folds does not necessarily correlate with catalytic activity (Erzberger & Berger, 2006; Leipe et al., 2002). Leipe et al. further distinguish multiple evolutionary lineages within the P-loop NTPase superfamily, including classical AAA^+ ATPases as well as structurally related ATPase groups with distinct functional properties

(Leipe et al., 2002). Consequently, the ATPase-like features identified in STI do not necessarily imply a canonical AAA^+ ATPase function.

In some ATPase-associated proteins, ATP binding rather than ATP hydrolysis represents the biologically relevant property, whereas others retain ATPase-associated structural elements despite functional divergence (Duderstadt et al., 2010). In AAA^+/initiator systems such as DnaA, ATP binding can promote conformational transitions and higher-order assembly states independently of measurable ATP turnover (Duderstadt et al., 2010). This distinction is particularly relevant for STI, as no experimental evidence for ATP hydrolysis or ATP-dependent assembly could be obtained in the present study.

Furthermore, many AAA^+ ATPases function as multimeric assemblies, and ATP-dependent oligomerization represents a central mechanistic feature of many initiator- and clamp loader-like ATPases (Duderstadt et al., 2010). It is therefore conceivable that STI may require interaction with additional plant-specific cofactors or related proteins to form functional higher-order assemblies that cannot be reconstituted using isolated recombinant fragments *in vitro*.

Overall, the *in silico* analyses substantially refine the current structural model of STI and support the presence of a conserved ATPase-like core region within a larger multidomain protein. However, computational predictions alone remain insufficient to infer biochemical activity, and experimental validation was therefore required to determine whether the predicted ATPase-like region of STI corresponds to a catalytically active domain or instead fulfils structural or regulatory functions during trichome development.

5.2 Absence of detectable ATPase activity suggests a non-canonical role of STI

Despite structural similarity of the central STI region to ATPase-associated proteins, no detectable ATP hydrolysis activity could be observed for the analysed STI fragments in two independent *in vitro* assay systems. These findings argue against STI functioning as a classical highly active ATPase under the tested conditions.

However, the negative biochemical results should be interpreted cautiously. The biochemical analyses were performed using STI-derived fragments rather than the full-length protein. Biochemical and structural studies of AAA^+ and ATPase-associated proteins frequently focus on isolated ATPase-containing domains, particularly in the case of large multidomain proteins

that are difficult to express and purify in full-length form (Erzberger & Berger, 2006; Khan et al., 2022). Nevertheless, catalytic activity of many ATPase-associated proteins can depend on oligomerization, conformational rearrangements, cofactors, membranes, or interaction partners for full activity (Erzberger & Berger, 2006). Such requirements may not be reproduced in recombinant *in vitro* systems.

The absence of detectable ATPase activity is consistent with the sequence and structural analyses presented in this study, which identified ATPase-associated similarity but did not reveal fully conserved canonical ATPase motifs. Together, the available data support the hypothesis that STI may primarily fulfil structural or regulatory functions mediated through protein-protein interactions rather than acting as a highly active ATP-hydrolysing enzyme.

5.2.1 Genetic and interaction data support a dosage- or assembly-dependent function

STI was reported to interact with itself and with the related protein STI-hom in Y2H and BiFC assays, suggesting that STI may participate in higher-order protein assemblies or self-associated complexes (Huang, 2008). The STI homologue analysed likely corresponds to AT1G14460, which was identified by Ilgenfritz et al., 2003 as one of the closest STI-related proteins in *Arabidopsis*.

A previous study reported that a mutation in the predicted ATPase binding motif failed to rescue the *sti* mutant phenotype, while the corresponding mutant protein still retained interaction with STI and STI-hom in Y2H and BiFC assays (Huang, 2008). It must be noted that a misidentification of the ATP hydrolysis motif led to the transformation of a construct that had the intact motif and a K619A mutation, which was also not able to rescue the *sti* mutant phenotype in the same study. The *STI* wild type construct only rescued the phenotype in half of the cases (Huang, 2008). Additional transformation experiments using different *STI* expression constructs yielded partially inconsistent trichome branching phenotypes (Dr. Swen Schellmann, personal communication). Although some lines displayed altered branching behaviour suggestive of dosage-dependent or dominant-negative effects, the observed phenotypes were not sufficiently robust to allow clear mechanistic conclusions. The variability of these *in planta* observations additionally motivated the biochemical and structural approaches pursued in the present study to investigate the proposed ATPase-associated properties of STI under more controlled experimental conditions. This interpretation is further supported by the

overbranching phenotype observed upon constitutive expression of STI-tdTomato in the Col-0 background in the present study (Fig. 25), indicating that altered STI dosage can influence trichome branch number and supporting a dosage-dependent or interaction-based mode of STI function.

5.2.2 STI may function through regulatory protein interactions during branch initiation

Previous interaction studies further demonstrated direct association between the STI N-terminus and the branch initiation regulator BLT (Xi et al., 2018). Together with the absence of obvious endoreduplication defects in *sti* mutants, these observations led the authors to propose that STI may function predominantly through regulatory protein interactions during trichome morphogenesis rather than through classical replication-associated ATPase activity. Consistent with this interpretation, heterologous expression studies in cotton fibres demonstrated that elevated endoreduplication alone was insufficient to induce branching (Wang et al., 2013). Fibre branching could only be induced by combined expression of *BLT*, *SIM*, and *Arabidopsis STI*, supporting a specific role of *STI* in branch initiation rather than general regulation of DNA content or cell growth (Wang et al., 2013).

Introduction of defined endogenous point mutations by CRISPR/Cas9-mediated genome editing under native expression conditions may therefore provide a more suitable strategy to assess the functional relevance of the predicted ATPase-associated region.

More generally, the performed *in vitro* experiments remain limited in their ability to reproduce the physiological environment of plant cells, where protein activity may depend on cellular context, developmental regulation, or interaction partners. To address these limitations, endogenous fluorescent STI reporter lines and CRISPR/Cas9-based genome editing strategies were established in this study as a foundation for future *in planta* analyses of STI localization and function.

5.3 Establishment of CRISPR/Cas9-based endogenous STI reporter lines

The generation of endogenous fluorescent STI reporter lines was motivated by the limitations of the previously available constitutive 35S*::*GFP-STI reporter system. While constitutive overexpression lines represent useful tools for initial localization studies, they may not accurately reflect native expression levels, developmental regulation, or physiological protein localization. In the case of *STI*, dosage-dependent effects on trichome branching further complicated interpretation of overexpression-based reporter lines. CRISPR/Cas9-mediated endogenous tagging strategies were therefore established to enable future analyses of STI under native regulatory conditions.

5.3.1 Proof of principle for HDR-mediated endogenous *STI* tagging using the DD45 system

HDR-mediated genome editing in plants is generally considered substantially less efficient than non-homologous end joining (NHEJ), which represents the predominant DNA repair pathway in somatic plant cells (T. K. Huang & Puchta, 2019). Consistent with this, only a limited number of candidate knock-in events were recovered in the present study. Nevertheless, PCR- and sequencing-based analyses confirmed that precise integration of the tdTomato sequence at the endogenous *STI* locus was achievable using the DD45 egg-cell-specific Cas9 system, consistent with previous reports demonstrating heritable HDR-mediated genome editing in *Arabidopsis* (D. Miki et al., 2018).

Interestingly, all confirmed knock-in events originated from a single transformation line, further illustrating the generally low frequency and stochastic nature of HDR-mediated genome editing in *Arabidopsis*. Sequencing of PCR-amplified integration products confirmed correct insertion of the fluorophore sequence at the targeted genomic locus. Subsequent backcrossing to Col-0 successfully restored trichome formation in the F1 generation, demonstrating that the glabrous phenotype associated with the original DD45 parental line could be separated genetically from the edited *STI* locus.

Several technical challenges became apparent during construct generation and transformation. The high AT content of the *STI* upstream and downstream regions substantially complicated conventional cloning procedures, ultimately requiring commercial gene synthesis of the HDR

donor fragments. In addition, the knock-in vectors themselves were unusually large (approximately 13500 bp) and contained repetitive as well as AT-rich sequence elements, which complicated plasmid propagation and sequence verification. Full plasmid sequencing was not feasible and constructs therefore had to be verified in fragments, requiring iterative primer design and partial sequencing approaches.

While candidate lines could be recovered for the C-terminal knock-in strategy, no fluorescent transformants were obtained for the N-terminal construct during seed fluorescence screening. This observation suggests that the failure of the N-terminal approach may already have occurred at the level of transformation efficiency, construct stability, or transgene integrity rather than during the HDR process itself. Potential functional interference of the N-terminal fluorophore fusion with STI expression or protein stability also cannot be excluded. Since no transformants could be recovered for this construct, these possibilities could not be distinguished experimentally in the present study.

In addition to PCR-based verification and phenotypic analyses, initial confocal microscopy experiments demonstrated that STI-tdTomato fluorescence can be detected in T1 knock-in plants generated by the CRISPR/Cas9 strategy. Although fluorescence intensity was weak, a reproducible signal could be observed in epidermal outgrowth structures of the GL2 background used for the initial knock-in experiments (Fig. 19). Interestingly, fluorescence appeared enriched at apical cortical regions of these structures, consistent with the localization pattern previously reported for the constitutive GFP-STI reporter line (Herrmann, 2007; Ilgenfritz et al., 2003). In one out of three analysed samples, fluorescence was additionally detected at basal regions of the trichome-like structure (Fig. 41). As this observation was limited to one sample and was obtained in the *gl2* background, its biological relevance remains unclear and requires further analysis in subsequent generations after segregation of the *gl2* background.

Importantly, the analysed cells do not represent fully developed wild-type trichomes, since the initial knock-in experiments were performed in the glabrous *gl2*/Cas9 parental background. Nevertheless, the successful detection of STI-tdTomato under endogenous regulatory control is remarkable, particularly because previous *STI* reporter approaches remained close to the detection limit even under constitutive 35S-driven overexpression conditions. Earlier studies further reported that comparable STI fluorescence signals could not be reproducibly re-established in subsequent years despite extensive attempts using alternative fluorophores, fusion orientations, and expression systems (Herrmann, 2007). The present results therefore

provide an important proof of principle that endogenous STI fluorescence can be visualized using modern confocal microscopy approaches.

At the same time, the low fluorescence intensity highlights the technical challenges associated with endogenous protein tagging in plants. In contrast to constitutive overexpression systems, endogenous STI expression levels are likely substantially lower and may additionally be spatially and temporally restricted. Future analyses in backcrossed lines with restored trichome development will therefore be required to determine whether endogenous STI localization in fully developed trichomes recapitulates the cortical enrichment observed in the present preliminary experiments.

5.3.2 Generation of optimized parental lines for future STI genome editing approaches

To further improve experimental flexibility and establish optimized genetic backgrounds for future knock-in approaches, additional CRISPR/Cas9 parental lines targeting *STI* and *NOK* were generated. In contrast to the previously described *GL2*-based parental system (Mao et al., 2016), these lines directly couple genome editing outcomes to trichome morphogenesis and therefore provide a biologically more relevant background for future *STI* analyses. HY115 and HY116 displayed phenotypes consistent with previously described *sti* and *nok* mutants, confirming functionality of the CRISPR/Cas9 system.

An additional advantage of the newly generated parental lines is that successful HDR-mediated integration events may potentially be linked directly to phenotypic complementation or altered branching phenotypes. This strategy may facilitate identification of edited lines and allow future analyses of STI localization and function in distinct trichome morphogenesis backgrounds. Furthermore, the establishment of independent parental lines targeting different *STI* regions provides increased flexibility for future comparisons between N- and C-terminal fluorescent tagging strategies.

In addition to the redesigned parental lines, the HDR donor constructs were further optimized for future functional studies. The originally used tdTomato fluorophore was replaced by the smaller monomeric fluorophore mNeonGreen, which has been successfully applied in plant imaging approaches (Denay et al., 2019; Seitz & Krysan, 2020). Furthermore, a flexible glycine-serine linker was introduced between *STI* and the fluorescent tag to reduce potential steric interference and improve structural flexibility of the fusion protein (X. Chen et al., 2013;

van Rosmalen et al., 2017). Together, these modifications were intended to improve construct stability and facilitate future localization analyses under endogenous expression conditions.

At the current stage, transformation of the newly generated parental lines with the modified HDR constructs has been completed, but no T1 generation was yet available for detailed analysis. Therefore, the functionality and efficiency of the modified knock-in system remain to be evaluated in future experiments. Nevertheless, the generated parental lines and HDR constructs provide a versatile experimental platform for future *in planta* studies of STI localization, dynamics, and biological function under endogenous regulatory conditions.

5.4 Functional characterization of a T-DNA-based STI-tdTomato reporter line

In parallel to the development of CRISPR/Cas9-mediated endogenous tagging strategies, a conventional T-DNA-based STI reporter line was established to enable rapid functional and localization analyses independently of HDR efficiency. While endogenous tagging approaches provide the advantage of native gene regulation, HDR-mediated genome editing in plants remains technically challenging and comparatively inefficient (T. K. Huang & Puchta, 2019). The rapid establishment of transgenic STI-tdTomato lines therefore represented an important complementary strategy while endogenous reporter systems remain under development.

5.4.1 Functional complementation and dosage-dependent effects of STI-tdTomato

The STI-tdTomato fusion construct fully restored trichome branching in the *sti146* mutant background, demonstrating that the C-terminally tagged fusion protein retained biological functionality despite constitutive overexpression and fluorophore fusion (Fig. 24). This functional complementation is particularly relevant for interpretation of localization studies, as it indicates that the observed fluorescence pattern is associated with a biologically active protein rather than a non-functional reporter construct.

Expression of STI-tdTomato in the Col-0 background additionally resulted in significantly increased trichome branching compared to wild type. (Fig. 23) This observation is consistent with previous reports suggesting dosage-dependent effects of STI on trichome morphogenesis (Ilgenfritz et al., 2003). However, since the construct is expressed under the constitutive 35S

promoter, potential overexpression-related influences cannot be separated from physiological dosage effects. The observed increase in branch number is therefore compatible with dosage-sensitive STI activity, although constitutive overexpression may additionally contribute to the phenotype.

The different phenotypic outcomes observed in the Col-0 and *sti146* backgrounds indicate that increased STI dosage does not uniformly translate into enhanced branching activity. While constitutive *STI* expression promoted overbranching in the Col-0 background, expression in *sti146* primarily restored branch number to near wild-type levels (Fig. 25), suggesting that *STI*-dependent branch formation may become saturated or constrained in the mutant background.

Importantly, the successful complementation by a C-terminal STI-tdTomato fusion demonstrates that C-terminal fluorophore tagging is compatible with STI function and trichome branching activity. The use of tdTomato instead of GFP additionally provides increased experimental flexibility for future co-localization studies. Many established *Arabidopsis* reporter lines, including cytoskeletal markers such as LifeAct-GFP, are GFP-based and therefore difficult to combine with existing GFP-STI constructs due to spectral overlap. The red fluorophore therefore enables future analyses of STI localization in combination with established GFP-based cellular markers. Notably, tdTomato is substantially larger than the subsequently introduced mNeonGreen fluorophore, indicating that STI can tolerate even comparatively large C-terminal fusion tags without complete loss of function.

5.4.2 Subcellular localization of STI-tdTomato during trichome branch initiation

Fluorescence microscopy of the STI-tdTomato reporter line revealed accumulation of the fusion protein at cortical regions of developing trichomes, particularly at sites associated with future branch formation (Fig. 26). This localization pattern is consistent with previous observations reported for GFP-STI, which similarly accumulated at trichome branch initiation sites (Huang, 2008).

The spatially restricted enrichment of STI at developing branch sites is compatible with a role during early stages of branch establishment rather than later phases of branch elongation. The observed localization further supports the hypothesis that STI function is closely associated with spatial regulation of trichome morphogenesis.

However, several limitations must be considered when interpreting these observations. The fluorescence signal was comparatively weak, potentially limiting precise subcellular resolution. In addition, the STI-tdTomato construct is expressed under control of the constitutive 35S promoter, which may alter expression levels and spatial distribution compared to endogenous *STI* expression. Therefore, although the observed localization pattern is consistent with previous findings, its physiological relevance should be interpreted cautiously until confirmed under endogenous expression conditions.

5.5 STI NET1 interactions suggest a role of STI in actin-associated branch initiation

A yeast two-hybrid screen previously identified NET1 proteins among potential interaction partners of STI (Huang, 2008). However, these interactions were not investigated further at the time. The present study independently re-examined the interaction between STI and NET1 proteins and systematically mapped the corresponding interaction regions using defined protein subfragments.

5.5.1 Interaction of STI with distinct NET1 C-terminal regions

Notably, no interaction was detected between STI and the conserved N-terminal NAB domains of NET1 proteins, which mediate actin binding (Deeks et al., 2012). Instead, STI interaction was consistently associated with regions located within the C-terminal parts of NET1 proteins. Since the C-terminal regions of NET1 proteins are thought to contribute to protein-specific interactions and membrane association (Deeks et al., 2012), the observed interaction pattern suggests that STI associates with regulatory or targeting regions of NET1 proteins rather than with the conserved actin-binding machinery itself.

The interaction profiles differed between NET1 paralogs. Whereas NET1A and NET1D interacted predominantly through the cterm3 region. interaction with NET1C was primarily associated with cterm3 and, to a lesser extent, cterm1. By contrast, interaction with NET1B was restricted to cterm2 and was only observed in a single vector orientation. Interestingly, the original large-scale Y2H screen by Huang (2008) identified interactions between STI S1 and NET1A as well as NET1D (consistent with this study), while NET1C was not detected as an interaction partner. NET1B was identified in the original screen with STI S1 and STI S3

fragments, whereas in the present study only an orientation-dependent interaction of S1 and NET1B cterm2 could be confirmed. Together, these observations suggest that STI interaction with NET1 proteins differs between paralogs and may involve distinct interaction surfaces rather than a single conserved interaction mechanism.

This interpretation is supported by the sequence analysis of the interacting regions. Multiple sequence alignment of the robustly interacting NET1 fragments revealed regions of moderate local sequence conservation, particularly enriched in charged residues (Fig. 31). Additional motif discovery analysis using MEME (Bailey & Elkan, 1994) identified several short locally conserved sequence motifs shared among the interacting fragments. However, no single extended highly conserved linear amino acid motif spanning the complete interacting regions could be defined. The aligned C-terminal regions additionally contained several low-complexity sequence stretches while lacking extended hydrophobic regions typically associated with stable globular domains (Wright & Dyson, 2015). Such sequence characteristics are frequently associated with flexible or intrinsically disordered protein regions that mediate transient or multivalent protein-protein interactions (Oldfield & Dunker, 2014; Wright & Dyson, 2015). Although no direct structural disorder analysis was performed in this study, the results suggest that STI interaction may depend on a combination of short conserved sequence elements and broader physicochemical properties of the NET1 C-termini.

Some interactions additionally displayed orientation dependency within the yeast two-hybrid system. Such effects are common in Y2H approaches and may result from steric constraints, altered folding of fusion proteins, or differences in accessibility of interaction surfaces (Sharan et al., 2017). Consequently, absence of interaction in reciprocal bait-prey configurations does not necessarily exclude biological relevance. At the same time, these observations highlight limitations of the Y2H system and indicate that additional interaction studies under physiological conditions will be necessary to further resolve the molecular basis of STI NET1 association.

5.5.2 Functional implications of STI NET1 interactions

NET1 proteins have been described as plant-specific actin-binding proteins that associate with membrane compartments and contribute to the organization of actin-membrane interfaces (Deeks et al., 2012). Their proposed role as actin-membrane linkers makes them plausible

components of processes underlying localized cortical organization and polarized cell growth. Recent studies further demonstrated that members of the NET family can participate in larger cortical interaction networks linking cytoskeletal and membrane-associated structures (Duckney et al., 2025).

The interaction between STI and NET1 proteins is therefore particularly interesting in the context of trichome morphogenesis. Branch initiation in *Arabidopsis* trichomes depends on coordinated cytoskeletal organization and localized cell expansion (Mathur & Chua, 2000; Sambade et al., 2014). Previous studies demonstrated that cortical actin organization and microtubule rearrangements are associated with the establishment of future branch initiation sites and directional branch outgrowth (Sambade et al., 2014). The observed STI NET1 interaction therefore raises the possibility that STI contributes to cytoskeleton-associated organization processes required for localized branch formation. This interpretation is further supported by the localization pattern of STI observed in this study. Fluorescence microscopy revealed enrichment of STI at prospective branch initiation sites (Fig. 26), consistent with a function during early branch establishment rather than later branch elongation. Interestingly, NET1 proteins were previously reported to localize in punctate cortical structures associated with the plasma membrane and cortical actin arrays (Deeks et al., 2012). Although the subcellular localization patterns of STI and NET1 were not analysed simultaneously in the present study, the enrichment of both proteins at cortical regions associated with polarized growth is consistent with the possibility that they act within related spatial organization processes during branch initiation. Together with the interaction data, these observations support a model in which *STI* contributes to the establishment or stabilization of localized cortical growth domains.

Additional support for a role of *STI* in cytoskeleton-associated regulatory processes comes from previously published interaction data. Kasili et al., 2011. report an interaction between STI and the trichome regulator BLT. BLT has been implicated in trichome branch formation and genetically interacts with factors affecting cytoskeletal organization and branch morphogenesis. Although the molecular consequences of the STI-BLT interaction remain unresolved, these findings further support the idea that STI functions within protein networks controlling polarized trichome outgrowth and branch establishment. In addition, proximity-labelling datasets identified STI in association with the catalytic SNF1-related kinase 1 (SnRK1) subunit

KIN10 (Kim et al., 2023). SnRK1 represents a central energy-sensing kinase complex in plants and coordinates metabolic and stress-responsive signalling under conditions of energy limitation. The reported association between STI and KIN10 currently derives from proximity-dependent biotin labelling experiments and therefore does not demonstrate direct physical interaction (Kim et al., 2023). Nevertheless, the observation raises the possibility that STI may participate in larger regulatory protein assemblies that integrate developmental and cellular signalling pathways.

Because STI did not interact with the conserved actin-binding NAB domain (Tab. 15), it appears unlikely that STI directly regulates actin filament binding itself. Instead, STI may function as a scaffold or regulatory factor influencing NET1 protein localization, stability, or interaction dynamics at membrane-associated cortical regions. Such a role would be compatible with the localized accumulation of STI and with the requirement of *STI* for proper branch initiation.

However, the molecular mechanism underlying *STI* function remains unresolved. The present interaction data do not distinguish between direct and indirect association, nor do they clarify whether additional protein complexes are required for STI NET1 interaction *in planta.* Furthermore, although the predicted ATPase-like central region of *STI* suggests possible regulatory activity, the biochemical experiments performed in this study did not provide evidence for detectable ATPase activity. Consequently, the precise biochemical function of STI remains unclear.

Taken together, the present results validate and further characterize the previously reported association between STI and NET1 proteins by identifying distinct interacting C-terminal regions within several NET1 paralogs. These findings establish a potential molecular connection between *STI* and cytoskeleton-associated membrane organization and provide a basis for future studies investigating the role of STI-containing protein complexes during trichome branch initiation.

6 Outlook

Despite more than two decades since the identification of *STI* as a central regulator of trichome branching, its molecular function remains unresolved. The results obtained in this work narrow down possible functional models and provide new experimental tools for future investigations. In particular, the generated fluorescent reporter lines and the identification of candidate interaction partners establish a basis for addressing STI function directly *in planta*. Beyond their use for genetic verification, the generated knock-in lines also enabled first microscopic analyses of endogenous STI localization. Preliminary confocal analyses already demonstrated that endogenous STI-tdTomato fluorescence can be detected in CRISPR/Cas9-generated knock-in lines, despite the weak signal intensity expected under endogenous promoter control (Fig. 19, Fig. 40, Fig. 41). Future analyses of backcrossed lines with restored trichome development will provide an important opportunity to investigate STI localization dynamics under native expression conditions in developing trichomes.

A major challenge for future work will be to integrate *STI* into the broader cellular framework of branch initiation. Trichome branching depends on highly coordinated spatial regulation of cytoskeletal organization, membrane dynamics, and localized cell expansion (Mathur & Chua, 2000; Sambade et al., 2014). Whether *STI* directly contributes to these processes or acts upstream within a regulatory pathway remains unknown. High-resolution live-cell imaging approaches combining STI reporters with cytoskeletal markers may help to resolve the temporal relationship between STI localization and branch establishment. In addition, perturbation experiments using cytoskeletal inhibitors could provide further insight into whether endogenous STI localization or dynamics depend on actin or microtubule organization during branch initiation.

Another important open question concerns the biochemical nature of STI itself. Although structural predictions support the presence of an ATPase-like core region, the absence of detectable ATPase activity raises the possibility that STI has undergone functional divergence. It therefore remains possible that the conserved ATPase-associated architecture fulfils primarily structural or regulatory roles rather than enzymatic functions. To further address this question, additional constructs have already been generated targeting the predicted ATP-binding and/or ATP-hydrolysis motifs of *STI*. These constructs are currently being introduced into the newly established parental reporter line as well as into the DD45 background for endogenous knock-

in approaches. Analysis of these lines may help to clarify whether the predicted ATPase-associated motifs are required for STI localization, protein function, or branch initiation under endogenous expression conditions. In parallel, ATP-binding assays are currently being established to directly test whether STI is capable of ATP binding despite the absence of detectable ATP hydrolysis.

In addition, the interaction between STI and NET1 proteins will require validation in systems independent of yeast two-hybrid assays. Since Y2H analyses are performed under heterologous nuclear conditions and may be influenced by steric effects of fusion proteins, complementary approaches such as co-immunoprecipitation, split-luciferase assays, or fluorescence-based interaction studies *in planta* will be important to determine whether STI-NET1 complexes form under physiological conditions.

More generally, the findings of this study highlight how proteins involved in plant morphogenesis may combine conserved structural features with highly specialized developmental functions. Understanding how *STI* contributes to the spatial control of branch initiation may therefore not only clarify trichome development in *Arabidopsis*, but also provide broader insights into the organization of localized growth processes in plant cells.

References

An, L., Zhou, Z., Su, S., Yan, A., & Gan, Y. (2012). GLABROUS INFLORESCENCE STEMS (GIS) is required for trichome branching through gibberellic acid signaling in *Arabidopsis*. *Plant and Cell Physiology*, *53*(2), 457–469. https://doi.org/10.1093/pcp/pcr192

Bailey, T. L., & Elkan, C. (1994). Fitting a mixture model by expectation maximization to discover motifs in biopolymers. www.aaai.org

Baskin, T. I. (2001). On the alignment of cellulose microfibrils by cortical microtubules: A review and a model. *Protoplasma*, *215*(1–4), 150–171. https://doi.org/10.1007/BF01280311

Baskin, T. I. (2005). Anisotrophic Expansion of the Plant Cell Wall. *Annual Review of Cell and Developmental Biology*, *21*(1), 203–222. https://doi.org/10.1146/annurev.cellbio.20.082503.103053

Bernard, P., & Couturier, M. (1992). Cell killing by the F plasmid CcdB protein involves poisoning of DNA-topoisomerase II complexes. *Journal of Molecular Biology*, *226*(3), 735–745. https://doi.org/10.1016/0022-2836(92)90629-X

Blum, M., Chang, H.-Y., Chuguransky, S., Grego, T., Kandasaamy, S., Mitchell, A., Nuka, G., Paysan-Lafosse, T., Qureshi, M., Raj, S., Richardson, L., Salazar, G. A., Williams, L., Bork, P., Bridge, A., Gough, J., Haft, D. H., Letunic, I., Marchler-Bauer, A., … Finn, R. D. (2021). The InterPro protein families and domains database: 20 years on. *Nucleic Acids Research*, *49*(D1), D344–D354. https://doi.org/10.1093/nar/gkaa977

Chen, L., Peng, Y., Tian, J., Wang, X., Kong, Z., Mao, T., Yuan, M., & Li, Y. (2016). TCS1, a microtubule-binding protein, interacts with KCBP/ZWICHEL to regulate trichome cell shape in *Arabidopsis thaliana*. *PLoS Genetics*, *12*(10). https://doi.org/10.1371/journal.pgen.1006266

Chen, X., Zaro, J. L., & Shen, W.-C. (2013). Fusion protein linkers: Property, design and functionality. *Advanced Drug Delivery Reviews*, *65*(10), 1357–1369. https://doi.org/10.1016/j.addr.2012.09.039

Clough, S. J., & Bent, A. F. (1998). Floral dip: a simplified method for *Agrobacterium*-mediated transformation of *Arabidopsis thaliana*. *The Plant Journal*, *16*(6), 735–743. https://doi.org/10.1046/j.1365-313x.1998.00343.x

Cosgrove, D. J. (2005). Growth of the plant cell wall. *Nature Reviews Molecular Cell Biology*, *6*(11), 850–861. https://doi.org/10.1038/nrm1746

Dalin, P., Ågren, J., Björkman, C., Huttunen, P., & Kärkkäinen, K. (2008). Leaf trichome formation and plant resistance to herbivory. In *Induced Plant Resistance to Herbivory* (pp. 89–105). Springer Netherlands. https://doi.org/10.1007/978-1-4020-8182-8_4

Deeks, M. J., Calcutt, J. R., Ingle, E. K. S., Hawkins, T. J., Chapman, S., Richardson, A. C., Mentlak, D. A., Dixon, M. R., Cartwright, F., Smertenko, A. P., Oparka, K., & Hussey, P. J. (2012). A superfamily of actin-binding proteins at the actin-membrane nexus of higher plants. *Current Biology*, *22*(17), 1595–1600. https://doi.org/10.1016/j.cub.2012.06.041

Denay, G., Schultz, P., Hänsch, S., Weidtkamp-Peters, S., & Simon, R. (2019). Over the rainbow: A practical guide for fluorescent protein selection in plant FRET experiments. *Plant Direct*, *3*(12). https://doi.org/10.1002/pld3.189

Duckney, P. J., Wang, P., & Hussey, P. J. (2025). Plant NETWORKED and VAP27 proteins work in complexes to regulate membrane-based functions. *Contact: The Journal of Inter-Organelle Communication*, *8*. https://doi.org/10.1177/25152564251342533

Duderstadt, K. E., Mott, M. L., Crisona, N. J., Chuang, K., Yang, H., & Berger, J. M. (2010). Origin remodeling and opening in bacteria rely on distinct assembly states of the DnaA initiator. *Journal of Biological Chemistry*, *285*(36), 28229–28239. https://doi.org/10.1074/jbc.M110.147975

Erzberger, J. P., & Berger, J. M. (2006). Evolutionary relationships and structural mechanisms of AAA^+ proteins. *Annual Review of Biophysics and Biomolecular Structure*, *35*(1), 93–114. https://doi.org/10.1146/annurev.biophys.35.040405.101933

Fields, S., & Song, O. (1989). A novel genetic system to detect protein–protein interactions. *Nature*, *340*(6230), 245–246. https://doi.org/10.1038/340245a0

Folkers, U., Berger, J., & Hülskamp, M. (1997). Cell morphogenesis of trichomes in *Arabidopsis*: differential control of primary and secondary branching by branch initiation

regulators and cell growth. *Development*, *124*(19), 3779–3786. https://doi.org/10.1242/dev.124.19.3779

Gasteiger, E., Hoogland, C., Gattiker, A., Duvaud, S., Wilkins, M. R., Appel, R. D., & Bairoch, A. (2005). Protein identification and analysis tools on the ExPASy server. In *The Proteomics Protocols Handbook* (pp. 571–607). Humana Press. https://doi.org/10.1385/1-59259-890-0:571

Gilding, E. K., & Marks, M. D. (2010). Analysis of purified glabra3-shapeshifter trichomes reveals a role for *NOECK* in regulating early trichome morphogenic events. *The Plant Journal*, *64*(2), 304–317. https://doi.org/10.1111/j.1365-313X.2010.04329.x

Glas, J., Schimmel, B., Alba, J., Escobar-Bravo, R., Schuurink, R., & Kant, M. (2012). Plant glandular trichomes as targets for breeding or engineering of resistance to herbivores. *International Journal of Molecular Sciences*, *13*(12), 17077–17103. https://doi.org/10.3390/ijms131217077

Hanahan, D. (1983). Studies on transformation of *Escherichia coli* with plasmids. *Journal of Molecular Biology*, *166*(4), 557–580. https://doi.org/10.1016/S0022-2836(83)80284-8

Hanson, P. I., & Whiteheart, S. W. (2005). AAA^+ proteins: have engine, will work. *Nature Reviews Molecular Cell Biology*, *6*(7), 519–529. https://doi.org/10.1038/nrm1684

Hauser, M.-T. (2014). Molecular basis of natural variation and environmental control of trichome patterning. *Frontiers in Plant Science*, *5*. https://doi.org/10.3389/fpls.2014.00320

Herrmann, U. (2007). Two genes involved in trichome morphogenesis: Localisation and putative function of STI and At-CLASP in *A. thaliana*.

Huang, C.-C. (2008). Functional Characterization of the STICHEL Gene in *Arabidopsis thaliana*. Doctoral dissertation, University of Cologne, Germany.

Huang, T. K., & Puchta, H. (2019). CRISPR/Cas-mediated gene targeting in plants: finally a turn for the better for homologous recombination. In *Plant Cell Reports* (Vol. 38, Number 4, pp. 443–453). Springer Verlag. https://doi.org/10.1007/s00299-019-02379-0

Hülskamp, M. (2004). Plant trichomes: a model for cell differentiation. *Nature Reviews Molecular Cell Biology*, *5*(6), 471–480. https://doi.org/10.1038/nrm1404

Hülskamp, M. (2019). Trichomes. *Current Biology*, *29*(8), R273–R274. https://doi.org/10.1016/j.cub.2019.02.010

Hülskamp, M., Miséra, S., & Jürgens, G. (1994). Genetic dissection of trichome cell development in *Arabidopsis*. *Cell*, *76*(3), 555–566. https://doi.org/10.1016/0092-8674(94)90118-X

Hussey, P. J., Ketelaar, T., & Deeks, M. J. (2006). Control of the actin cytoskeleton in plant cell growth. *Annual Review of Plant Biology*, *57*(1), 109–125. https://doi.org/10.1146/annurev.arplant.57.032905.105206

Ilgenfritz, H., Bouyer, D., Schnittger, A., Mathur, J., Kirik, V., Schwab, B., Chua, N.-H., Jürgens, G., & Hülskamp, M. (2003). The *Arabidopsis* STICHEL gene is a regulator of trichome branch number and encodes a novel protein. *Plant Physiology*, *131*(2), 643–655. https://doi.org/10.1104/pp.014209

Jelínková, B., Bellinvia, E., & Schwarzerová, K. (2026). Recent insights into the plant ARP2/3 complex. *Protoplasma*. https://doi.org/10.1007/s00709-026-02199-6

Jumper, J., Evans, R., Pritzel, A., Green, T., Figurnov, M., Ronneberger, O., Tunyasuvunakool, K., Bates, R., Žídek, A., Potapenko, A., Bridgland, A., Meyer, C., Kohl, S. A. A., Ballard, A. J., Cowie, A., Romera-Paredes, B., Nikolov, S., Jain, R., Adler, J., … Hassabis, D. (2021). Highly accurate protein structure prediction with AlphaFold. *Nature*, *596*(7873), 583–589. https://doi.org/10.1038/s41586-021-03819-2

Kasili, R., Huang, C.-C., Walker, J. D., Simmons, L. A., Zhou, J., Faulk, C., Hülskamp, M., & Larkin, J. C. (2011). BRANCHLESS TRICHOMES links cell shape and cell cycle control in *Arabidopsis* trichomes. *Development*, *138*(11), 2379–2388. https://doi.org/10.1242/dev.058982

Katoh, K., & Standley, D. M. (2013). MAFFT Multiple Sequence Alignment Software Version 7: Improvements in performance and usability. *Molecular Biology and Evolution*, *30*(4), 772–780. https://doi.org/10.1093/molbev/mst010

Khan, Y. A., White, K. I., & Brunger, A. T. (2022). The AAA^+ superfamily: a review of the structural and mechanistic principles of these molecular machines. *Critical Reviews in Biochemistry and Molecular Biology*, *57*(2), 156–187. https://doi.org/10.1080/10409238.2021.1979460

Kim, T.-W., Park, C. H., Hsu, C.-C., Kim, Y.-W., Ko, Y.-W., Zhang, Z., Zhu, J.-Y., Hsiao, Y.-C., Branon, T., Kaasik, K., Saldivar, E., Li, K., Pasha, A., Provart, N. J., Burlingame, A. L., Xu, S.-L., Ting, A. Y., & Wang, Z.-Y. (2023). Mapping the signaling network of BIN2 kinase using TurboID-mediated biotin labeling and phosphoproteomics. *The Plant Cell*, *35*(3), 975–993. https://doi.org/10.1093/plcell/koad013

Knowles, A. F. (2011). The GDA1_CD39 superfamily: NTPDases with diverse functions. *Purinergic Signalling*, *7*(1), 21–45. https://doi.org/10.1007/s11302-010-9214-7

Koncz, C., & Schell, J. (1986). The promoter of TL-DNA gene 5 controls the tissue-specific expression of chimaeric genes carried by a novel type of *Agrobacterium* binary vector. *Molecular and General Genetics MGG*, *204*(3), 383–396. https://doi.org/10.1007/BF00331014

Labun, K., Montague, T. G., Krause, M., Torres Cleuren, Y. N., Tjeldnes, H., & Valen, E. (2019). CHOPCHOP v3: expanding the CRISPR web toolbox beyond genome editing. *Nucleic Acids Research*, *47*(W1), W171–W174. https://doi.org/10.1093/nar/gkz365

Leipe, D. D., Wolf, Y. I., Koonin, E. V, & Aravind, L. (2002). Classification and evolution of P-loop GTPases and related ATPases. *Journal of Molecular Biology*, *317*(1), 41–72. https://doi.org/10.1006/jmbi.2001.5378

Le, J., El-Assal, S. E.-D., Basu, D., Saad, M. E., & Szymanski, D. B. (2003). Requirements for *Arabidopsis* ATARP2 and ATARP3 during epidermal development. *Current Biology*, *13*(15), 1341–1347. https://doi.org/10.1016/S0960-9822(03)00493-7

Li, J., Kim, T., & Szymanski, D. B. (2019). Multi-scale regulation of cell branching: Modeling morphogenesis. In *Developmental Biology* (Vol. 451, Number 1, pp. 40–52). Elsevier Inc. https://doi.org/10.1016/j.ydbio.2018.12.004

Lindsley, J. E. (2001). Use of a real-time, coupled assay to measure the ATPase activity of DNA topoisomerase II. In *DNA Topoisomerase Protocols* (pp. 57–64). Humana Press. https://doi.org/10.1385/1-59259-057-8:57

Liu, W., Xie, Y., Ma, J., Luo, X., Nie, P., Zuo, Z., Lahrmann, U., Zhao, Q., Zheng, Y., Zhao, Y., Xue, Y., & Ren, J. (2015). IBS: an illustrator for the presentation and visualization of biological sequences. *Bioinformatics*, *31*(20), 3359–3361. https://doi.org/10.1093/bioinformatics/btv362

Lu, S., Wang, J., Chitsaz, F., Derbyshire, M. K., Geer, R. C., Gonzales, N. R., Gwadz, M., Hurwitz, D. I., Marchler, G. H., Song, J. S., Thanki, N., Yamashita, R. A., Yang, M., Zhang, D., Zheng, C., Lanczycki, C. J., & Marchler-Bauer, A. (2020). CDD/SPARCLE: the conserved domain database in 2020. *Nucleic Acids Research*, *48*(D1), D265–D268. https://doi.org/10.1093/nar/gkz991

Mao, Y., Zhang, Z., Feng, Z., Wei, P., Zhang, H., Botella, J. R., & Zhu, J. (2016). Development of germ-line-specific CRISPR -Cas9 systems to improve the production of heritable gene modifications in *Arabidopsis*. *Plant Biotechnology Journal*, *14*(2), 519–532. https://doi.org/10.1111/pbi.12468

Marks, M. D., Wenger, J. P., Gilding, E., Jilk, R., & Dixon, R. A. (2009). Transcriptome analysis of *Arabidopsis* wild-type and *gl3–sst sim* trichomes identifies four additional genes required for trichome development. *Molecular Plant*, *2*(4), 803–822. https://doi.org/10.1093/mp/ssp037

Mathur, J. (2005). The ARP2/3 complex: giving plant cells a leading edge. *BioEssays*, *27*(4), 377–387. https://doi.org/10.1002/bies.20206

Mathur, J. (2006). Trichome cell morphogenesis in *Arabidopsis*: a continuum of cellular decisions. Special Issue on Plant Cell Biology. *Canadian Journal of Botany*, *84*(4), 604–612. https://doi.org/10.1139/b06-019

Mathur, J., & Chua, N.-H. (2000). Microtubule stabilization leads to growth reorientation in *Arabidopsis* trichomes. *The Plant Cell*, *12*(4), 465–477. https://doi.org/10.1105/tpc.12.4.465

Mathur, J., Spielhofer, P., Kost, B., & Chua, N.-H. (1999). The actin cytoskeleton is required to elaborate and maintain spatial patterning during trichome cell morphogenesis in *Arabidopsis thaliana*. *Development*, *126*(24), 5559–5568. https://doi.org/10.1242/dev.126.24.5559

Miki, D., Zhang, W., Zeng, W., Feng, Z., & Zhu, J.-K. (2018). CRISPR/Cas9-mediated gene targeting in *Arabidopsis* using sequential transformation. *Nature Communications*, *9*(1), 1967. https://doi.org/10.1038/s41467-018-04416-0

Miki, T., Ae Park, J., Nagao, K., Murayama, N., & Horiuchi, T. (1992). Control of segregation of chromosomal DNA by sex factor F in *Escherichia coli*. *Journal of Molecular Biology*, *225*(1), 39–52. https://doi.org/10.1016/0022-2836(92)91024-J

Mistry, J., Chuguransky, S., Williams, L., Qureshi, M., Salazar, G. A., Sonnhammer, E. L. L., Tosatto, S. C. E., Paladin, L., Raj, S., Richardson, L. J., Finn, R. D., & Bateman, A. (2021). Pfam: The protein families database in 2021. *Nucleic Acids Research*, *49*(D1), D412–D419. https://doi.org/10.1093/nar/gkaa913

Niu, L., Xie, W., Li, Q., Wang, Y., Zhang, X., Shi, M., Zeng, J., Li, M., Wang, Y., Shao, J., Yu, F., & An, L. (2024). BEACH domain-containing protein SPIRRIG facilitates microtubule cytoskeleton-associated trichome morphogenesis in *Arabidopsis*. *Planta*, *260*(5). https://doi.org/10.1007/s00425-024-04545-5

Oldfield, C. J., & Dunker, A. K. (2014). Intrinsically disordered proteins and intrinsically disordered protein regions. *Annual Review of Biochemistry*, *83*(1), 553–584. https://doi.org/10.1146/annurev-biochem-072711-164947

Oppenheimer, D. G., Pollock, M. A., Vacik, J., Szymanski, D. B., Ericson, B., ¶ K. F., & Marks, M. D. (1997). Essential role of a kinesin-like protein in *Arabidopsis* trichome morphogenesis. In *Developmental Biology* (Vol. 94). https://www.pnas.org

Pattanaik, S., Patra, B., Singh, S. K., & Yuan, L. (2014). An overview of the gene regulatory network controlling trichome development in the model plant, *Arabidopsis*. In *Frontiers in Plant Science* (Vol. 5, Number JUN). Frontiers Research Foundation. https://doi.org/10.3389/fpls.2014.00259

Payne, C. T., Zhang, F., & Lloyd, A. M. (2000). *GL3* encodes a bHLH protein that regulates trichome development in *Arabidopsis* through interaction with GL1 and TTG1. *Genetics*, *156*(3), 1349–1362. https://doi.org/10.1093/genetics/156.3.1349

Perazza, D., Herzog, M., Hülskamp, M., Brown, S., Dorne, A.-M., & Bonneville, J.-M. (1999). Trichome cell growth in *Arabidopsis thaliana* can be derepressed by mutations in at least five genes. *Genetics*, *152*(1), 461–476. https://doi.org/10.1093/genetics/152.1.461

Perazza, D., Vachon, G., & Herzog, M. (1998). Gibberellins promote trichome formation by up-regulating GLABROUS1 in *Arabidopsis*. *Plant Physiology*, *117*(2), 375–383. https://doi.org/10.1104/pp.117.2.375

Pettersen, E. F., Goddard, T. D., Huang, C. C., Meng, E. C., Couch, G. S., Croll, T. I., Morris, J. H., & Ferrin, T. E. (2021). UCSF ChimeraX: Structure visualization for researchers, educators, and developers. *Protein Science*, *30*(1), 70–82. https://doi.org/10.1002/pro.3943

Saedler, R., Jakoby, M., Marin, B., Galiana-Jaime, E., & Hülskamp, M. (2009). The cell morphogenesis gene SPIRRIG in *Arabidopsis* encodes a WD/BEACH domain protein. *The Plant Journal*, *59*(4), 612–621. https://doi.org/10.1111/j.1365-313X.2009.03900.x

Sambade, A., Findlay, K., Schäffner, A. R., Lloyd, C. W., & Buschmann, H. (2014). Actin-dependent and -independent functions of cortical microtubules in the differentiation of *Arabidopsis* leaf trichomes. *Plant Cell*, *26*(4), 1629–1644. https://doi.org/10.1105/tpc.113.118273

Schnittger, A., Folkers, U., Schwab, B., Jurgens, G., & Hulskamp, M. (1999). Generation of a spacing pattern: The Role of *TRIPTYCHON* in trichome patterning in *Arabidopsis*. *The Plant Cell*, *11*(6), 1105. https://doi.org/10.2307/3870802

Schwab, B., Folkers, U., Ilgenfritz, H., & Hülskamp, M. (2000). Trichome morphogenesis in *Arabidopsis*. *Philosophical Transactions of the Royal Society of London. Series B: Biological Sciences*, *355*(1399), 879–883. https://doi.org/10.1098/rstb.2000.0623

Seitz, K., & Krysan, P. J. (2020). Expanding the toolkit of fluorescent biosensors for studying mitogen activated protein kinases in plants. *International Journal of Molecular Sciences*, *21*(15), 5350. https://doi.org/10.3390/ijms21155350

Shaner, N. C., Campbell, R. E., Steinbach, P. A., Giepmans, B. N. G., Palmer, A. E., & Tsien, R. Y. (2004). Improved monomeric red, orange and yellow fluorescent proteins derived from *Discosoma* sp. red fluorescent protein. *Nature Biotechnology*, *22*(12), 1567–1572. https://doi.org/10.1038/nbt1037

Sharan, A., Soni, P., Nongpiur, R. C., Singla-Pareek, S. L., & Pareek, A. (2017). Mapping the 'Two-component system' network in rice. *Scientific Reports*, *7*(1), 9287. https://doi.org/10.1038/s41598-017-08076-w

Shimada, T. L., Shimada, T., & Hara-Nishimura, I. (2010). A rapid and non-destructive screenable marker, FAST, for identifying transformed seeds of *Arabidopsis thaliana*. *The Plant Journal*, *61*(3), 519–528. https://doi.org/10.1111/j.1365-313X.2009.04060.x

Smith, L. G., & Oppenheimer, D. G. (2005). Spatial control of cell expansion by the plant cytoskeleton. *Annual Review of Cell and Developmental Biology*, *21*(1), 271–295. https://doi.org/10.1146/annurev.cellbio.21.122303.114901

Stracke, R., Werber, M., & Weisshaar, B. (2001). The R2R3-MYB gene family in *Arabidopsis thaliana. Current Opinion in Plant Biology*, *4*(5), 447–456. https://doi.org/10.1016/S1369-5266(00)00199-0

Studier, F. W., & Moffatt, B. A. (1986). Use of bacteriophage T7 RNA polymerase to direct selective high-level expression of cloned genes. *Journal of Molecular Biology*, *189*(1), 113–130. https://doi.org/10.1016/0022-2836(86)90385-2

Szymanski, D. B. (2005). Breaking the WAVE complex: the point of *Arabidopsis* trichomes. *Current Opinion in Plant Biology*, *8*(1), 103–112. https://doi.org/10.1016/j.pbi.2004.11.004

Szymanski, D. B., Lloyd, A. M., & Marks, M. D. (2000). Progress in the molecular genetic analysis of trichome initiation and morphogenesis in *Arabidopsis*. *Trends in Plant Science*, *5*(5), 214–219. https://doi.org/10.1016/S1360-1385(00)01597-1

Szymanski, D. B., & Marks, M. D. (1998). *GLABROUS1* Overexpression and *TRIPTYCHON* alter the cell cycle and trichome cell fate in *Arabidopsis*. *The Plant Cell*, *10*(12), 2047–2062. https://doi.org/10.1105/tpc.10.12.2047

Szymanski, D. B., Marks, M. D., & Wick, S. M. (1999). Organized F-actin is essential for normal trichome morphogenesis in *Arabidopsis*. *The Plant Cell*, *11*(12), 2331–2347. https://doi.org/10.1105/tpc.11.12.2331

van Rosmalen, M., Krom, M., & Merkx, M. (2017). Tuning the flexibility of glycine-serine linkers to allow rational design of multidomain proteins. *Biochemistry*, *56*(50), 6565–6574. https://doi.org/10.1021/acs.biochem.7b00902

Varadi, M., Anyango, S., Deshpande, M., Nair, S., Natassia, C., Yordanova, G., Yuan, D., Stroe, O., Wood, G., Laydon, A., Žídek, A., Green, T., Tunyasuvunakool, K., Petersen, S., Jumper, J., Clancy, E., Green, R., Vora, A., Lutfi, M., … Velankar, S. (2022). AlphaFold Protein Structure Database: massively expanding the structural coverage of protein-sequence space with high-accuracy models. *Nucleic Acids Research*, *50*(D1), D439–D444. https://doi.org/10.1093/nar/gkab1061

Walker, J. E., Saraste, M., Runswick, M. J., & Gay, N. J. (1982). Distantly related sequences in the alpha- and beta-subunits of ATP synthase, myosin, kinases and other ATP-requiring enzymes and a common nucleotide binding fold. *The EMBO Journal*, *1*(8), 945–951. https://doi.org/10.1002/j.1460-2075.1982.tb01276.x

Wang, G., Feng, H., Sun, J., & Du, X. (2013). Induction of cotton ovule culture fibre branching by co-expression of cotton *BTL*, cotton *SIM*, and *Arabidopsis STI* genes. *Journal of Experimental Botany*, *64*(14), 4157–4168. https://doi.org/10.1093/jxb/ert222

Waterhouse, A. M., Procter, J. B., Martin, D. M. A., Clamp, M., & Barton, G. J. (2009). Jalview Version 2—a multiple sequence alignment editor and analysis workbench. *Bioinformatics*, *25*(9), 1189–1191. https://doi.org/10.1093/bioinformatics/btp033

Wright, P. E., & Dyson, H. J. (2015). Intrinsically disordered proteins in cellular signalling and regulation. *Nature Reviews Molecular Cell Biology*, *16*(1), 18–29. https://doi.org/10.1038/nrm3920

Xi, A., Yang, X., Deng, M., Chen, Y., Shao, J., Zhao, J., & An, L. (2018). Isolation and identification of two new alleles of *STICHEL* in *Arabidopsis*. *Biochemical and Biophysical Research Communications*, *499*(3), 605–610. https://doi.org/10.1016/j.bbrc.2018.03.197

Xu, L., Cao, L., Li, J., & Staiger, C. J. (2024). Cooperative actin filament nucleation by the Arp2/3 complex and formins maintains the homeostatic cortical array in *Arabidopsis* epidermal cells. *Plant Cell*, *36*(3), 764–789. https://doi.org/10.1093/plcell/koad301

Zhao, M., Morohashi, K., Hatlestad, G., Grotewold, E., & Lloyd, A. (2008). The TTG1-bHLH-MYB complex controls trichome cell fate and patterning through direct targeting of regulatory loci. *Development*, *135*(11), 1991–1999. https://doi.org/10.1242/dev.016873

Appendix

Use of AI-assisted tools

Generative AI tools (ChatGPT, OpenAI, based on GPT-5.5, accessed May 2026) were used during the preparation of this dissertation to support language editing, text structuring, refinement of scientific formulations, paper summarization and literature research. Fig. 8 was created with the assistance of ChatGPT, carefully reviewed and edited manually in Powerpoint. Perplexity (accessed May 2026) was used for assistance in coding. The use of these tools was conducted in accordance with the currently applicable AI policy (KI-Richtlinie vom 27. Januar 2026) of the University of Cologne.

All scientific content, including experimental design, data analysis, interpretation of results, and conclusions, was developed independently by the author. AI tools were not used to generate or modify primary data or experimental results. All outputs generated with the assistance of AI were critically reviewed and revised sentence by sentence by the author to ensure scientific accuracy and integrity.

Example ChimeraX command generated in assistance with Perplexity

```
# load structure
open AlphaFold_STI_At.pdb

# basic visualization
hide
cartoon
set bgColor white

# color full structure
color grey

# highlight central region
select :450-750
color sel #3A5FCD


# show Walker motifs
style :490-497 stick
style :569-574 stick


color :490-497 #CC0000
color :569-574 #FF8C00

# adjust stick size
size stickRadius 0.4

# center view
```

view

export image
save panelB_STICHEL.png

Additional Malachite Green ATPase results

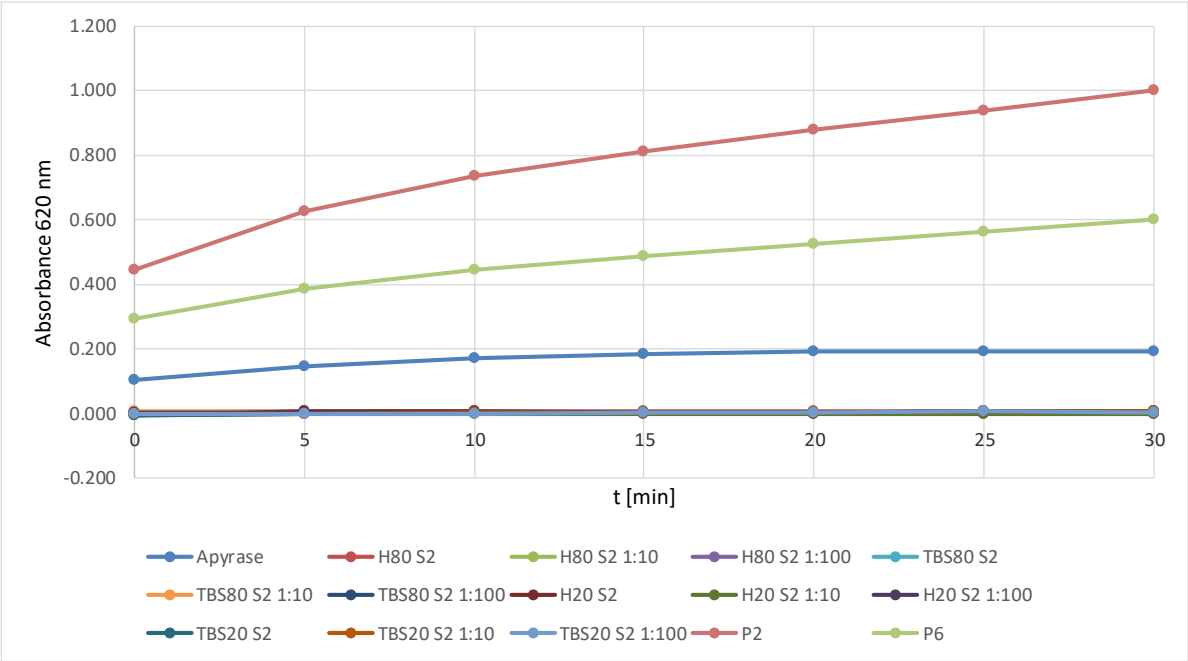

Fig. 32: Malachite Green ATPase assay of the STI S2 fragment under different storage and buffer conditions.
ATP hydrolysis was assessed by measuring phosphate-dependent absorbance at 620 nm over 30 min. The STI S2 fragment was analysed in either TBS buffer (TBS) or HEPES buffer (H), using protein samples stored at −20 °C or −80 °C. Protein dilutions of 1:10 and 1:100 were additionally tested where indicated. Potato apyrase served as a positive control. P2 and P6 represent phosphate standards supplied with the assay kit. Increased absorbance over time was observed for the phosphate standards and the apyrase control, whereas no detectable phosphate release was observed for the STI S2 samples under the tested conditions.

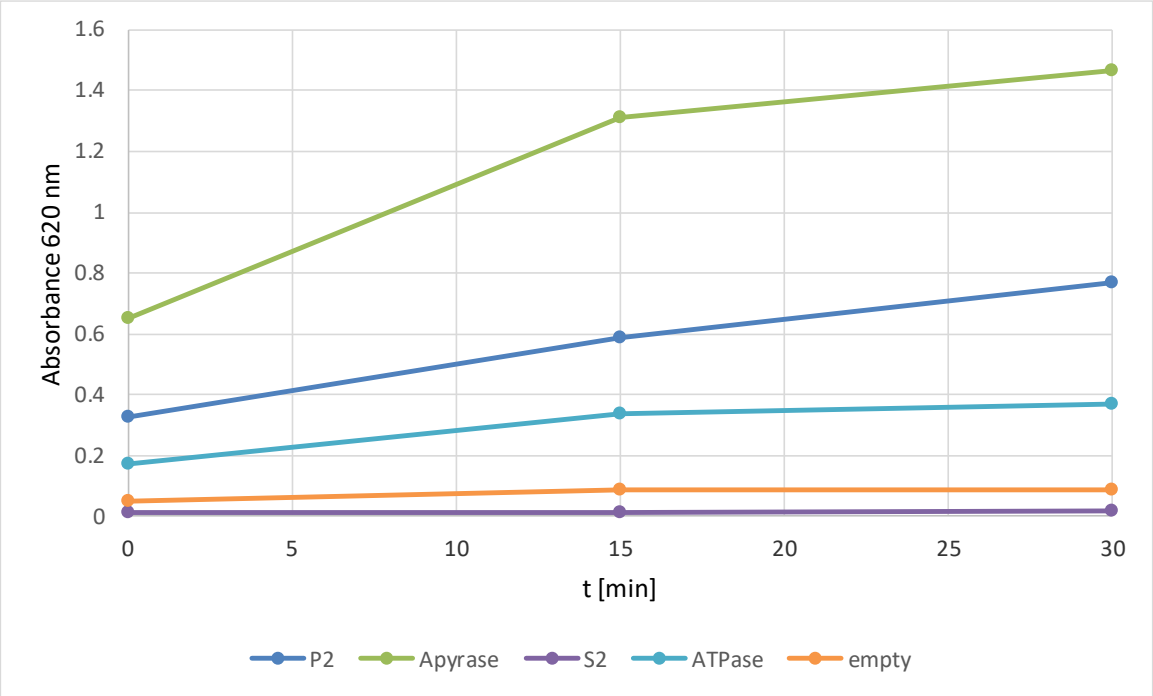

Fig. 33: Malachite Green ATPase assay of the STI S2 fragment and the ATPase-extended STI fragment.
ATP hydrolysis was assessed by measuring phosphate-dependent absorbance at 620 nm over 30 min. Potato apyrase served as a positive control, while the MBP empty vector control was included to assess background phosphate release. P2 represents a phosphate standard supplied with the assay kit. The ATPase-extended STI fragment ("ATPase") showed a moderate increase in absorbance over time in this experiment, whereas the STI S2 fragment ("S2") remained at background levels comparable to the empty vector control. However, the signal increase observed for the ATPase-extended fragment could not be reproduced in independent experiments. The apyrase control produced the strongest increase in absorbance, confirming assay functionality.

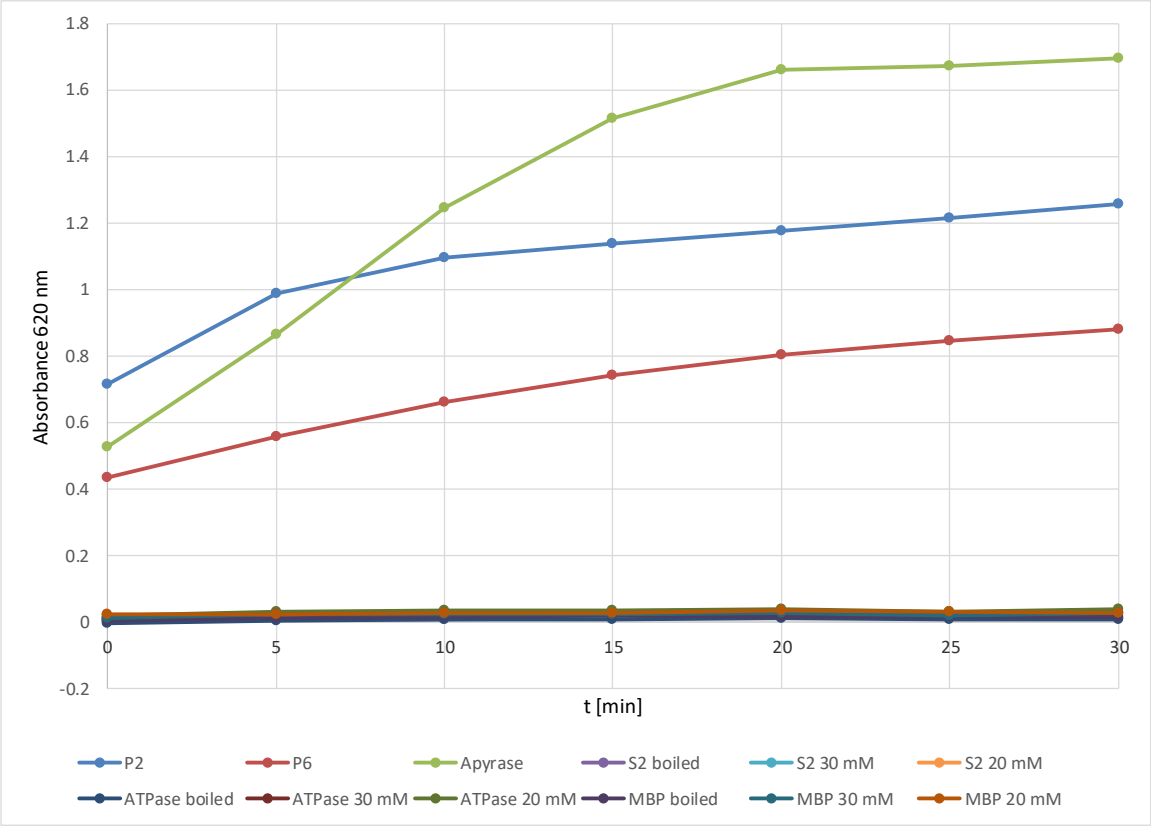

Fig. 34: Malachite Green ATPase assay of STI fragments after heat denaturation and under different maltose elution conditions.
ATP hydrolysis was assessed by measuring phosphate-dependent absorbance at 620 nm over 30 min. STI S2 and ATPase-extended fragments were analysed following elution with either 20 mM or 30 mM maltose. Corresponding boiled protein samples and MBP controls were included to assess background phosphate release. Potato apyrase served as a positive control, while P2 and P6 represent phosphate standards supplied with the assay kit. The phosphate standards (P2 and P6) and the apyrase control showed clear increases in absorbance over time, confirming assay functionality. In contrast, all STI fragment samples, including the ATPase-extended fragment under different elution conditions, remained at background levels comparable to the MBP controls.

Additional coupled enzyme ATPase results

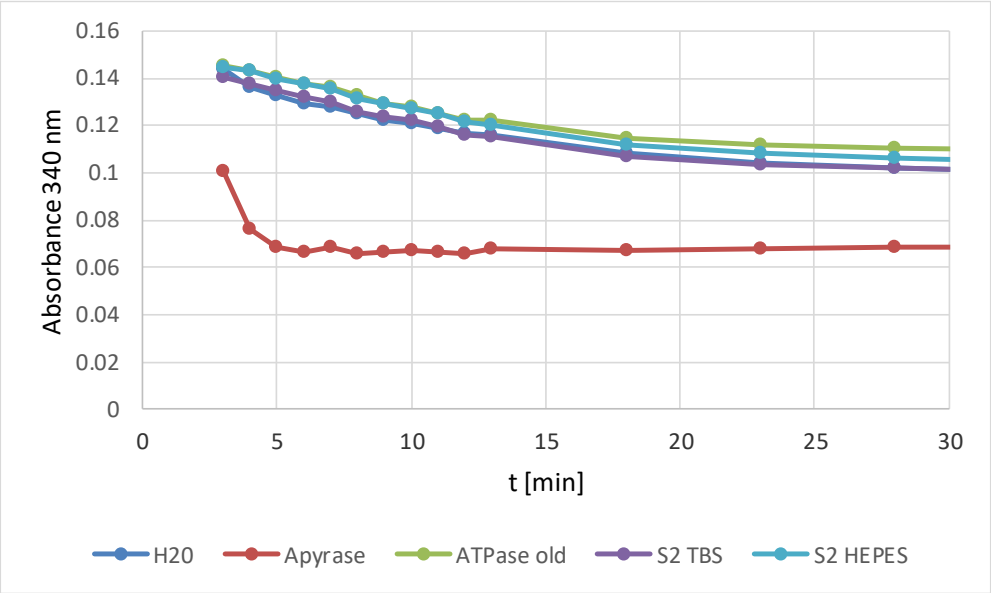

Fig. 35: Coupled enzymatic ATPase assay monitoring NADH consumption over time.
ATPase activity was assessed using a coupled assay linking ATP hydrolysis to NADH oxidation. NADH levels were monitored by measuring absorbance at 340 nm over time. Apyrase served as a positive control and showed a rapid decrease in absorbance, indicating ATP hydrolysis and coupled NADH consumption, followed by a plateau phase after approximately 7 min, consistent with reaction saturation. In contrast, the STI-derived fragments ("ATPase old", "S2 TBS", and "S2 HEPES") displayed absorbance profiles comparable to the H2O control and no detectable ATPase activity under the tested conditions.

CRISPR/Cas9 additional information

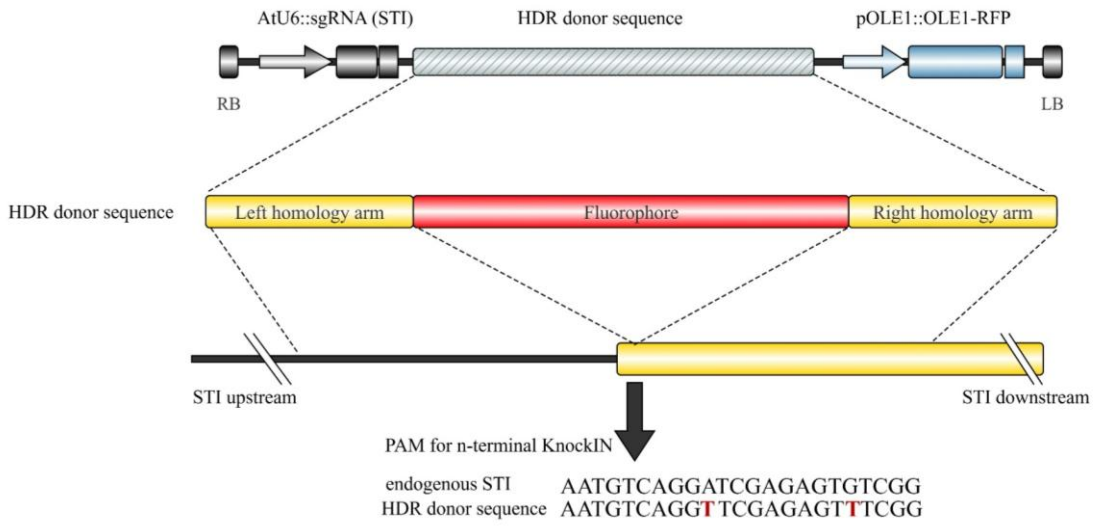

Fig. 36: Structure of the HDR donor construct used for STI N-terminal fluorophore knock-in. The construct contains an *AtU6*-driven sgRNA targeting *STI*, the HDR donor sequence consisting of left and right homology arms flanking the fluorophore sequence, and the seed fluorescence selection cassette *pOLE1::OLE1-RFP*. The lower panel illustrates the targeted *STI* genomic locus and the position of the N-terminal knock-in. Silent nucleotide substitutions were introduced into the donor sequence in the PAM target region to prevent *Cas9*-mediated re-cutting after homologous recombination. Adapted from (D. Miki et al., 2018). Figure created in BioRender and IBS

Sequences of *STI* knock-in constructs

Fluorophores are highlighted in red and green, the PAMs including silent mutations are highlighted in bolt. A linker sequence is highlighted in lower case letters. Repair fragments are flanked by the respective restriction sites for cloning (AsCI and Mfe/SpeI).

HDR donor fragment for STI N-terminal Knock-in with tdTomato

AAAGGCGCGCCAGTATTCATCATGATGTTTATTTTATTTTTTTGACTAAATTTGTTAGTATTTTTTTGAGAAAAAAAGAAAGAA
AAAACTAAGTGTGACGAGACACGAAAACACTAGACAAGGAGGGGCTTTGACGAGACCCGAACAAACAAATGTGAATTTAAA
AAAACCCATTAAAATAATTAAAAATAATGGAAATTTAAAAATAGAAAATAATAGTGTCTCTCGCTTTCCTTCATGCGTTCTCT
CGCAGTCGCAGGCGACTATCAAGTTTCAGAACTCGAGATTCATCATTCTCTGTTCCACTTCCGGCGATGTATTATAATCCCTAG
ACCTTAGTTCCGGCGAACTCTCGAAGAACAAACAAGTATATATTATTATTTTCTTCTTAGTGTTTCGTGCTGTTTCCACGATTC
CTTCGTTTTATCTTGGATCTACAGTTTTACATTCTTCTGTTTTTCTTCACTTTCATTGTTTCCACTGCGTTGTTCTGATTAGGTAT
TGCACAGGTTTTGAAATGTCAGTGAAAACGCGAAGCTGAGAGAGGAGAAGGAAGAAATCGAAGGAAGCTGATTCAAATTTA
GGAAGAAGAAAAAATGGTGAGCAAGGGCGAGGAGGTCATCAAAGAGTTCATGCGCTTCAAGGTGCGCATGGAGGGCTCCAT
GAACGGCCACGAGTTCGAGATCGAGGGCGAGGGCGAGGGCCGCCCCTACGAGGGCACCCAGACCGCCAAGCTGAAGGTGAC
CAAGGGCGGCCCCCTGCCCTTCGCCTGGGACATCCTGTCCCCCCAGTTCATGTACGGCTCCAAGGCGTACGTGAAGCACCCCG
CCGACATCCCCGATTACAAGAAGCTGTCCTTCCCCGAGGGCTTCAAGTGGGAGCGCGTGATGAACTTCGAGGACGGCGGTCT
GGTGACCGTGACCCAGGACTCCTCCCTGCAGGACGGCACGCTGATCTACAAGGTGAAGATGCGCGGCACCAACTTCCCCCCC
GACGGCCCCGTAATGCAGAAGAAGACCATGGGCTGGGAGGCCTCCACCGAGCGCCTGTACCCCCGCGACGGCGTGCTGAAG
GGCGAGATCCACCAGGCCCTGAAGCTGAAGGACGGCGGCCACTACCTGGTGGAGTTCAAGACCATCTACATGGCCAAGAAG
CCCGTGCAACTGCCCGGCTACTACTACGTGGACACCAAGCTGGACATCACCTCCCACAACGAGGACTACACCATCGTGGAAC
AGTACGAGCGCTCCGAGGGCCGCCACCACCTGTTCCTGGGGCATGGCACCGGCAGCACCGGCAGCGGCAGCTCCGGCACCGC
CTCCTCCGAGGACAACAACATGGCCGTCATCAAAGAGTTCATGCGCTTCAAGGTGCGCATGGAGGGCTCCATGAACGGCCAC
GAGTTCGAGATCGAGGGCGAGGGCGAGGGCCGCCCCTACGAGGGCACCCAGACCGCCAAGCTGAAGGTGACCAAGGGCGGC
CCCCTGCCCTTCGCCTGGGACATCCTGTCCCCCCAGTTCATGTACGGCTCCAAGGCGTACGTGAAGCACCCCGCCGACATCCC

CGATTACAAGAAGCTGTCCTTCCCCGAGGGCTTCAAGTGGGAGCGCGTGATGAACTTCGAGGACGGCGGTCTGGTGACCGTG
ACCCAGGACTCCTCCCTGCAGGACGGCACGCTGATCTACAAGGTGAAGATGCGCGGCACCAACTTCCCCCCCGACGGCCCCG
TAATGCAGAAGAAGACCATGGGCTGGGAGGCCTCCACCGAGCGCCTGTACCCCCGCGACGGCGTGCTGAAGGGCGAGATCC
ACCAGGCCCTGAAGCTGAAGGACGGCGGCCGCTACCTGGTGGAGTTCAAGACCATCTACATGGCCAAGAAGCCCGTGCAACT
GCCCGGCTACTACTACGTGGACACCAAGCTGGACATCACCTCCCACAACGAGGACTACACCATCGTGGAACAGTACGAGCGC
TCCGAGGGCCGCCACCACCTGTTCCTGTACGGCATGGACGAGCTGTACAAG**ATGTCAGGATCGAGAGTGTCGG**ATCTGAGT
AAATTGCATCTGAAGAAGGAGCTGACTCAAATCAGAAAAGCTGGCCGTGTTTTACGCGATCCAGGTACTACTTCCTCCTGGA
AATCTCCTCTCGATTCGTCAAGATCCGTCGCGCTTTTGGAGACTCCGGCGAGCAGAAACGGTGGCAGTTCGAGTCAGTTTCCG
ATTCGAGGAGAGAGTAGTACTAATCGTCGTGGGAAAGAGAAGAAGGTGTTTTTGTATAACTGGAAGACTCAGAAATCTTCTA
GTGAGAAAAGTGGATTAGCTAAGAATGGTAAGGAAGAAGAGGAAGAAGAAGAAGATGCTTCTTCGTGGACGCAAGCTAGTG
TTAATGATGATGATGATGTGAGTGATGCGAGGAATGGTGGTGATTCGTATCGTAGAGAAATACAATCAGCTTCGATGGGTTTT
AGGTGTAGAGATACGAATCTAGCGTCACAAGGTGTGTCAAAGATGAGGAAGAGTAATGTTGGTAGTTGTAAGAAGAAGAGT
AAGAAAAAAATTAGCTCTTCTCGTTTGGATTGTTTGTCAAAGTATCAACCTAGAGATGACATTGTTGCTAGAAATTGTAATGC
TGGATCAGATGAGGCGCGCCAAA

HDR donor fragment for STI C-terminal Knock-in with tdTomato

AAAGGCGCGCCTTCTACCTCAAGAAGACACTTATCGCCAAACTAACGTAGCTTCTGCTATTTCTTCTTCTGGCCTAACCACTCA
CCAATGGGTAGATGAGCTAAACAATGAAGTTAAGCTTTTGAAAATCGGCGACAATGGTGAGCTTCAGGAGAATCTAACCGGT
ACAAGAGGACAGCATTGTCCTCTTTCCCCAAGCTTACTTCATGATACTAACTTCGGAAACAACAAAGACAATCTGTAAGTTCC
TCACTCTGATCCTTTTCGATACAAAACCGAAAAGAAAAAACAAATAAGATCTTTATAATCAACGTATTGTCGTAATGATGTCA
TGTTTGGCTTTGGTTGTGTAGAGGAGGATACGAATCAGGATCAGGAAGAGTTGGTTGTAATATATTATTTTGTTGGAACACAA
AAAAGACTCAGAGACGAAGCAAGGTTTGTGCTAATAACTCGAATCTGTTCCTCCTTTTCGATGTTTTCTTTGTCTCATTTGTTT
TTCATTTGCGGATTTGATTAGTCGAAACAGGTCAAGGGAACTCCTGTTCGTTCGCGGAGAAATCGGAAGAGTCGGTTCTCTCT
GT**TTAATGGATGTGCTAAACCTAGG**AAAGCAGAAGGTAACATTAGAAGAATGGTGAGCAAGGGCGAGGAGGTCATCAAAG
AGTTCATGCGCTTCAAGGTGCGCATGGAGGGCTCCATGAACGGCCACGAGTTCGAGATCGAGGGCGAGGGCGAGGGCCGCC
CCTACGAGGGCACCCAGACCGCCAAGCTGAAGGTGACCAAGGGCGGCCCCCTGCCCTTCGCCTGGGACATCCTGTCCCCCCA
GTTCATGTACGGCTCCAAGGCGTACGTGAAGCACCCCGCCGACATCCCCGATTACAAGAAGCTGTCCTTCCCCGAGGGCTTCA
AGTGGGAGCGCGTGATGAACTTCGAGGACGGCGGTCTGGTGACCGTGACCCAGGACTCCTCCCTGCAGGACGGCACGCTGAT
CTACAAGGTGAAGATGCGCGGCACCAACTTCCCCCCCGACGGCCCCGTAATGCAGAAGAAGACCATGGGCTGGGAGGCCTCC
ACCGAGCGCCTGTACCCCCGCGACGGCGTGCTGAAGGGCGAGATCCACCAGGCCCTGAAGCTGAAGGACGGCGGCCACTAC
CTGGTGGAGTTCAAGACCATCTACATGGCCAAGAAGCCCGTGCAACTGCCCGGCTACTACTACGTGGACACCAAGCTGGACA
TCACCTCCCACAACGAGGACTACACCATCGTGGAACAGTACGAGCGCTCCGAGGGCCGCCACCACCTGTTCCTGGGGCATGG
CACCGGCAGCACCGGCAGCGGCAGCTCCGGCACCGCCTCCTCCGAGGACAACAACATGGCCGTCATCAAAGAGTTCATGCGC
TTCAAGGTGCGCATGGAGGGCTCCATGAACGGCCACGAGTTCGAGATCGAGGGCGAGGGCGAGGGCCGCCCCTACGAGGGC
ACCCAGACCGCCAAGCTGAAGGTGACCAAGGGCGGCCCCCTGCCCTTCGCCTGGGACATCCTGTCCCCCCAGTTCATGTACG
GCTCCAAGGCGTACGTGAAGCACCCCGCCGACATCCCCGATTACAAGAAGCTGTCCTTCCCCGAGGGCTTCAAGTGGGAGCG
CGTGATGAACTTCGAGGACGGCGGTCTGGTGACCGTGACCCAGGACTCCTCCCTGCAGGACGGCACGCTGATCTACAAGGTG
AAGATGCGCGGCACCAACTTCCCCCCCGACGGCCCCGTAATGCAGAAGAAGACCATGGGCTGGGAGGCCTCCACCGAGCGCC
TGTACCCCCGCGACGGCGTGCTGAAGGGCGAGATCCACCAGGCCCTGAAGCTGAAGGACGGCGGCCGCTACCTGGTGGAGTT
CAAGACCATCTACATGGCCAAGAAGCCCGTGCAACTGCCCGGCTACTACTACGTGGACACCAAGCTGGACATCACCTCCCAC
AACGAGGACTACACCATCGTGGAACAGTACGAGCGCTCCGAGGGCCGCCACCACCTGTTCCTGTACGGCATGGACGAGCTGT
ACAAGTAAAACTAAGTTCTTTAGTCATGAAAAACAAAATTGTTCCCTCAAGCTCTAATTTATCATCTGTTCTTCCACTTCCACA
TAGTTTTCCCTTAATTATGTTTGATAATGATATGTCAAAGGACAGTTTTAATATATTCACTGTAAAGTTCCTATCCATTTTTGTT
ATCTATCTTATAAAAACTTCAAAAATGTTACTGTGAAATAATCGACGAATTGGTTAACCTTGCACATTAGTTTATATTTTTCAA
TTTTTTTGTGTTGCATTTGTTGGAAAAATAAATAATATTTATTATTTGTGATTTACCTTTTTCAGTTATTGTAATTTTTAGTTTCA
TATTTACTTGGTTTATGACACATATTGAAACTATTGAAACAAATCAAAATTTCTATTGTTAAACTCTTTTCAAGTCTTAAAAAA
TATTAAAATTTTAAAATGAACAAAAAGGTTATGTAAGTTTTGTTTCACCTAACTTAAGCGGGGAGATGAAAAGTTGAAAAGTT
AGTAAATGTAATAGACCAAAGGGTTTGTCGCGGAGAATAAATTATAAAAGAAAACAAACTATAATTTTGGGCGCGCCAAA

HDR donor fragment for STI N-terminal Knock-in with mNeonGreen

AAAACTAGTAGTATTCATCATGATGTTTATTTTATTTTTTTGACTAAATTTGTTAGTATTTTTTTGAGAAAAAAAGAAAGAAAA
AACTAAGTGTGACGAGACACGAAAACACTAGACAAGGAGGGGCTTTGACGAGACCCGAACAAACAAATGTGAATTTAAAAA
AACCCATTAAAATAATTAAAAATAATGGAAATTTAAAAATAGAAAATAATAGTGTCTCTCGCTTTCCTTCATGCGTTCTCTCG
CAGTCGCAGGCGACTATCAAGTTTCAGAACTCGAGATTCATCATTCTCTGTTCCACTTCCGGCGATGTATTATAATCCCTAGAC
CTTAGTTCCGGCGAACTCTCGAAGAACAAACAAGTATATATTATTATTTTCTTCTTAGTGTTTCGTGCTGTTTCCACGATTCCTT
CGTTTTATCTTGGATCTACAGTTTTACATTCTTCTGTTTTTCTTCACTTTCATTGTTTCCACTGCGTTGTTCTGATTAGGTATTGC
ACAGGTTTTGAAATGTCAGTGAAAACGCGAAGCTGAGAGAGGAGAAGGAAGAAATCGAAGGAAGCTGATTCAAATTTAGGA
AGAAGAAAAAATGGTCTCAAAAGGTGAGGAAGATAATATGGCGTCGCTTCCAGCAACTCATGAACTTCACATTTTTGGATCT
ATCAATGGTGTTGATTTTGATATGGTTGGTCAAGGTACTGGAAACCCAAATGATGGTTATGAAGAGCTAAACCTCAAGAGCA
CAAAGGGAGATCTTCAGTTCTCACCGTGGATTTTAGTACCTCATATTGGGTATGGATTCCATCAATACCTCCCTTATCCTGATG
GCATGTCTCCATTTCAAGCCGCAATGGTGGATGGCTCTGGCTACCAAGTACACCGCACAATGCAGTTTGAAGACGGTGCTTCG
CTGACGGTGAACTATAGATACACTTATGAGGGATCTCACATCAAAGGAGAAGCTCAAGTCAAAGGGACTGGCTTCCCTGCGG
ACGGTCCGGTGATGACAAACTCCCTTACCGCAGCTGACTGGTGTAGAAGCAAGAAGACGTATCCCAATGACAAGACTATAAT
ATCCACATTCAAATGGAGTTATACAACCGGGAACGGAAAGCGTTACCGGTCAACAGCACGAACCACCTACACATTTGCTAAA
CCAATGGCTGCCAATTACTTGAAGAACCAGCCTATGTATGTTTTCAGGAAAACGGAGTTAAAACATAGTAAAACTGAGTTGA
ATTTCAAGGAATGGCAGAAGGCTTTTACTGATGTTATGGGAATGGATGAGTTGTACAAA*GGAGGAGGAGGATCTGGAGGAGGA*
*GGATCT***ATGTCAGGATCGAGAGTGTCGG**ATCTGAGTAAATTGCATCTGAAGAAGGAGCTGACTCAAATCAGAAAAGCTGGC
CGTGTTTTACGCGATCCAGGTACTACTTCCTCCTGGAAATCTCCTCTCGATTCGTCAAGATCCGTCGCGCTTTTGGAGACTCCG
GCGAGCAGAAACGGTGGCAGTTCGAGTCAGTTTCCGATTCGAGGAGAGAGTAGTACTAATCGTCGTGGGAAAGAGAAGAAG
GTGTTTTTGTATAACTGGAAGACTCAGAAATCTTCTAGTGAGAAAAGTGGATTAGCTAAGAATGGTAAGGAAGAAGAGGAAG

AAGAAGAAGATGCTTCTTCGTGGACGCAAGCTAGTGTTAATGATGATGATGATGTGAGTGATGCGAGGAATGGTGGTGATTC
GTATCGTAGAGAAATACAATCAGCTTCGATGGGTTTTAGGTGTAGAGATACGAATCTAGCGTCACAAGGTGTGTCAAAGATG
AGGAAGAGTAATGTTGGTAGTTGTAAGAAGAAGAGTAAGAAAAAAATTAGCTCTTCTCGTTTGGATTGTTTGTCAAAGTATC
AACCTAGAGATGACATTGTTGCTAGAAATTGTAATGCTGGATCAGATGACAATTGAAA

HDR donor fragment for STI C-terminal Knock-in with mNeonGreen

AAAACTAGTTTCTACCTCAAGAAGACACTTATCGCCAAACTAACGTAGCTTCTGCTATTTCTTCTTCTGGCCTAACCACTCACC
AATGGGTAGATGAGCTAAACAATGAAGTTAAGCTTTTGAAAATCGGCGACAATGGTGAGCTTCAGGAGAATCTAACCGGTAC
AAGAGGACAGCATTGTCCTCTTTCCCCAAGCTTACTTCATGATACTAACTTCGGAAACAACAAAGACAATCTGTAAGTTCCTC
ACTCTGATCCTTTTCGATACAAAACCGAAAAGAAAAAACAAATAAGATCTTTATAATCAACGTATTGTCGTAATGATGTCATG
TTTGGCTTTGGTTGTGTAGAGGAGGATACGAATCAGGATCAGGAAGAGTTGGTTGTAATATATTATTTTGTTGGAACACAAAA
AAGACTCAGAGACGAAGCAAGGTTTGTGCTAATAACTCGAATCTGTTCCTCCTTTTCGATGTTTTCTTTGTCTCATTTGTTTTTC
ATTTGCGGATTTGATTAGTCGAAACAGGTCAAGGGAACTCCTGTTCGTTCGCGGAGAAATCGGAAGAGTCGGTTCTCTCTGT**T**
TAATGGATGTGCTAAACCTAGGAAAGCAGAAGGTAACATTAGAAGA*GGAGGAGGAGGATCTGGAGGAGGAGGATCT*ATGGT
CTCAAAAGGTGAGGAAGATAATATGGCGTCGCTTCCAGCAACTCATGAACTTCACATTTTTGGATCTATCAATGGTGTTGATT
TTGATATGGTTGGTCAAGGTACTGGAAACCCAAATGATGGTTATGAAGAGCTAAACCTCAAGAGCACAAAGGGAGATCTTCA
GTTCTCACCGTGGATTTTAGTACCTCATATTGGGTATGGATTCCATCAATACCTCCCTTATCCTGATGGCATGTCTCCATTTCA
AGCCGCAATGGTGGATGGCTCTGGCTACCAAGTACACCGCACAATGCAGTTTGAAGACGGTGCTTCGCTGACGGTGAACTAT
AGATACACTTATGAGGGATCTCACATCAAAGGAGAAGCTCAAGTCAAAGGGACTGGCTTCCCTGCGGACGGTCCGGTGATGA
CAAACTCCCTTACCGCAGCTGACTGGTGTAGAAGCAAGAAGACGTATCCCAATGACAAGACTATAATATCCACATTCAAATG
GAGTTATACAACCGGGAACGGAAAGCGTTACCGGTCAACAGCACGAACCACCTACACATTTGCTAAACCAATGGCTGCCAAT
TACTTGAAGAACCAGCCTATGTATGTTTTCAGGAAAACGGAGTTAAAACATAGTAAAACTGAGTTGAATTTCAAGGAATGGC
AGAAGGCTTTTACTGATGTTATGGGAATGGATGAGTTGTACAAATAGAACTAAGTTCTTTAGTCATGAAAAACAAAATTGTTC
CCTCAAGCTCTAATTTATCATCTGTTCTTCCACTTCCACATAGTTTTCCCTTAATTATGTTTGATAATGATATGTCAAAGGACA
GTTTTAATATATTCACTGTAAAGTTCCTATCCATTTTTGTTATCTATCTTATAAAAACTTCAAAAATGTTACTGTGAAATAATC
GACGAATTGGTTAACCTTGCACATTAGTTTATATTTTTCAATTTTTTTGTGTTGCATTTGTTGGAAAAATAAATAATATTTATTA
TTTGTGATTTACCTTTTTCAGTTATTGTAATTTTTAGTTTCATATTTACTTGGTTTATGACACATATTGAAACTATTGAAACAAA
TCAAAATTTCTATTGTTAAACTCTTTTCAAGTCTTAAAAAATATTAAAATTTTAAAATGAACAAAAAGGTTATGTAAGTTTTGT
TTCACCTAACTTAAGCGGGGAGATGAAAAGTTGAAAAGTTAGTAAATGTAATAGACCAAAGGGTTTGTCGCGGAGAATAAAT
TATAAAAGAAAACAAACTATAATTTTGCAATTGAAA

Gel electrophoresis of CRISPR/Cas9 knock-in PCR screening

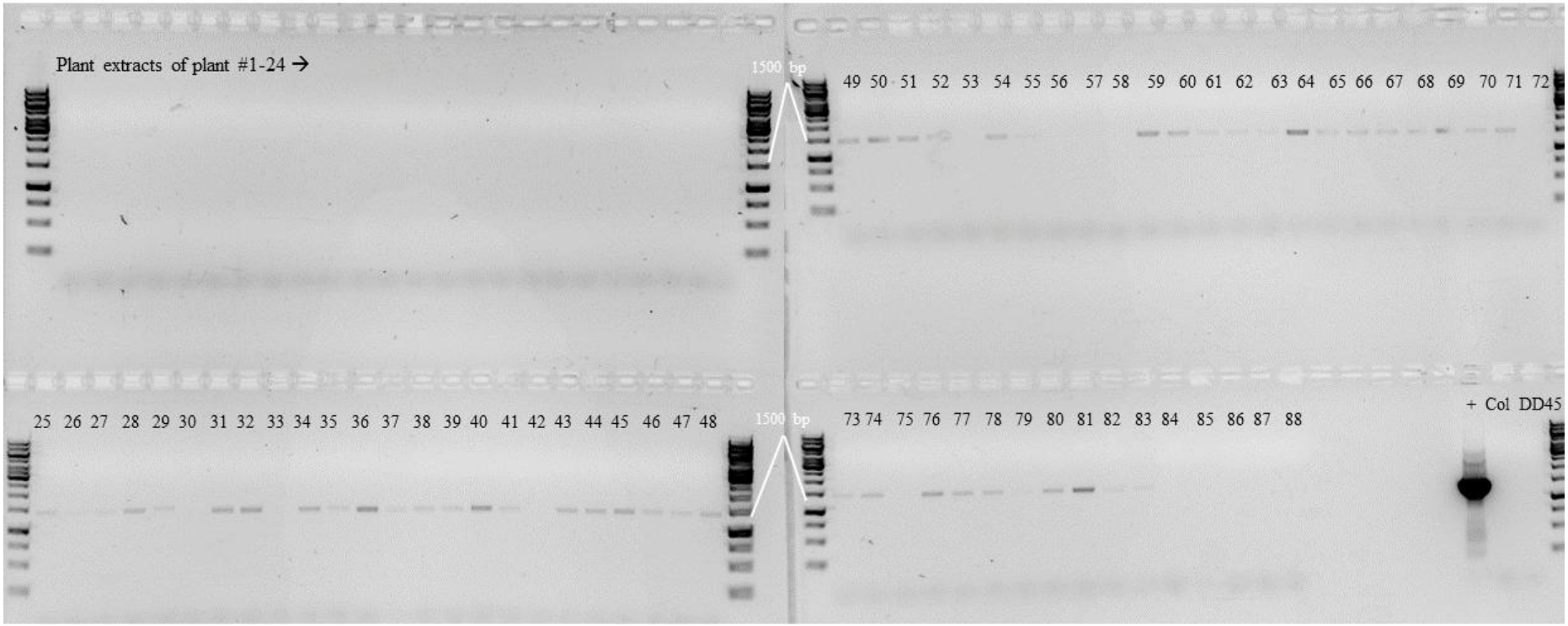

Fig. 37: CRISPR/Cas9 Screening PCR of HY100 in DD45.

Genomic DNA extracts of 178 T2 plants was tested. Plants 24 to 83 belong to a single T1 plant. Plant 89-178 did not show bands (data not shown). Primers L577 (inside tdTomato sequence) and HJ062 (upstream, outside of HDR fragment) confirmed insertion of the transgene at the correct location, shown as bands at the expected size of 1440 bp. The vector HY081 serves as a positive control, Col-0 and DD45 serve as negative controls. Primers were annealed at 60 °C, the elongation step took 90 sec, 30 PCR cycles. The GeneRuler 1 kb DNA ladder was used.

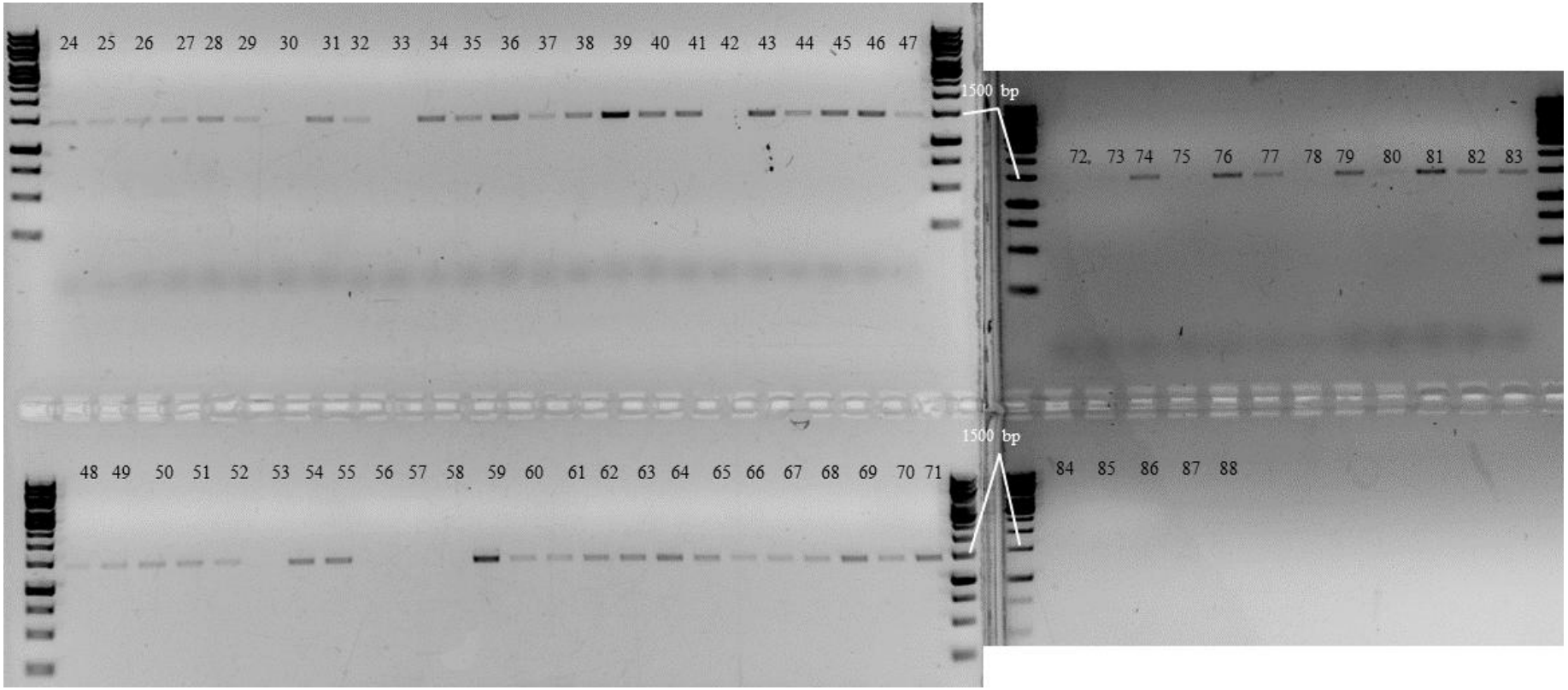

Fig. 38: CRISPR/Cas9 Screening PCR of HY100 in DD45, third PCR to confirm positives.

Genomic DNA extracts of T2 plants was tested. Plants 24 to 83 belong to a single T1 plant. Primers L577 (inside tdTomato sequence) and HJ062 (upstream, outside of HDR fragment) confirmed insertion of the transgene at the correct location, shown as bands at the expected size of 1440 bp. Primers were annealed at 60 °C, the elongation step took 90 sec, 30 PCR cycles. The GeneRuler 1 kb DNA ladder was used.

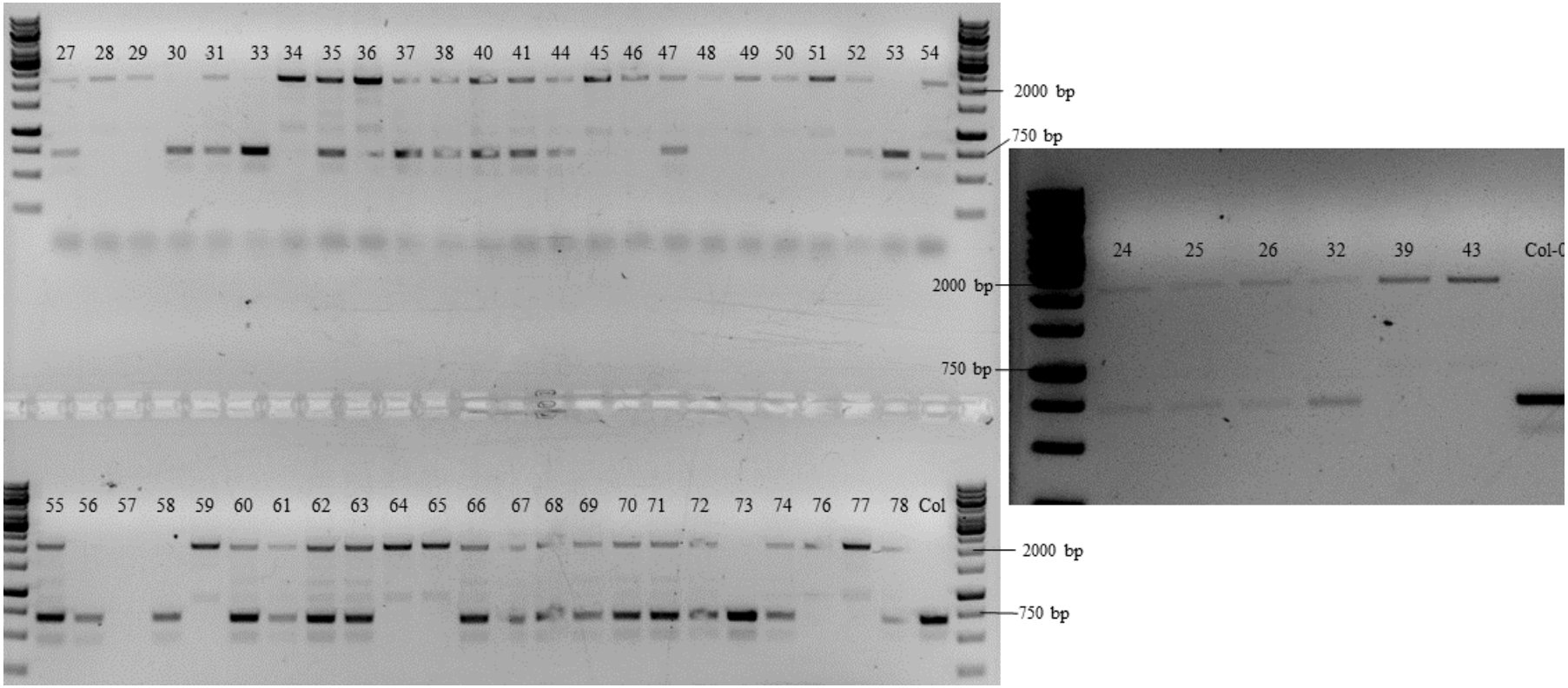

Fig. 39: Gel electrophoresis after PCR to distinguish wild-type and knock-in alleles (full set).

In the wild-type locus, amplification using one primer located upstream of the homology region and one downstream of the target site results in a 728 bp PCR fragment. In the knock-in allele, insertion of the tdTomato sequence increases the distance between primer binding sites, resulting in a 2159 bp PCR fragment. DD45 resembles the parental line and serves as negative control showing the wild type band.

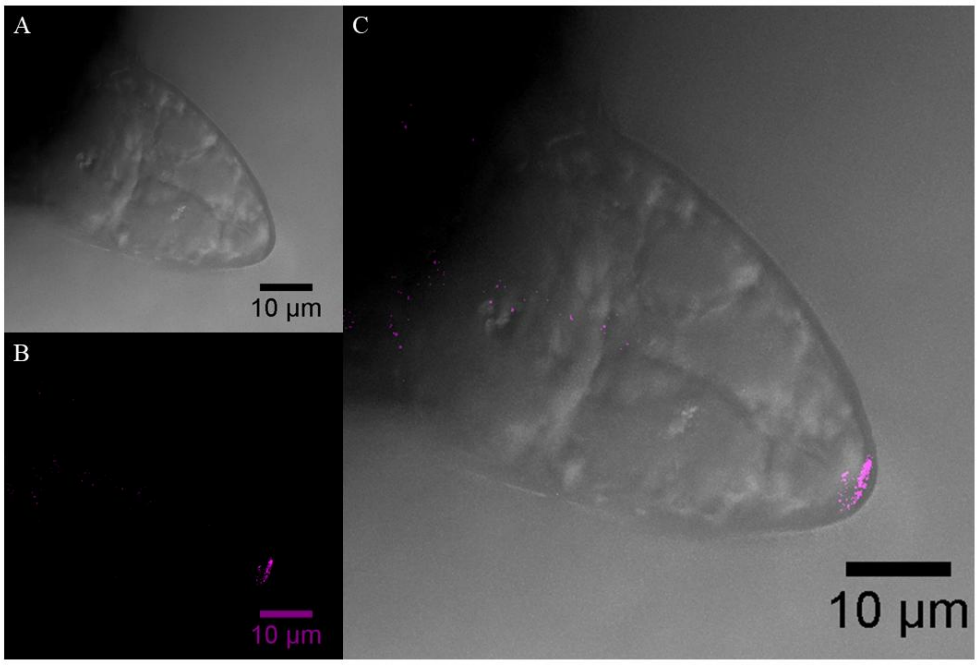

Fig. 40: Weak apical STI-tdTomato **fluorescence detected in T1 plants generated by CRISPR/Cas9-mediated knock-in. Additional Fig. 1**

Confocal microscopy of epidermal outgrowth structures in T1 plants carrying the endogenous STI-tdTomato knock-in construct. A Brightfield image. B tdTomato fluorescence C Merged image. Weak fluorescence signals were predominantly detected at the apical region of the developing structure. Scale bars = 10 µm.

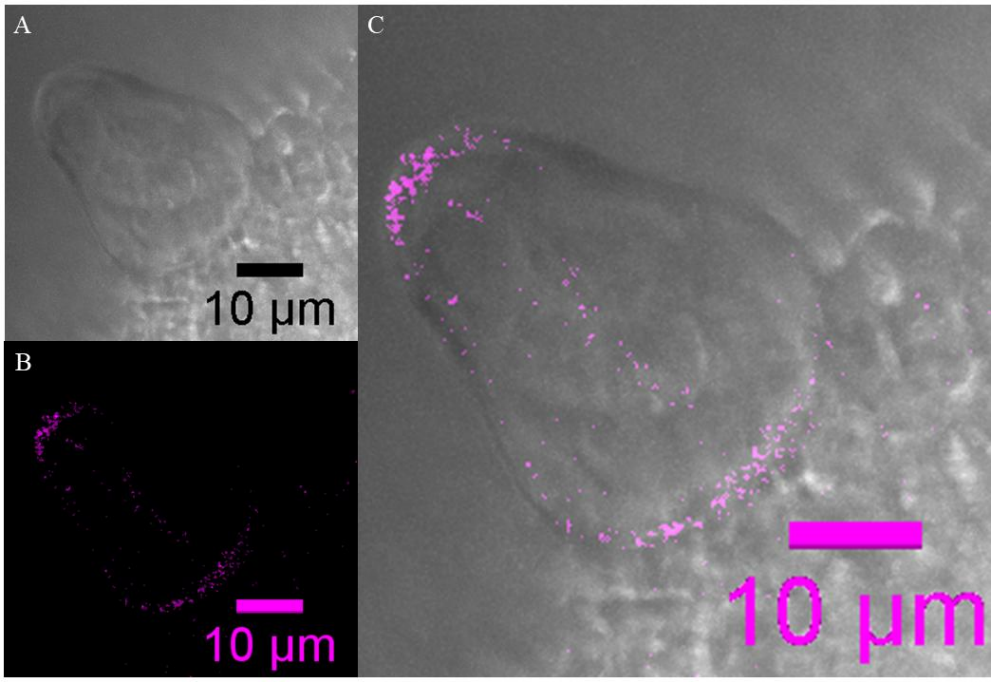

Fig. 41: Weak apical STI-tdTomato **fluorescence detected in T1 plants generated by CRISPR/Cas9-mediated knock-in. Additional Fig. 2**

Confocal microscopy of epidermal outgrowth structures in T1 plants carrying the endogenous STI-tdTomato knock-in construct. A Brightfield image. B tdTomato fluorescence C Merged image. Weak fluorescence signals were detected at the apical region of the developing structure as well as at the base. Scale bars = 10 µm.

Yeast two-hybrid additional data

Tab. 16: NET1 fragments designed for yeast-two-hybrid interaction studies.
Exact positions of the CDS. Note that the C-terminal 3 fragment as well as the full C-terminal fragment of NET1A contains an intron of 170 bp. Furthermore, fragment NET1D C-terminal full length was excluded from the analysis because repeated cloning attempts were unsuccessful.

Position in CDS (bp)	Fragment
1-317	NET1A NAB domain
318-5187	NET1A C-terminal full length
318-1728	NET1A C-terminal 1
1716-3638	NET1A C-terminal 2
3625-5187	NET1A C-terminal 3
1-319	NET1B NAB domain
320-5133	NET1B C-terminal full length
320-1582	NET1B C-terminal 1
1573-3466	NET1B C-terminal 2

Position in CDS (bp)	Fragment
3458-5133	NET1B C-terminal 3
1-321	NET1C NAB domain
321-3336	NET1C C-terminal full length
321-1484	NET1C C-terminal 1
1475-2241	NET1C C-terminal 2
2230-3336	NET1C C-terminal 3
1-318	NET1D NAB domain
319-3456	NET1D C-terminal full length
319-1391	NET1D C-terminal 1
1392-2385	NET1D C-terminal 2
2378-3456	NET1D C-terminal 3

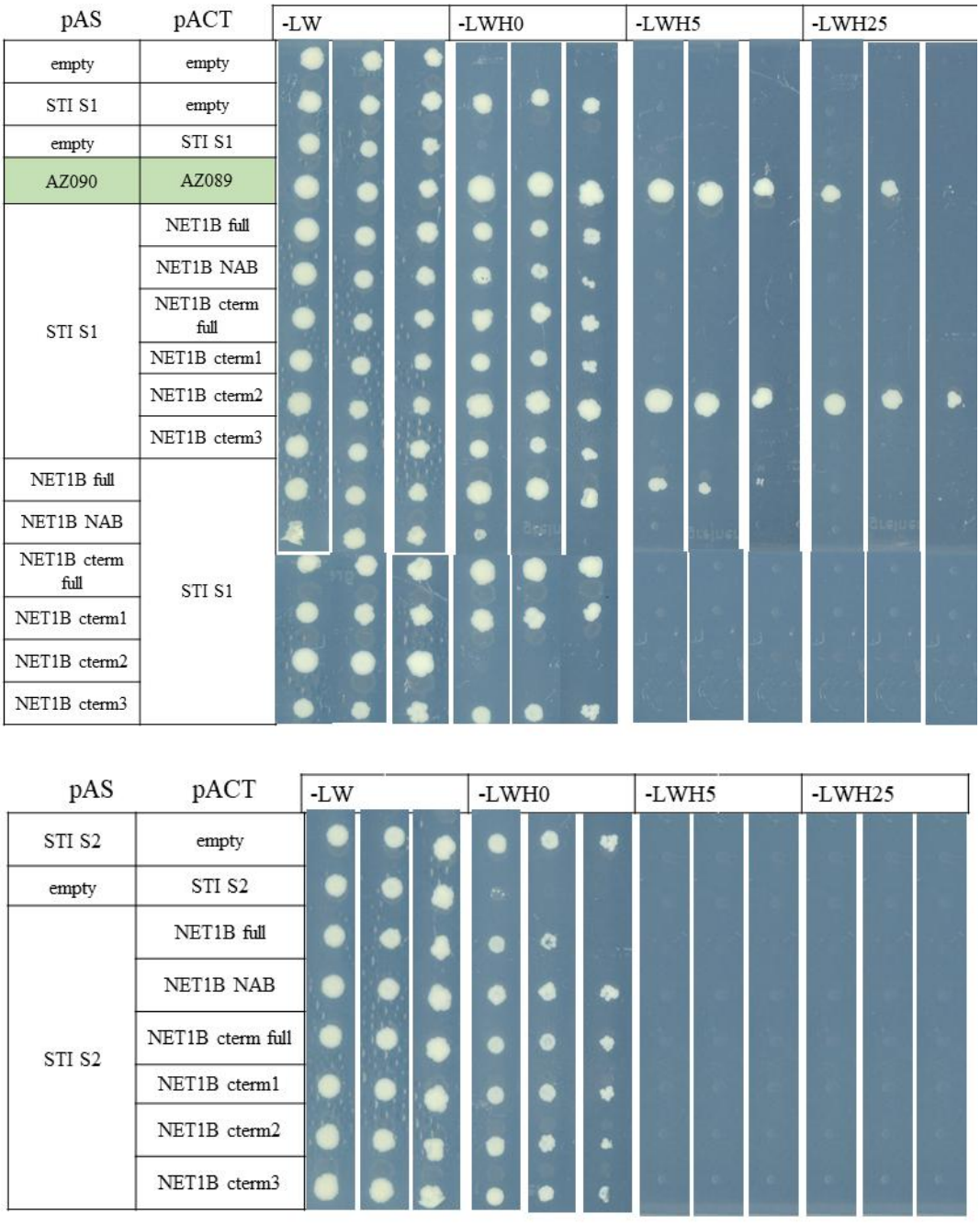

Fig. 42: Set 1: Yeast two-hybrid analysis of interactions between STI S1 and STI S2 with NET1B protein fragments.

Yeast growth was assessed on selective media lacking leucine and tryptophan (-LW), as well as on increasingly stringent interaction-selective media lacking leucine, tryptophan and histidine supplemented with increasing concentrations of 3-amino-1,2,4-triazole (3-AT) (-LWH0, -LWH5, -LWH25). Only growth on media containing 3-AT was considered as positive interaction. Growth on selective media was observed predominantly for NET1B cterm2 and the full length NET1B, indicating interaction with STI S1. STI S2 did not show detectable interaction with NET1B fragments under the tested conditions. Empty vector combinations served as negative controls. The interaction between SNF1 (AZ089) and SNF4 (AZU089) served as positive control (green).

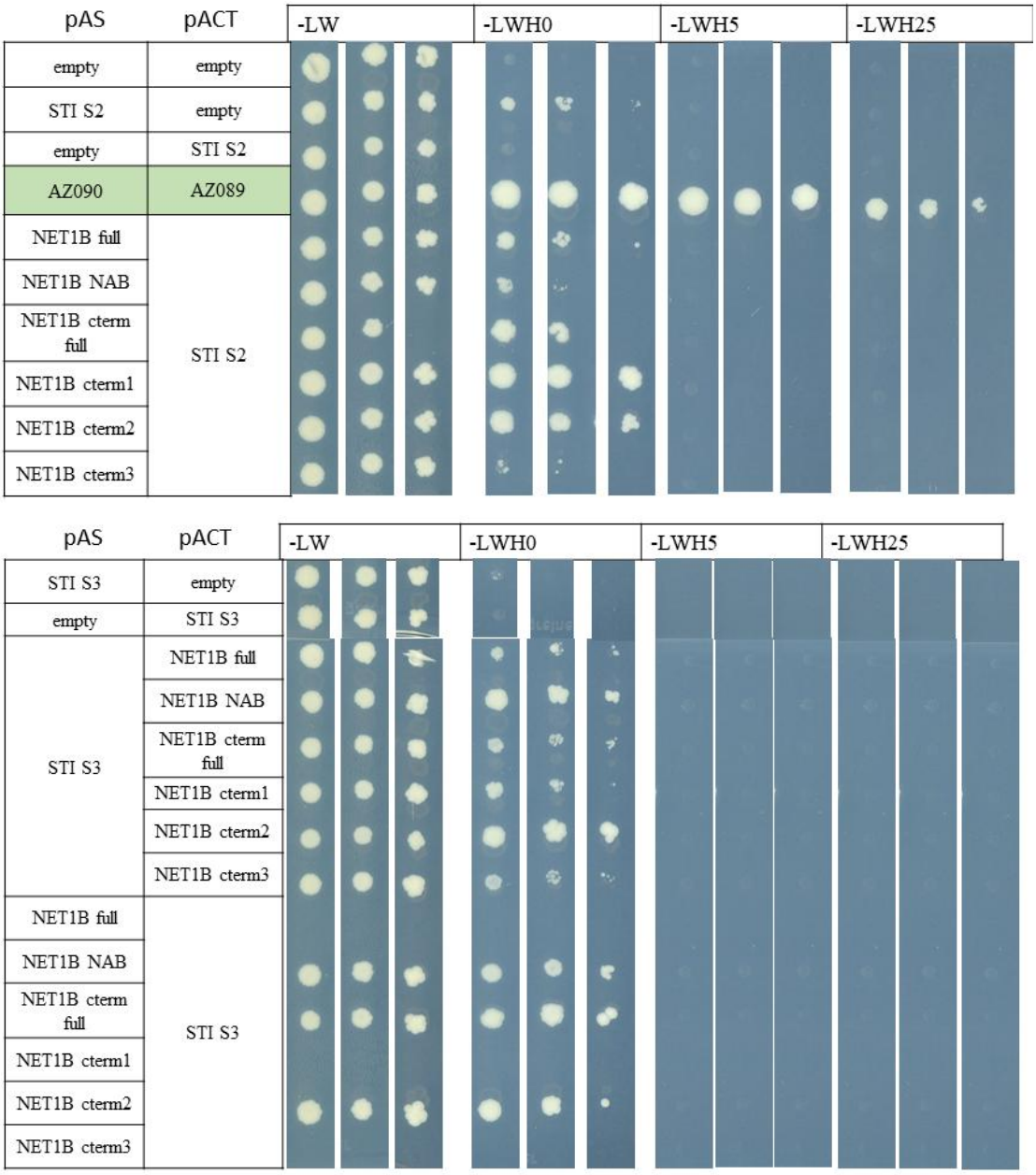

Fig. 43: Set 2: Yeast two-hybrid analysis of interactions between STI S2 and STI S3 with NET1B protein fragments.

Yeast growth was assessed on selective media lacking leucine and tryptophan (-LW), as well as on increasingly stringent interaction-selective media lacking leucine, tryptophan and histidine supplemented with increasing concentrations of 3-amino-1,2,4-triazole (3-AT) (-LWH0, -LWH5, -LWH25). Only growth on media containing 3-AT was considered as positive interaction. No detectable interaction with NET1B fragments under the tested conditions were observed. NET1B full, cterm1 and cterm3 interaction with STI S3 was repeated in Set 9. Empty vector combinations served as negative controls. The interaction between SNF1 (AZ090) and SNF4 (AZ089) served as positive control (green).

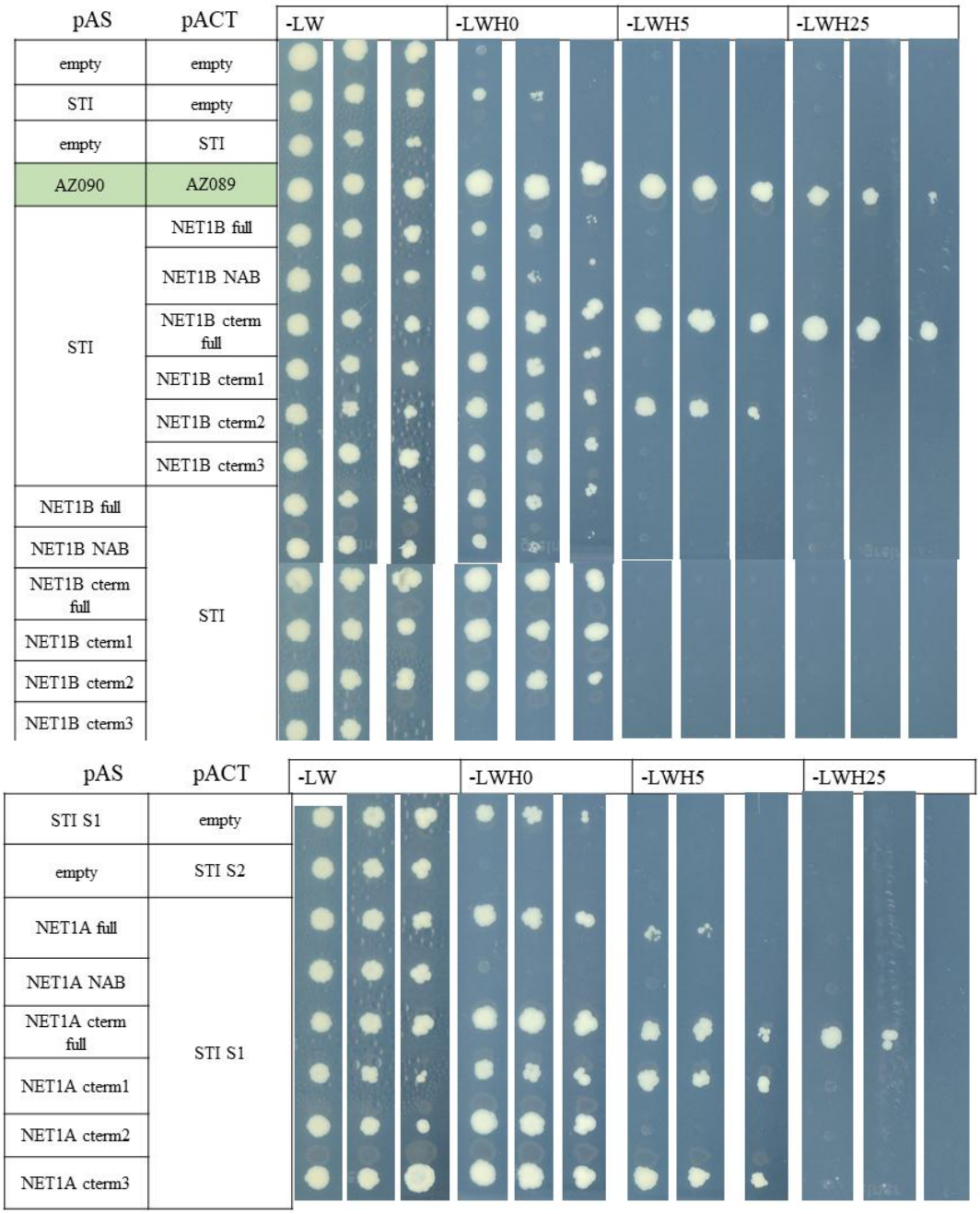

Fig. 44: Set 3: Yeast two-hybrid analysis of interactions between full-length STI or STI S1 and NET1A and NET1B protein fragments.

Yeast growth was assessed on selective media lacking leucine and tryptophan (-LW), as well as on increasingly stringent interaction-selective media lacking leucine, tryptophan and histidine supplemented with increasing concentrations of 3-amino-1,2,4-triazole (3-AT) (-LWH0, -LWH5, -LWH25). Only growth on media containing 3-AT was considered as positive interaction. Full-length STI showed interaction-dependent growth predominantly with the complete NET1B C-terminal region (cterm full), and NET1B cterm2 fragments. STI S1 showed interaction with the complete NET1A C-terminal region, and with the NET1A cterm1 and cterm3 fragment. Empty vector combinations served as negative controls. The interaction between SNF1 (AZ090) and SNF4 (AZ089) served as positive control (green).

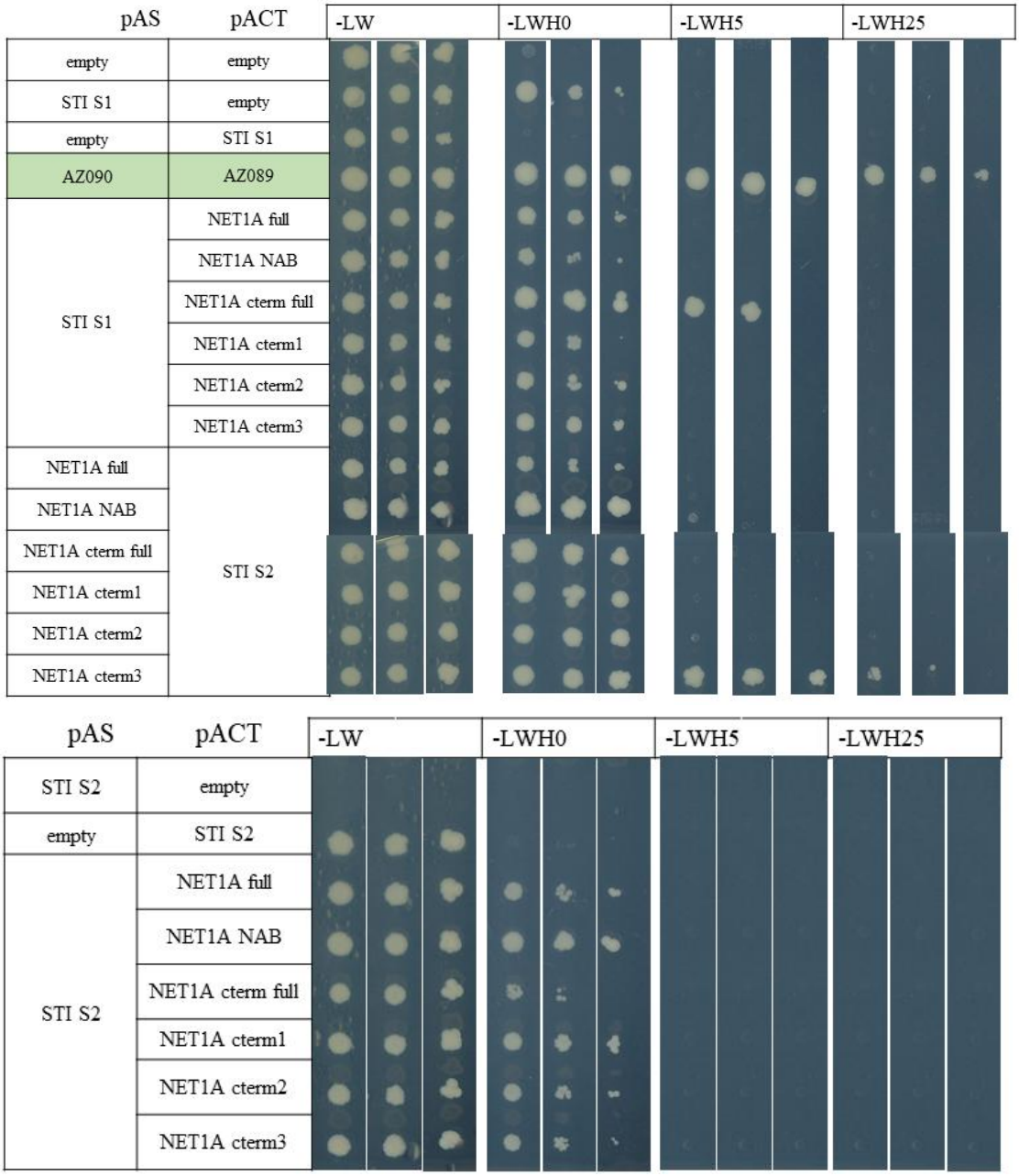

Fig. 45: Set 4: Yeast two-hybrid analysis of interactions between STI S1 and STI S2 with NET1A protein fragments.

Yeast growth was assessed on selective media lacking leucine and tryptophan (-LW), as well as on increasingly stringent interaction-selective media lacking leucine, tryptophan and histidine supplemented with increasing concentrations of 3-amino-1,2,4-triazole (3-AT) (-LWH0, -LWH5, -LWH25). Only growth on media containing 3-AT was considered as positive interaction. Growth on selective media was observed predominantly for the complete NET1A C-terminal region (cterm full) with STI S1 and the NET1A cterm3 fragment in combination with STI S2. Empty vector combinations served as negative controls. The interaction between SNF1 (AZ090) and SNF4 (AZ089) served as positive control (green).

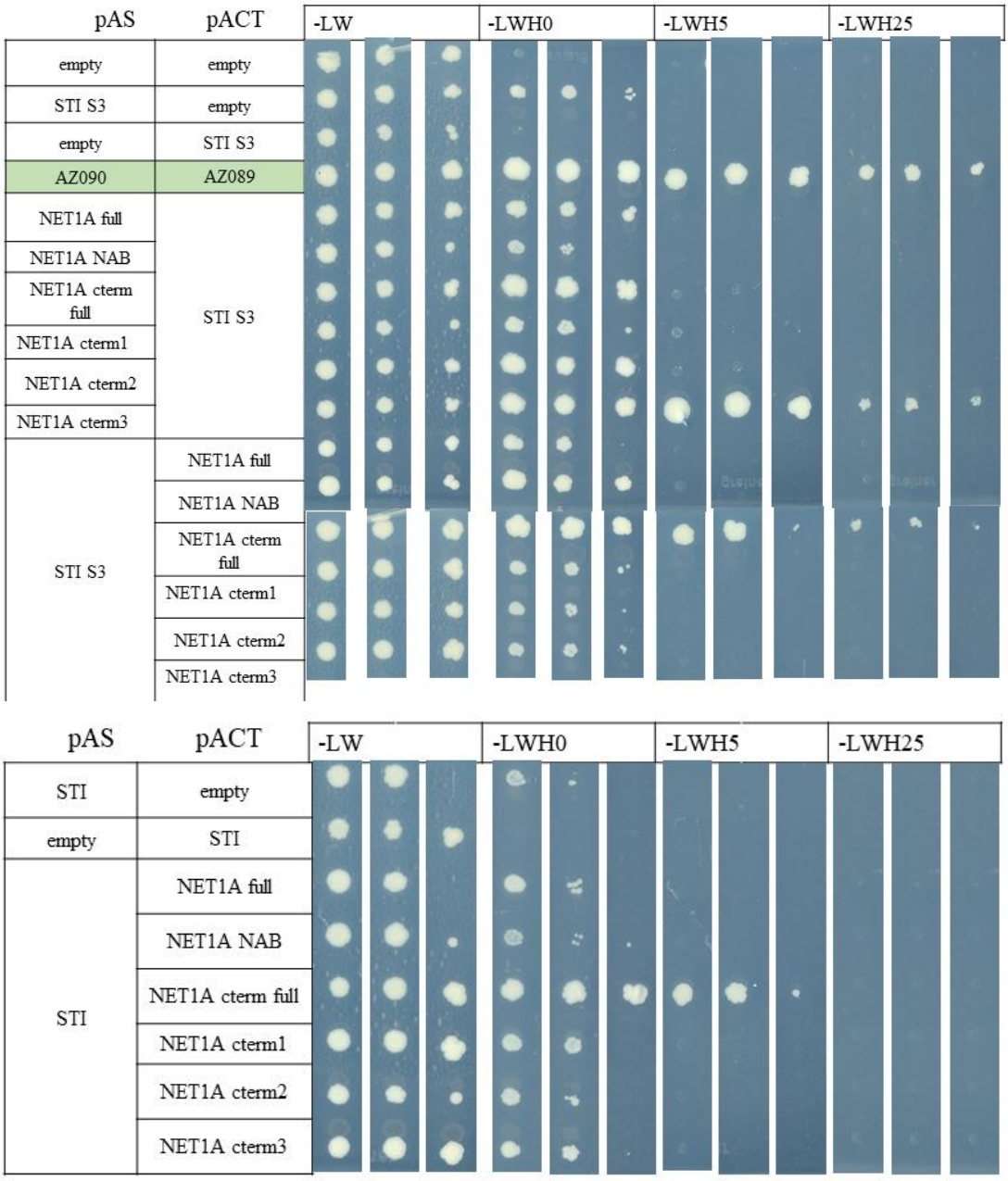

Fig. 46: Set 5: Yeast two-hybrid analysis of interactions between STI S3 or full-length STI and NET1A protein fragments.

Yeast growth was assessed on selective media lacking leucine and tryptophan (-LW), as well as on increasingly stringent interaction-selective media lacking leucine, tryptophan and histidine supplemented with increasing concentrations of 3-amino-1,2,4-triazole (3-AT) (-LWH0, -LWH5, -LWH25). Only growth on media containing 3-AT was considered as positive interaction. STI S3 showed interaction-dependent growth predominantly with the NET1A cterm3 fragment and the full length C-terminal fragment. Full-length STI also showed detectable interaction with the complete NET1A C-terminal region, Empty vector combinations served as negative controls. The interaction between SNF1 (AZ090) and SNF4 (AZ089) served as positive control (green).

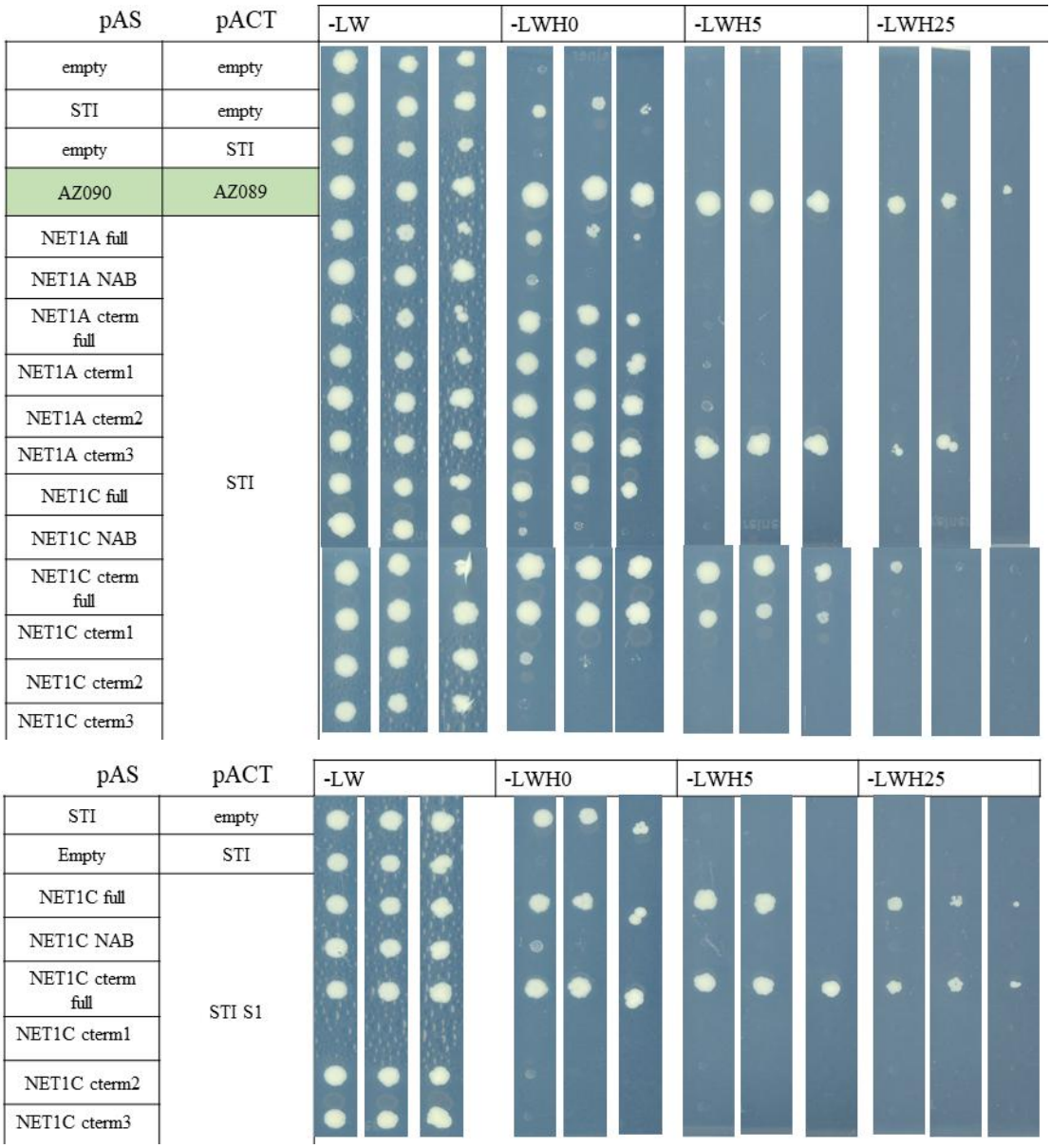

Fig. 47: Set 6: Yeast two-hybrid analysis of interactions between full-length STI or STI S1 and NET1A and NET1C protein fragments.

Yeast growth was assessed on selective media lacking leucine and tryptophan (-LW), as well as on increasingly stringent interaction-selective media lacking leucine, tryptophan and histidine supplemented with increasing concentrations of 3-amino-1,2,4-triazole (3-AT) (-LWH0, -LWH5, -LWH25). Only growth on media containing 3-AT was considered as positive interaction. Full-length STI showed interaction-dependent growth with NET1A cterm3, NET1C cterm full and NET1C cterm1. STI S1 showed interaction with NET1C cterm full and the full length NET1C. **NET1C cterm2 and NET1C cterm3 initially contained frameshift mutations and were therefore re-cloned and re-tested separately in Set 14.** NET1C cterm1 interaction with STI S1 was repeated in Set 10 Empty vector combinations served as negative controls. The interaction between SNF1 (AZ090) and SNF4 (AZ089) served as positive control (green).

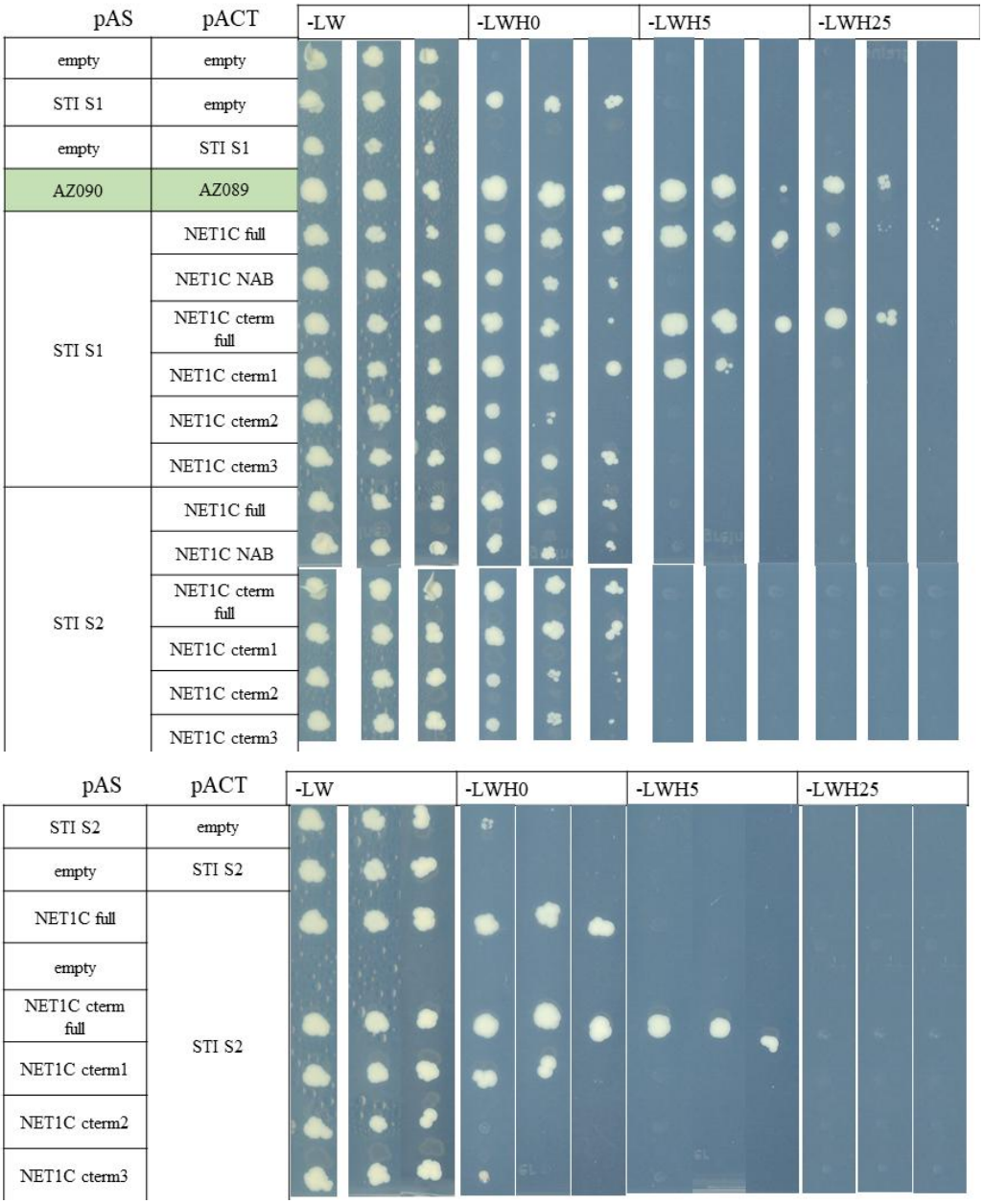

Fig. 48: Set 7: Yeast two-hybrid analysis of interactions between STI S1 and STI S2 with NET1C protein fragments.

Yeast growth was assessed on selective media lacking leucine and tryptophan (-LW), as well as on interaction-selective media lacking leucine, tryptophan and histidine supplemented with increasing concentrations of 3-amino-1,2,4-triazole (3-AT) (-LWH0, -LWH5, -LWH25). Only growth on media containing 3-AT was considered as positive interaction. STI S1 showed interaction-dependent growth with full-length NET1C, the complete NET1C C-terminal region (cterm full), and the NET1C cterm1 fragment. STI S2 similarly showed interaction with the complete NET1C C-terminal region, **NET1C cterm2 and NET1C cterm3 initially contained frameshift mutations and were therefore re-cloned and re-tested separately in Set 14.** NET1C NAB interaction with STI S2 was repeated in Set 10 Empty vector combinations served as negative controls. The interaction between SNF1 (AZ090) and SNF4 (AZ089) served as positive control (green).

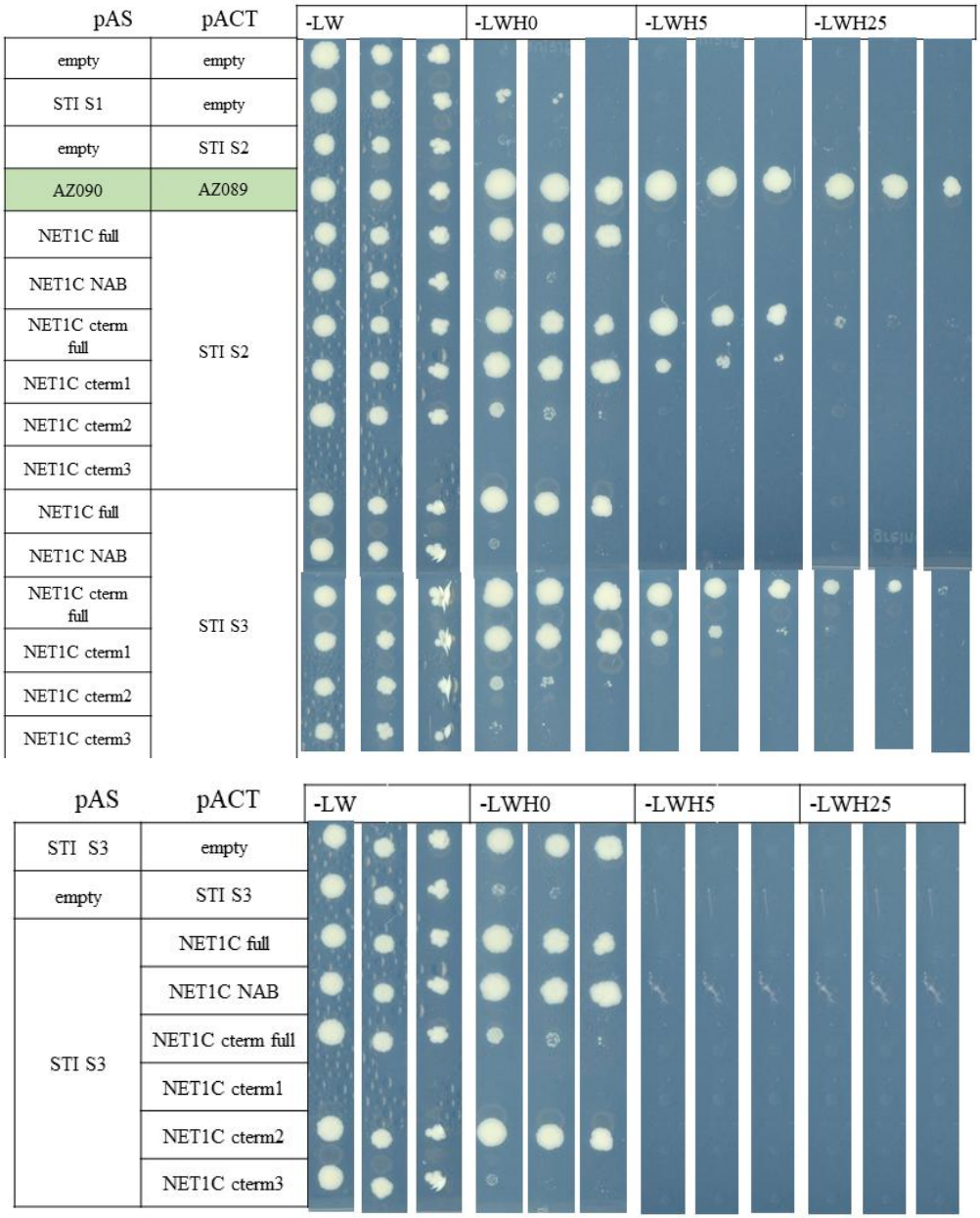

Fig. 49: Set 8: Yeast two-hybrid analysis of interactions between STI S2 and STI S3 with NET1C protein fragments.

Yeast growth was assessed on selective media lacking leucine and tryptophan (-LW), as well as on interaction-selective media lacking leucine, tryptophan and histidine supplemented with increasing concentrations of 3-amino-1,2,4-triazole (3-AT) (-LWH0, -LWH5, -LWH25). Only growth on media containing 3-AT was considered as positive interaction. STI S2 showed interaction-dependent growth with the complete NET1C C-terminal region (cterm full), and NET1C cterm1. In contrast, STI S3 did not show detectable interaction with NET1C fragments under increased selection stringency. **NET1C cterm2 and NET1C cterm3 initially contained frameshift mutations and were therefore re-cloned and re-tested separately in Set 14. NET1C cterm3 interaction with STI S2 was repeated in Set 10** Empty vector combinations served as negative controls. The interaction between SNF1 (AZ090) and SNF4 (AZ089) served as positive control (green).

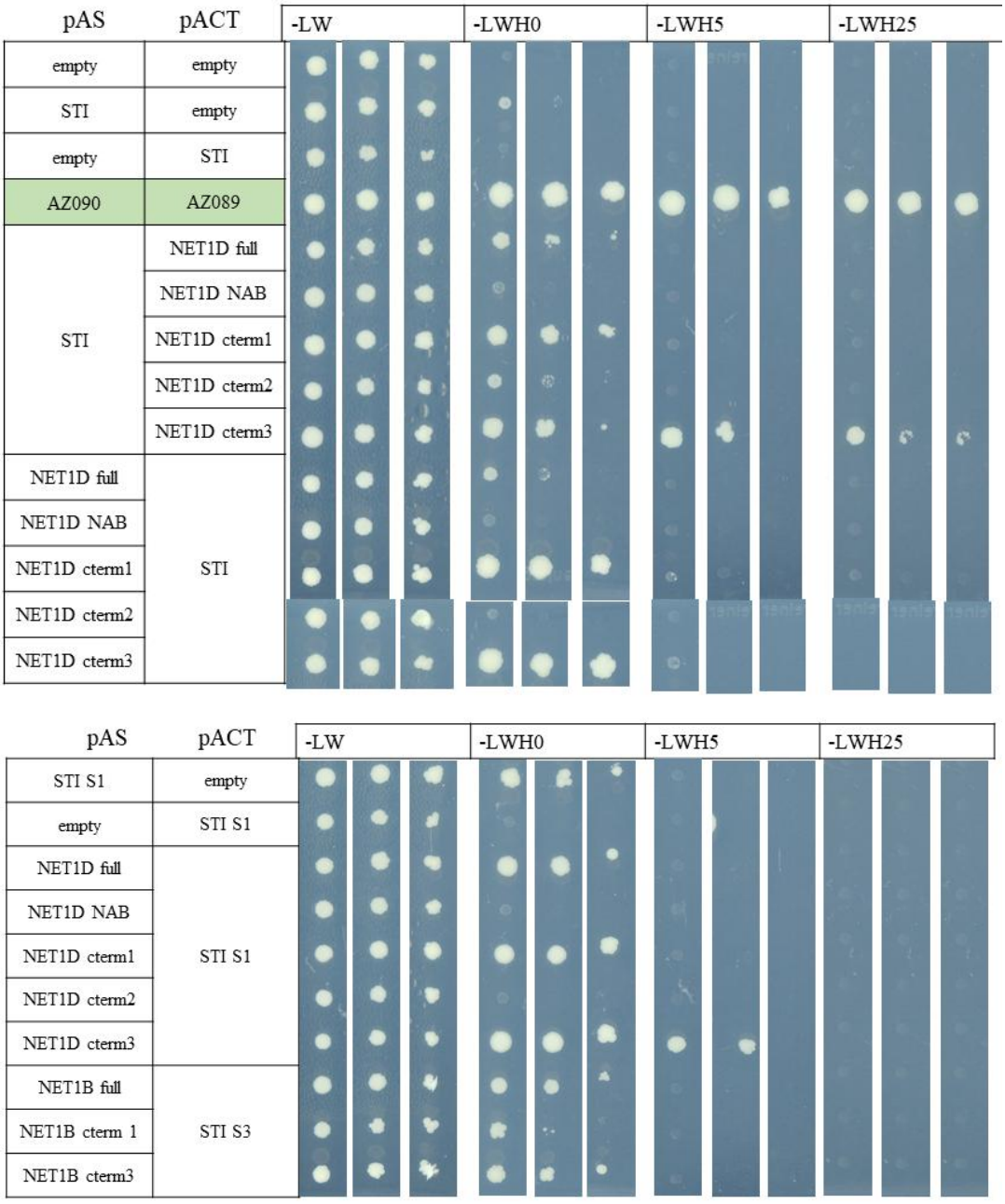

Fig. 50: Set 9: Yeast two-hybrid analysis of interactions between full-length STI and STI S1 protein fragments.

Yeast growth was assessed on selective media lacking leucine and tryptophan (-LW), as well as on interaction-selective media lacking leucine, tryptophan and histidine supplemented with increasing concentrations of 3-amino-1,2,4-triazole (3-AT) (-LWH0, -LWH5, -LWH25). Only growth on media containing 3-AT was considered as positive interaction. Full-length STI showed interaction-dependent growth with full-length NET1D and the NET1D cterm3 fragment. STI S1 similarly interacted with NET1D cterm3. Additionally, the three NET1B C-terminal subfragments that could not be tested successfully in previous sets due to failed yeast transformations were tested with STI S3 and likewise did not show detectable interaction under the tested conditions. Empty vector combinations served as negative controls. The interaction between SNF1 (AZ090) and SNF4 (AZ089) served as positive control (green).

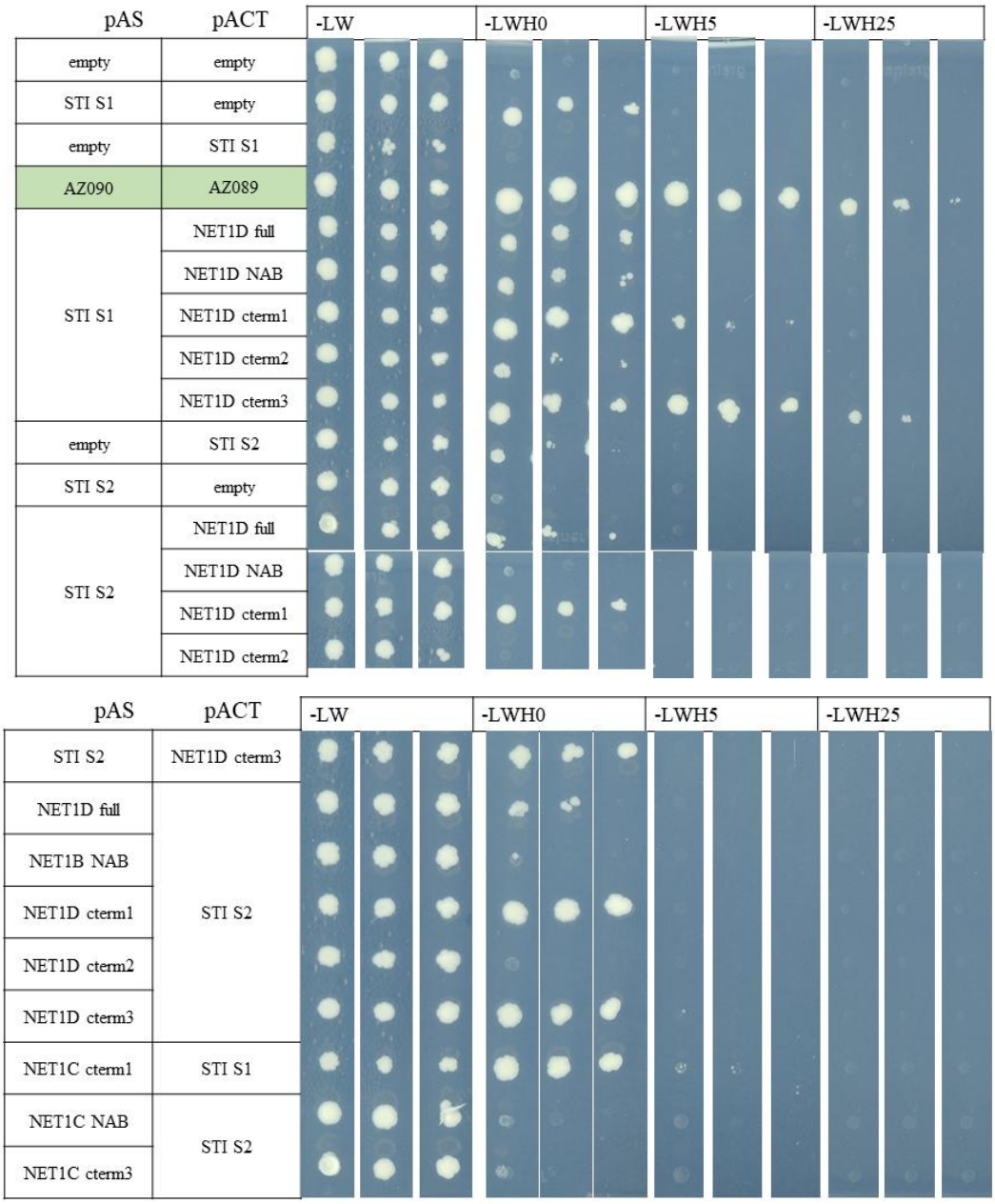

Fig. 51: Set 10: Yeast two-hybrid analysis of interactions between STI S1 and STI S2 with NET1D and NET1C protein fragments.

Yeast growth was assessed on selective media lacking leucine and tryptophan (-LW), as well as on interaction-selective media lacking leucine, tryptophan and histidine supplemented with increasing concentrations of 3-amino-1,2,4-triazole (3-AT) (-LWH0, -LWH5, -LWH25). Only growth on media containing 3-AT was considered as positive interaction. STI S1 showed interaction-dependent growth with NET1D cterm1 and cterm3 fragments. Selected NET1C interactions were additionally repeated due to failed yeast transformations in previous experiments, including NET1C cterm1 with STI S1 (originally tested in Set 6), NET1C NAB with STI S2 (Set 7), and NET1C cterm3 with STI S2 (Set 8). These repeated experiments did not reveal detectable interaction under the tested conditions. Empty vector combinations served as negative controls. The interaction between SNF1 (AZ090) and SNF4 (AZ089) served as positive control (green).

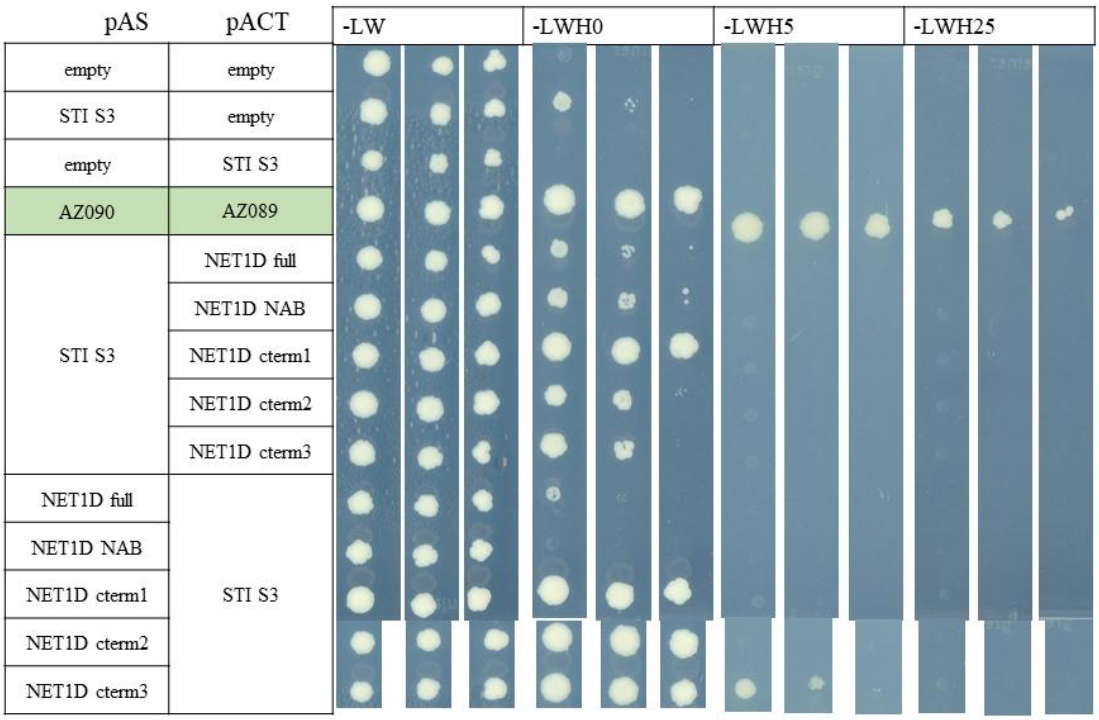

Fig. 52: Set 11: Yeast two-hybrid analysis of interactions between STI S3 and NET1D protein fragments.

Yeast growth was assessed on selective media lacking leucine and tryptophan (-LW), as well as on interaction-selective media lacking leucine, tryptophan and histidine supplemented with increasing concentrations of 3-amino-1,2,4-triazole (3-AT) (-LWH0, -LWH5, -LWH25). Only growth on media containing 3-AT was considered as positive interaction. STI S3 showed interaction-dependent growth with NET1D cterm3 fragment. Empty vector combinations served as negative controls. The interaction between SNF1 (AZ090) and SNF4 (AZ089) served as positive control (green).

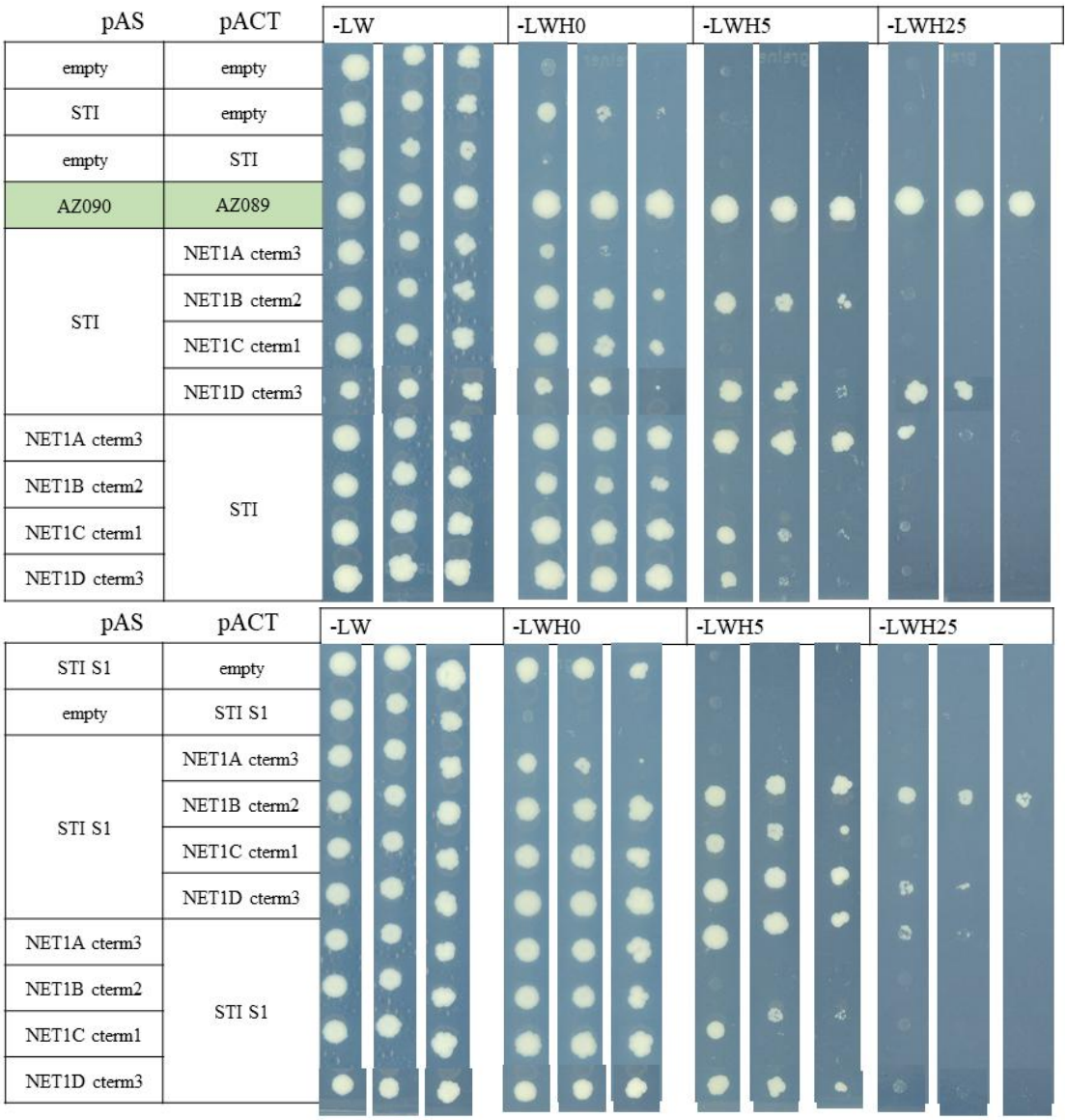

Fig. 53: Set12.1: Reproducibility analysis of selected STI interactions with NET1-derived C-terminal fragments using independent yeast two-hybrid experiments.

Yeast growth was assessed on selective media lacking leucine and tryptophan (-LW), as well as on interaction-selective media lacking leucine, tryptophan and histidine supplemented with increasing concentrations of 3-amino-1,2,4-triazole (3-AT) (-LWH0, -LWH5, -LWH25). Only growth on media containing 3-AT was considered as positive interaction. Full length STI interacted with NET1B cterm2, NET1A cterm3 and NET1D cterm3. STI S1 interacted with all tested subfragments. Interaction was sometimes orientation-dependent. Empty vector combinations served as negative controls. The interaction between SNF1 (AZ090) and SNF4 (AZ089) served as positive control (green).

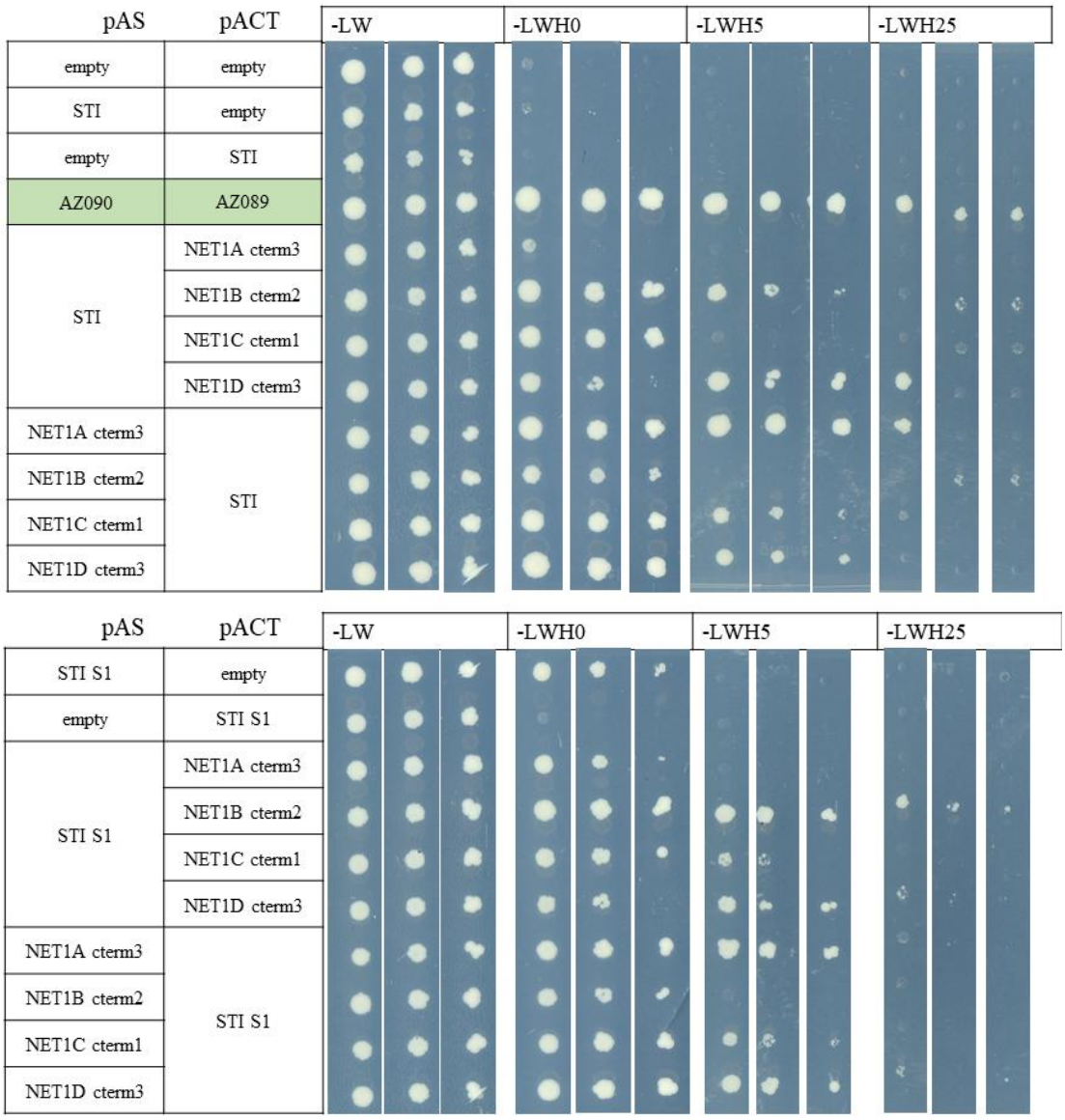

Fig. 54: Set12.2: Reproducibility analysis of selected STI interactions with NET1-derived C-terminal fragments using independent yeast two-hybrid experiments.

Yeast growth was assessed on selective media lacking leucine and tryptophan (-LW), as well as on interaction-selective media lacking leucine, tryptophan and histidine supplemented with increasing concentrations of 3-amino-1,2,4-triazole (3-AT) (-LWH0, -LWH5, -LWH25). Only growth on media containing 3-AT was considered as positive interaction. Full length STI interacted with NET1B cterm2, NET1A cterm3 and NET1D cterm3. STI S1 interacted with all tested subfragments. Interaction was sometimes orientation-dependent. Empty vector combinations served as negative controls. The interaction between SNF1 (AZ090) and SNF4 (AZ089) served as positive control (green).

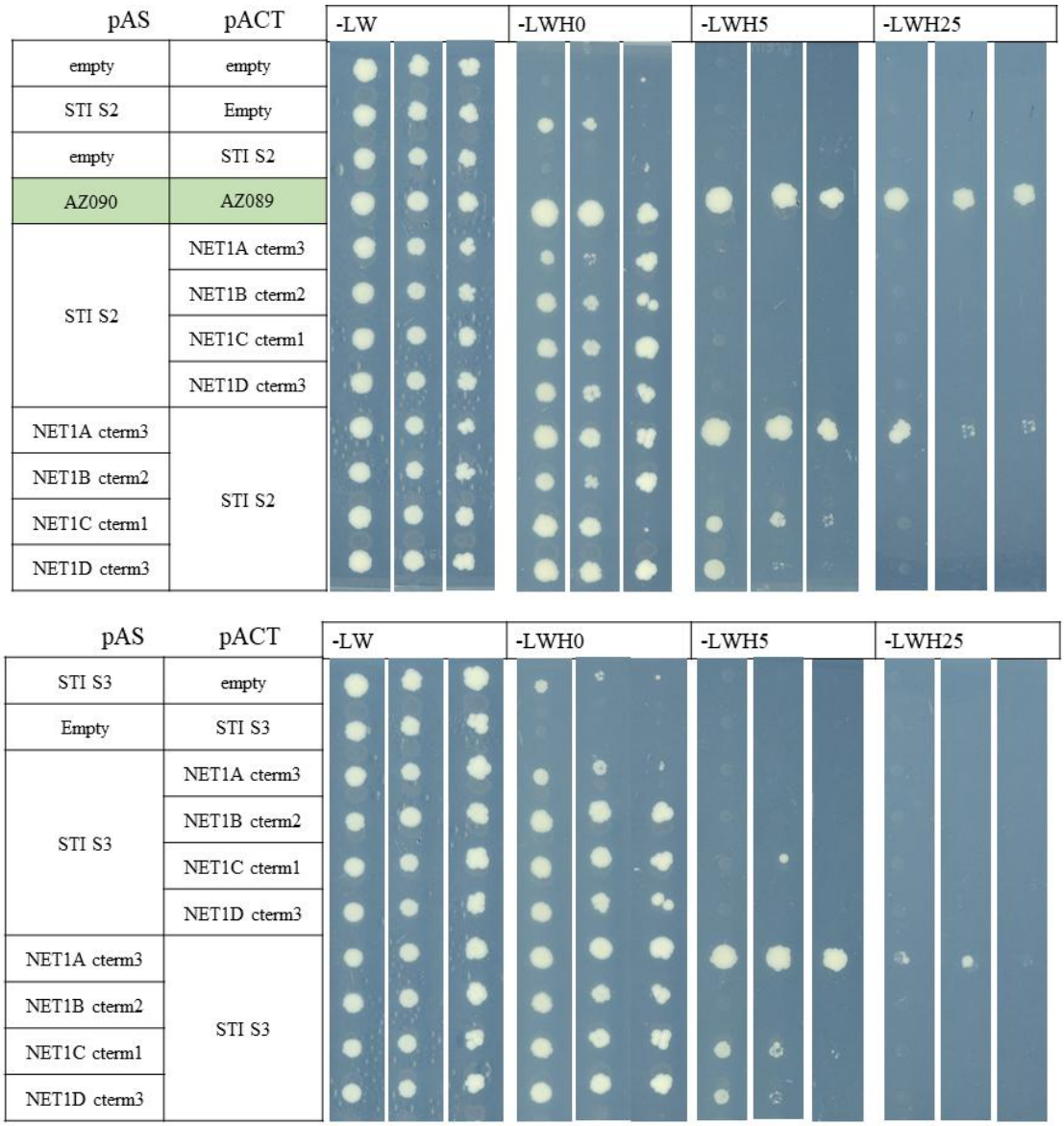

Fig. 55: Set 13.1: Reproducibility analysis of interactions between STI S2 or STI S3 and selected NET1-derived C-terminal fragments using independent yeast two-hybrid experiments.

Yeast growth was assessed on selective media lacking leucine and tryptophan (-LW), as well as on interaction-selective media lacking leucine, tryptophan and histidine supplemented with increasing concentrations of 3-amino-1,2,4-triazole (3-AT) (-LWH0, -LWH5, -LWH25). Only growth on media containing 3-AT was considered as positive interaction. STI S2 interacted orientation-dependently with NET1A cterm3, NET1C cterm1 and NET1D cterm3. STI S3 interacted orientation-dependently with NET1A cterm3, NET1C cterm1 and NET1D cterm3. Empty vector combinations served as negative controls. The interaction between SNF1 (AZ090) and SNF4 (AZ089) served as positive control (green).

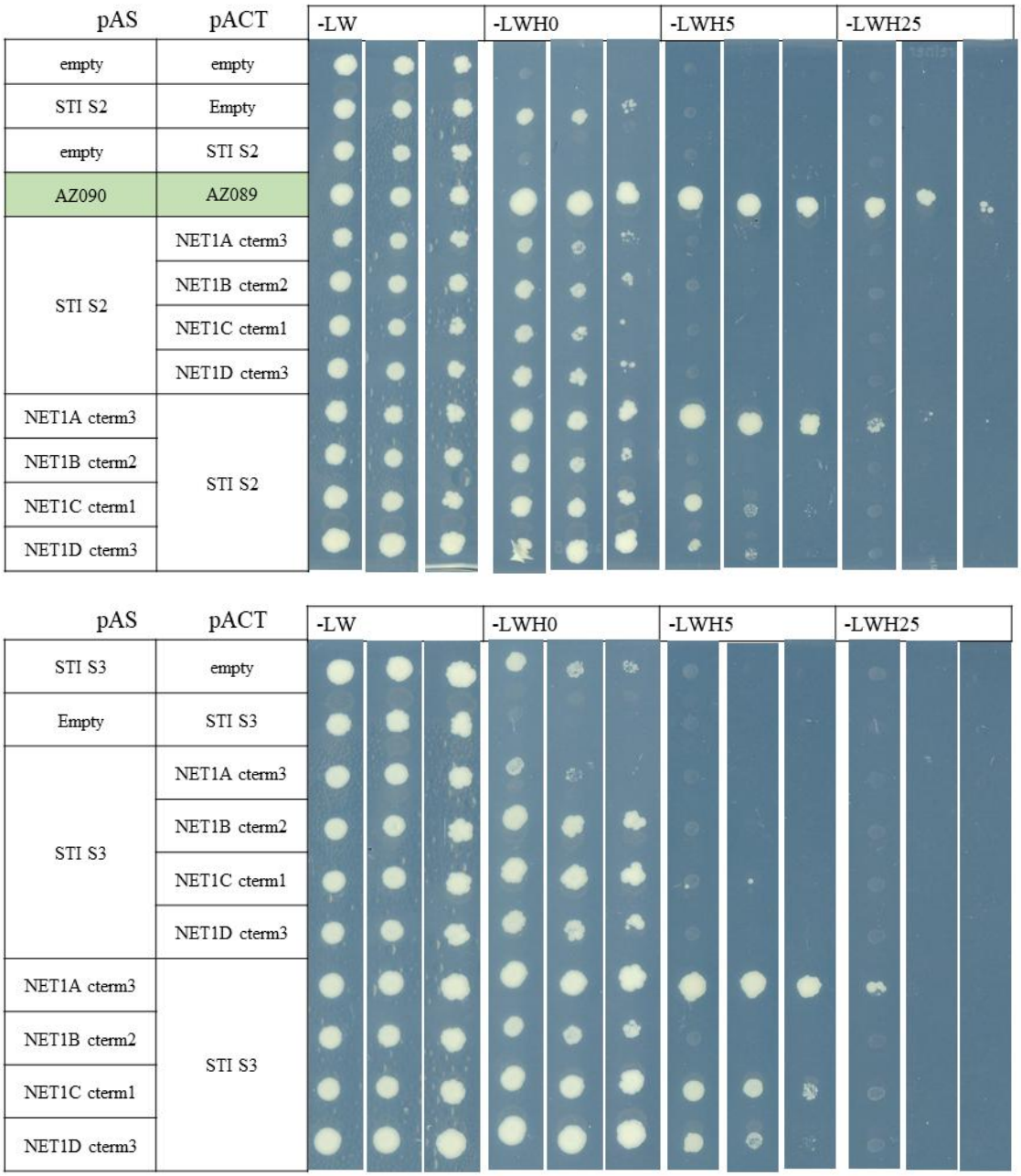

Fig. 56: Set 13.2: Reproducibility analysis of interactions between STI S2 or STI S3 and selected NET1-derived C-terminal fragments using independent yeast two-hybrid experiments.

Yeast growth was assessed on selective media lacking leucine and tryptophan (-LW), as well as on interaction-selective media lacking leucine, tryptophan and histidine supplemented with increasing concentrations of 3-amino-1,2,4-triazole (3-AT) (-LWH0, -LWH5, -LWH25). Only growth on media containing 3-AT was considered as positive interaction. STI S2 interacted orientation-dependently with NET1A cterm3, NET1C cterm1 and NET1D cterm3. STI S3 interacted orientation-dependently with NET1A cterm3, NET1C cterm1 and NET1D cterm3. Empty vector combinations served as negative controls. The interaction between SNF1 (AZ090) and SNF4 (AZ089) served as positive control (green).

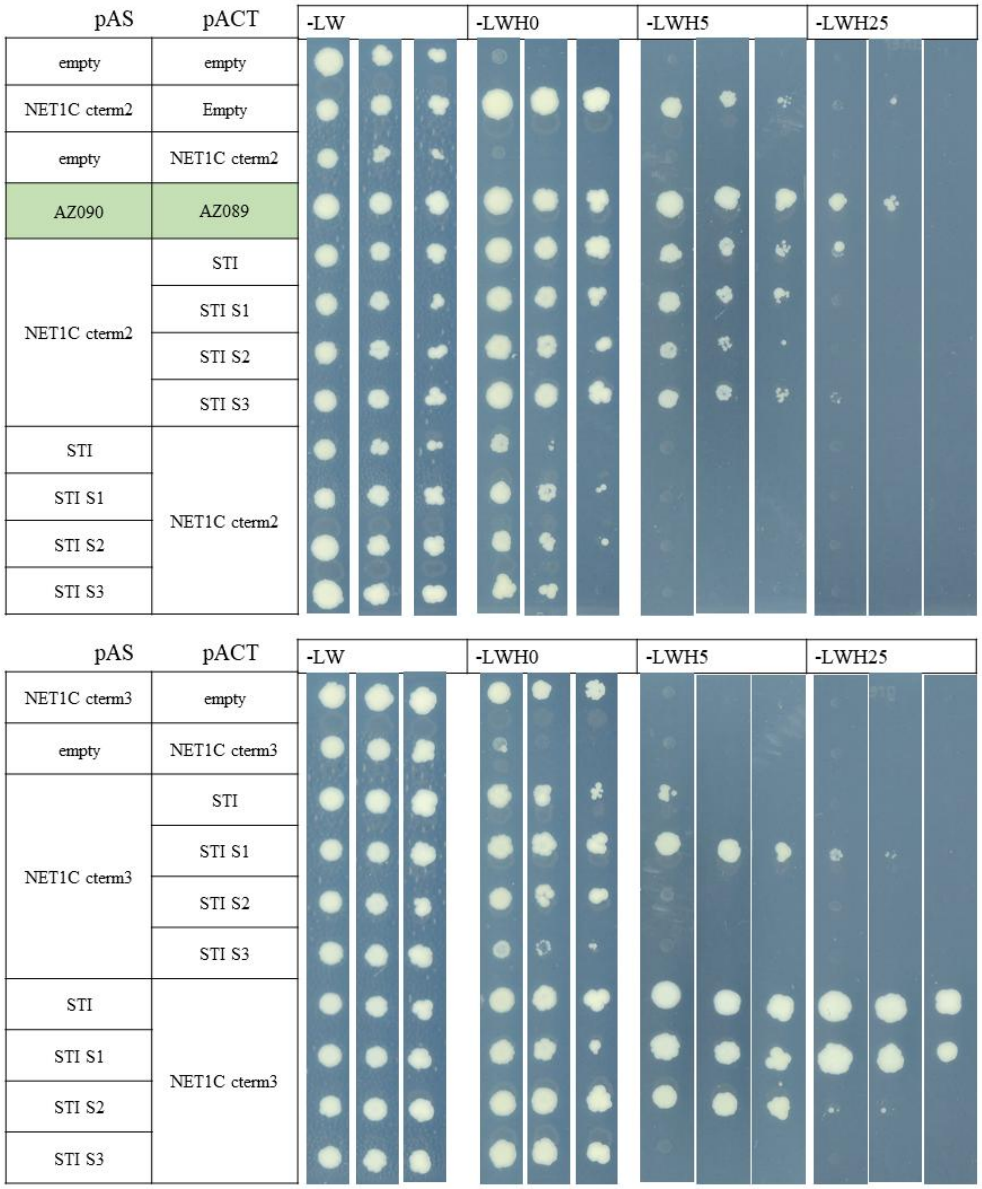

Fig. 57: Set 14.1: Reproducibility analysis of interactions between NET1C C-terminal2 and C-terminal 3 fragments using independent yeast two-hybrid experiments.

Yeast two-hybrid analysis of newly cloned NET1C C-terminal 2 and 3 fragments.Yeast growth was assessed on selective media lacking leucine and tryptophan (-LW), as well as on interaction-selective media lacking leucine, tryptophan and histidine supplemented with increasing concentrations of 3-amino-1,2,4-triazole (3-AT) (-LWH0, -LWH5, -LWH25). Only growth on media containing 3-AT was considered as positive interaction. NET1C cterm2 displayed growth already in combination with the empty vector control, indicating autoactivation. Therefore, positive interactions observed in this vector orientation were not considered biologically meaningful. In the reciprocal orientation, no interaction-dependent growth was detected, and interaction of NET1C cterm2 with STI-derived constructs could therefore not be confirmed. In contrast, NET1C cterm3 showed reproducible interaction-dependent growth with STI S1 in both vector orientations. Interaction was additionally observed for NET1C cterm3 with full-length STI and STI S2 in one vector orientation. The interaction between SNF1 (AZ090) and SNF4 (AZ089) served as positive control (green).

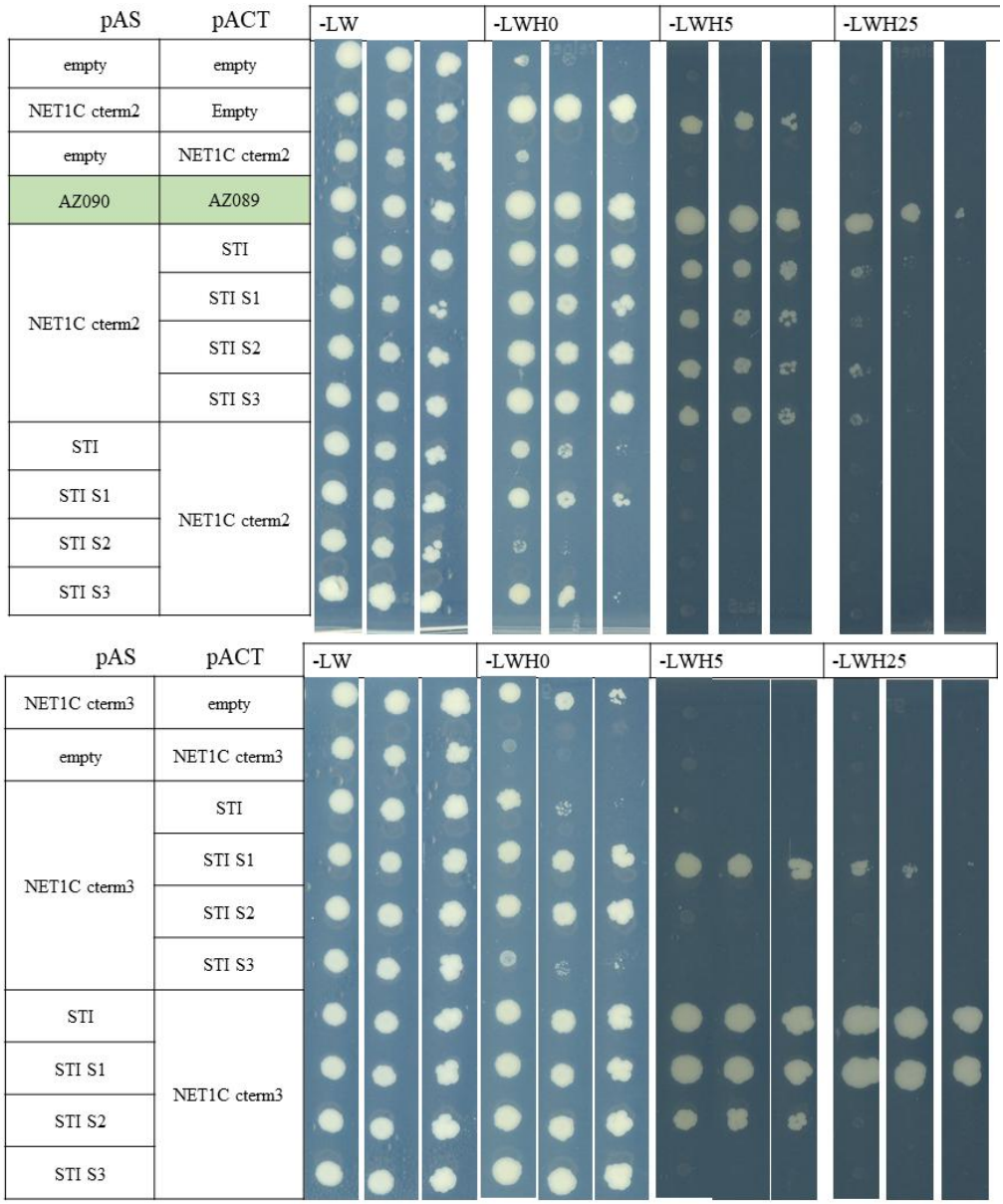

Fig. 58: Set 14.2: Reproducibility analysis of interactions between NET1C C-terminal2 and C-terminal 3 fragments using independent yeast two-hybrid experiments.

Yeast two-hybrid analysis of newly cloned NET1C C-terminal 2 and 3 fragments..Yeast growth was assessed on selective media lacking leucine and tryptophan (-LW), as well as on interaction-selective media lacking leucine, tryptophan and histidine supplemented with increasing concentrations of 3-amino-1,2,4-triazole (3-AT) (-LWH0, -LWH5, -LWH25). Only growth on media containing 3-AT was considered as positive interaction. NET1C cterm2 displayed growth already in combination with the empty vector control, indicating autoactivation. Therefore, positive interactions observed in this vector orientation were not considered biologically meaningful. In the reciprocal orientation, no interaction-dependent growth was detected, and interaction of NET1C cterm2 with STI-derived constructs could therefore not be confirmed. In contrast, NET1C cterm3 showed reproducible interaction-dependent growth with STI S1 in both vector orientations. Interaction was additionally observed for NET1C cterm3 with full-length STI and STI S2 in one vector orientation. The interaction between SNF1 (AZ090) and SNF4 (AZ089) served as positive control (green).

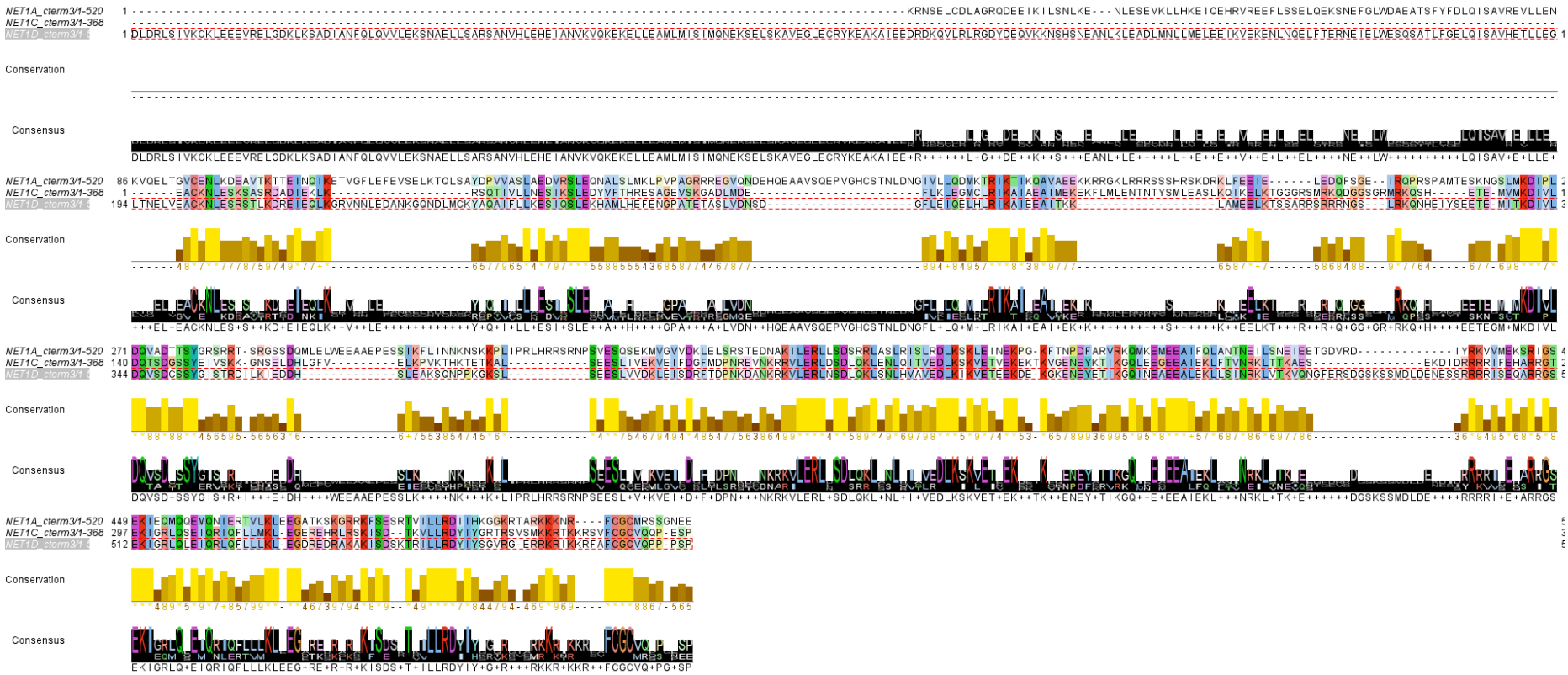

Fig. 59: Multiple sequence alignment of STI-interacting NET1 C-terminal fragments.

Full-length alignment of the interacting NET1 C-terminal fragments NET1A cterm3, NET1C cterm3 and NET1D cterm3 generated using MAFFT (Katoh & Standley, 2013) and visualized in Jalview (Waterhouse et al., 2009). Conserved residues are highlighted according to sequence similarity, and relative sequence conservation is indicated below the alignment. The alignment revealed regions of partial conservation enriched in charged amino acids, but no short highly conserved linear motif shared among all interacting fragments could be identified.